VILNIUS UNIVERSITY

CENTER FOR PHYSICAL SCIENCES AND TECHNOLOGY

VLADIMIR CHOROŠAJEV

VARIATIONAL THEORY OF ELECTRONIC ENERGY TRANSFER AND RELAXATION

Doctoral dissertation

Physical sciences, Physics (02P)

Vilnius, 2017

Dissertation was prepared at Vilnius university in 2014–2017.

Scientific supervisor –

prof. Darius Abramavičius (Vilnius university, Physical sciences, Physics – 02P).

VILNIAUS UNIVERSITETAS

FIZINIŲ IR TECHNOLOGIJOS MOKSLŲ CENTRAS

VLADIMIR CHOROŠAJEV

VARIACINĖ ELEKTRONINIŲ SUŽADINIMŲ PERNAŠOS IR RELAKSACIJOS TEORIJA

Daktaro disertacija

Fiziniai mokslai, Fizika (02P)

Vilnius, 2017

Disertacija rengta 2014–2017 metais Vilniaus universitete.

Mokslinis vadovas –

prof. Darius Abramavičius (Vilniaus universitetas, fiziniai mokslai, fizika – 02P).

Contents

List of abbreviations

h.c. hermitian conjugate

c.c. complex conjugate

2DES two-dimensional electronic spectroscopy

ATRF auxiliary time-resolved fluorescence

BChl bacteriochlorophyll

Chl chlorophyll

DoF degrees of freedom

DFT density functional theory

DMRG density matrix renormalization group

EET electronic energy transfer

ES electronic spectroscopy

FMO Fenna-Mathews-Olson complex

FLN fluorescence line narrowing

HR Huang-Rhys

LH2 light-harvesting complex 2

PSII photosystem II

RC reaction center

SB system–bath

SF system–field

SE stimulated emission

TDVP time-dependent variational principle

TDVA time-dependent variational approach

TD-DMRG time-dependent density matrix renormalization group

sTDVA stochastic time-dependent variational approach

TRF time-resolved fluorescence

ZPL zero-phonon line

Introduction

The theory of optically excited molecular aggregates lies on the intersection of physics, mathematics, chemistry and biology. On one hand, their properties are unlike single molecules, on the other hand the lack of large-scale crystalline structure makes the well-developed approaches of solid state physics inapplicable. Dimensions of molecular aggregates are still microscopic, and hence quantum mechanics is essential for the description of anything that happens immediately after optical excitations (the relevant timescales are from tens of femtoseconds to tens of picoseconds). The other important factor that must be taken into account is that under most circumstances the molecular aggregates cannot be considered isolated. Even at very short times, the interaction with their environment leads to irreversible evolution and decoherence of fragile quantum states. This is further complicated by the fact that the environment can act differently on spatially separated elements of molecular aggregates. The usual approach for theoretical analysis of such open quantum systems is to consider only a few degrees of freedom, with the rest being attributed to a bath (environment). The influence of the environment on the system of study is well defined, however, the influence of the optically excited system on the environment is usually neglected. From an experimental point of view the primary tool used to reveal the quantum dynamics of molecular aggregates is optical spectroscopy.

Probably the most important concept in the study of molecular aggregates is the Frenkel exciton. It defines a collective excitation delocalized over a number of molecules constituting an aggregate. This collective excitation is coherent, i.e. the phase relationships between the excitations of constituent molecules are conserved. The coherence, though, can only be maintained for some time until environmental decoherence sets in, reducing the quantum superposition to a probabilistic mixture. Thus the optical excitation can evolve in a few different ways, with one being coherent wavelike transfer and the other being irreversible dissipative dynamics. If the timescales can be separated (i.e. the coherent wavelike transfer is fast and the decoherence is slow), the theoretical description becomes much simpler. The most difficult scenario is where both coherent transfer and decoherence happen on a very similar timescale. This scenario requires the most sophisticated theoretical

approaches, and also it is the most frequent case in real-world molecular aggregates. The governing attribute that lets us distinguish whether the timescales are separable is the strength of coupling between the system and the bath relative to the coupling between constituent molecules. The extreme cases when one is very small compared to the other one let us treat the small coupling as a perturbation, leading to the well-known Redfield theory (for weak system-bath coupling) and Förster theory (for weak interaction between the optically active molecules). Anything in between falls into the so-called "intermediate" regime where the physics are much more complex. However (as we shall see throughout this thesis), this is not all, and the timescales of correlations of fluctuations of the bath itself also play a huge role even at relatively weak system-bath coupling.

The idea behind the description of the "intermediate" regime is the feedback, or the formation of excitonic polarons. Taking into account the influence of the optical excitation in molecular aggregates on the bath, the bath can become polarized. The Frenkel exciton state that is attributed to purely electronic interaction between optically active molecules becomes "dressed" by the environmental vibrational states. First, the system and the bath undergo collective evolution which transitions the Frenkel exciton state into an excitonic polaron state. Then the evolution between excitonic polaron states continues with the bath serving as a source of fluctuations from its new point of equilibrium. The magnitudes and timescales of such processes are dependent on lots of factors, including the spectral content of the bath, all the relevant coupling parameters, temperature, fluctuation correlations in both space and time, nonlinearities, etc.

Making any kind of valid model from first principles with such a huge amount of free parameters is questionable. Fortunately, much information about molecular aggregates can be obtained from spectroscopic experiments. Recent advances in ultrafast spectroscopy gave an opportunity to see the molecular processes at very short timescales after excitation, when most of the mentioned coherent transfer and dissipation effects happen. Ultrafast time-resolved fluorescence (TRF) and two-dimensional coherent spectroscopy (2D) are the two nonlinear techniques that can reveal the electronic-vibrational dynamics, especially at low temperatures. Historically two-dimensional spectroscopy was the approach that kickstarted the whole field of "quantum biology", which considers the effects of coherent transfer in biological systems such as photosynthetic pigment-protein complexes. A very complicated set of energy transfer pathways with long-lived quantum coherences was revealed first in the Fenna-Mathews-Olson (FMO) complex, and then in various other aggregates such as Light-harvesting complex 2 (LH2), Light-harvesting complex 3 (LH3) and Photosystem II (PSII). Fitting modeled spectroscopic data to experimental data thus became a prominent way to test models of energy transfer

in molecular aggregates. The other missing bits of information about parameters of molecular aggregates come from high-resolution structural data and quantum chemistry calculations. The spectral content of the environmental fluctuations is also a very important variable. Some information can be obtained from quantum chemistry calculations (for intramolecular vibrations) and the lineshapes of optical spectra in absorption, TRF, and 2D experiments. The more accurate data is obtained from hole burning, Raman, and low temperature fluorescence line narrowing experiments.

Having established both the theoretical problem and the sources of experimental data, one needs to proceed with developing a model and a theoretical approach for simulations of the quantum dynamics. From quantum dynamics one needs to obtain the associated simulated spectroscopic data to compare it with the experiment and test the validity of the model. However, at some point one still needs to make some kind of approximation for one reason - the computational resources are limited. Theoretically one could try to calculate everything exactly using the Liouville-von Neumann equation. Practically, not so much, because the amount of degrees of freedom in the environment is effectively infinite. So one very important requirement imposed on any kind of theoretical approach for simulations is that the calculations can be done in a reasonable time. So, having defined the challenges, we shall proceed with developing a theoretical approach for investigating the quantum dynamics of optical excitations in molecular aggregates tailored for the "intermediate" regime and allowing for bath polarization and feedback effects.

Main goal

The **main goal** of this research work is to develop an efficient theoretical approach suitable for calculation of excitation dynamics and optical spectra in molecular aggregates without restrictions on relative coupling strengths and timescales[1]. The following research tasks were formulated in order to achieve this goal:

- Establish and develop a calculation scheme based on the time-dependent variational approach (TDVA) with the Davydov Ansatze, tailored for *non translationally invariant systems coupled to damped/overdamped environments without spatial correlations* (at zero temperature). This includes deriving the equations of motion and writing code for the simulation.
- Investigate the effect of timescales of bath correlations on excitonic polaron formation in a model system at zero temperature.
- Develop an extension of the approach allowing for finite temperature simulations. Benchmark the accuracy of the finite temperature extension against an

[1] Throughout the text, citations[1–5] will be referring to author's own work.

established theoretical approach.

- Apply the developed formalism to the simulation of dynamics and optical spectra in a real molecular aggregate.
- Develop an extension of the approach allowing for treatment of vibrational nonlinearities. Examine the effect of nonlinear system-bath coupling on energy transfer and optical spectra.

Novelty and relevance of the results

Despite the success of the perturbative theories in their respective ranges of validity, it is the intermediate regime, when all interactions are of similar strength, that is often relevant, e.g. in the photosynthetic pigment-protein complexes.[6] Conventional Redfield and Förster theories are unable to explain all the dynamics in a system that interacts strongly with vibrations, and where the intermolecular resonant interactions span the range from small to relatively large values.

Non-perturbative theories that make no assumptions on the relative strength of interactions have become available in recent decades.[7–10] For example, the approach based on hierarchical equations of motion (HEOM) has been applied to study model systems with various strength of resonance interactions between molecules and with the inter- and intra-molecular vibrations.[11–15] It has also been used to describe time resolved spectroscopy experiments.[16–21] Nevertheless, exact theories are usually very expensive computationally, and limited to rather structureless vibrational baths. Therefore in practice their application is often limited.

Other numerical approaches have been adapted from solid state physics. Exact diagonalization[22] is one of the more straightforward methods. One of its major limitations is exponential scaling of required computational resources with the number of electronic and vibrational states. The other major limitation is that damping of vibrations is especially difficult to consistently introduce with this approach. Variational exact diagonalization[23] scales better if only the lower lying bosonic excited states of phonons are considered, but generally suffers from the same problems. Quantum Monte Carlo approach is very computationally efficient, however, its accuracy is not very high and it suffers from the well-known sign problem.[24] Time-dependent density matrix renormalization group is an accurate and efficient method, but its major restriction is that the system has to be one-dimensional and non-disordered.[25]

While the time-dependent variational approach together with the Davydov Ansatze is also a well-known and established method, some usual assumptions make it unsuitable for the application to excitation dynamics in molecular aggregates. First, traditionally it was used with translationally invariant one dimensional systems,

such as linear aggregates and rings, and required adaptation to make it work with disordered systems. Second, it assumed a phonon band with linear dispersion, which is unlike the typical bath encountered in molecular aggregates. Third, the phonons were assumed to be non-local, being coupled to every single site in the system. Local coupling with an individual bath without spatial correlations produces qualitatively different dynamics. And last, it was only applied at zero temperature, which cannot in principle describe the decoherence dynamics so much relevant for energy transfer and optical signals in realistic experimental conditions. The presented research gets rid of these assumptions and provides suitable extensions, validating the approach for simulations of molecular aggregates.

In a model system we were able to show two distinct regimes of excitonic polaron formation. A pair of strongly-coupled molecules was used to illustrate the dynamics of the transition from the excitonic into the polaronic picture. We showed that the excitonic states retain their character only in case of weak coupling to the fast bath. If the coupling to the bath is strong or the bath is slow the excitonic picture breaks down and an excitonic polaron forms. Slow bath leads to an adiabatic excitonic polaron formation regime. Strong interactions with the fast bath induce a rapid change in the elements of the Hamiltonian, causing the non-adiabatic dynamical localization. The effective resonant coupling between sites decreases and the amount of reduction is heavily dependent on the environment reorganization energy and the characteristic bath timescale. The timescale of change in this effective resonant coupling defines the timescale of polaron formation.

The accuracy of TDVA was studied to some extent in its usual range of applications. But since the extension of TDVA to finite temperature (sTDVA) was developed as part of this research work, it naturally had no information on its validity. So an important part of the development was testing the calculation scheme against an established method to determine its limitations. After finding out that the accuracy is sufficient in relevant ranges of parameters, we modeled the energy transfer within the B850 ring of the LH2 photosynthetic complex. The modeled results demonstrate that polaronic effects are small and temperature-dependent in optical absorption and fluorescence spectra. However, the dependence of wavefunction delocalization parameters and especially their asymptotic values signify a transition to the temperature-dependent polaronic picture. While other approaches have given a measure of polaronic effects in long timescale asymptotic states of the system, we were able to provide a completely dynamical picture of the state transition.

Finally, we used another advantage of the presented approach, namely the possible higher-order system-bath couplings. In experimental spectra some nonlinear effects are well-known, such as the breaking of absorption/fluorescence mirror symmetry, the broadening of zero-phonon line and the dependence of peak positions on

temperature. The sTDVA was furthermore extended with a more complicated variational trial wavefunction to simulate the dynamics in presence of nonlinearities.

Statements of the thesis

1. Formation of excitonic polarons is governed by two essential parameters: the strength of the system-bath interaction, and the bath correlation timescale compared to inverse couplings between the sites of the system. Depending on the timescale, two qualitatively distinct regimes are possible, with one being the adiabatic polaron formation when the bath timescale is slow, and the other being the coherent polaron formation when the bath is fast. The system-bath coupling strength scales this effect.

2. Thermal effects lead to increased state delocalization and decreased self-trapping, impeding the excitonic polaron formation. In an ensemble measurement the length of coherence decreases with temperature, and at room temperatures and long times the excitonic representation remains valid.

3. A nonlinear coupling between electronic states and vibrational states or a bath produces characteristic signatures (vibrational peak substructure, continuous spectrum generation at finite temperatures, fluorescence mirror symmetry breaking) in linear and nonlinear optical spectra, but the electronic energy transfer is very weakly affected by nonlinearities.

List of publications

The results are presented in scientific articles:

1. V. Chorošajev, A. Gelzinis, L. Valkunas, D. Abramavicius. **Dynamics of exciton-polaron transition in molecular assemblies: The variational approach.** The Journal of Chemical Physics **140**, 244108 (2014)

2. V. Chorošajev, O. Rancova, D. Abramavicius. **Polaronic effects at finite temperatures in the B850 ring of the LH2 complex.** Physical Chemistry Chemical Physics, **18**, 7966-7977 (2016)

3. V. Chorošajev, A. Gelzinis, L. Valkunas, D. Abramavicius. **Benchmarking the stochastic time-dependent variational approach for excitation dynamics in molecular aggregates.** Chemical Physics, **481**, 108 (2016)

4. J.Pan, A. Gelzinis, V. Chorošajev, M. Vengris, S. S. Senlik, J. Shen, L. Valkunas, D. Abramavicius, J. P. Ogilvie. **Ultrafast energy transfer within the photosystem II core complex.** Physical Chemistry Chemical Physics, **19**, 19536 (2017)

5. V. Chorošajev, T. Marciulionis, D. Abramavicius. **Temporal dynamics of excitonic states with nonlinear electronic-vibrational coupling.** The Journal of Chemical Physics, **147**, 074114 (2017)

In 1,2,3,5 the author of this thesis was the first author of the article, derived the presented sTDVA theory, performed the numerical calculations and wrote a major part of the discussion. In paper 4, which was a collaboration with an experimental group, the author has performed the numerical calculations of population dynamics and optical spectra and contributed to interpretation of the experimental results.

The results have been presented in conferences:

1. V. Chorošajev., D. Abramavičius. **Dinaminės poliaroninės būsenos tyrimas variaciniu metodu.** 40 Lietuvos Nacionalinė Fizikos Konferencija 2013 May 10-12 Vilnius

2. V. Chorošajev., D. Abramavičius. **Dynamics of excitonic polaron formation in molecular assemblies.** Nordic Femtochemistry 2014, May 26-27 Vilnius

3. V. Chorošajev., D. Abramavičius **Poliaroniniai efektai LH2 šviesos surinkimo komplekso kvantinėje dinamikoje.** 41 Lietuvos Nacionalinė Fizikos Konferencija 2014 May 17-19 Vilnius

4. V. Chorošajev., D. Abramavičius **Stochastic variational approach for investigation of quantum dynamics in light harvesting complexes.** Quantum Physics of Nature 2015 March 28-31 Vienna

5. V. Chorošajev., O.Rancova, D. Abramavičius **Stochastic variational approach to polaron formation dynamics in molecular aggregates.** Nordic Femtochemistry 23-26 May 2016, Orenas

Chapter 1

Theory of the variational approach to quantum dynamics

In this chapter we present a short overview of the theory of non-equilibrium dissipative dynamics in open quantum systems. First we develop some common concepts concerning the object of study, along with a review of other relevant methods applied in this thesis. Then we proceed to the approach forming the foundation of all the research presented in this thesis, namely, the time-dependent variational approach (TDVA) and its generalizations and extensions. We finish the chapter with a short review of alternative approaches to the theory of excitation energy transfer and relaxation.

Without specifying the physical system, we may write the total Hamiltonian as

$$\hat{H} = \hat{H}_{\mathrm{S}} + \hat{H}_{\mathrm{B}} + \hat{H}_{\mathrm{SB}} + \hat{H}_{\mathrm{F}},$$

where $\hat{H}_{\mathrm{S}}$ is the physical system of study. That means that we wish to obtain the time evolutions of anything assigned to the *system* part of the Hamiltonian explicitly and as accurately as possible. $\hat{H}_{\mathrm{B}}$ denotes the *environment* of the physical system. It is often considered that the amount of the degrees of freedom in the environment is effectively infinite, so explicit evaluation of their dynamics is not usually sought. Some approximation is used instead to evaluate the collective state of the environment. $\hat{H}_{\mathrm{SB}}$ is the interaction term between the system and the environment, which mediates the effect of the environment on the physical system (and also mediates the effect of the physical system on the environment). $\hat{H}_{\mathrm{F}}$ (where F stands for *field*) usually contains the external factors defined by the experimental setup, which are well-defined and controlled. The most relevant example is optical fields creating excitations in the physical system.

The state of an isolated quantum system (disregarding the interaction with the en-

vironment) can be completely defined by its wavefunction[1] - a vector in the Hilbert space spanned by all available *pure* quantum states of the system. The time evolution of a pure quantum state is described by a time-dependent Schrödinger equation

$$-\mathrm{i}\hbar\frac{\partial}{\partial t}|\psi(t)\rangle + \hat{H}|\psi(t)\rangle = 0. \tag{1.1}$$

When the system is in a pure quantum state, all physical observables are defined up to Heisenberg's uncertainty relation for pairs of complementary variables. The state of a system being in a pure quantum state is considered to be fully known, and the entropy of such a state is always equal to zero.

In case we have only partial knowledge about the state of the system (or none at all), we consider the state to be *mixed,* treating it like a probabilistic mixture of pure states. This mixture is defined in terms of *density operators*

$$\hat{\rho}(t) = \sum_i p_i|\psi_i(t)\rangle\langle\psi_i(t)|, \tag{1.2}$$

where p_i is the classical probability of the system being in a pure state $|\psi_i(t)\rangle$. Different mixtures of pure quantum states can give the same physical observables. The entropy of a mixed state is

$$S = \sum_i p_i \ln p_i. \tag{1.3}$$

The evolution of density operators is governed by the Liouville-von Neumann equation:

$$-\mathrm{i}\hbar\frac{\partial}{\partial t}\hat{\rho}(t) + \left[\hat{H}, \hat{\rho}(t)\right] = 0. \tag{1.4}$$

Most attempts of theoretical description of open quantum systems require the use of the density operator approach due to the fact that the state of the environment is not measurable. However, mathematically both wavefunction and density operator approaches are equivalent (at least, up until one traces over the environmental degrees of freedom in the full system-environment density operator). The approach used in this thesis is based on wavefunction propagation, and the density operator used in evaluation of some quantities is constructed a posteriori according to the Eq. (1.2).

In the following chapter we will first define the system of study in Section 1.1. The properties of the environment and the corresponding definitions are given in Section 1.2. In Section 1.3 we proceed to introduce the time-dependent variational approach and derive the equations of motion used in subsequent modeling of molec-

[1]The *wavefunction* term technically only applies if the Hilbert space is a function space. However, in this thesis we will use the terms *state* and *wavefunction* interchangeably.

ular aggregate dynamics at zero temperature. In Section 1.5 we describe an extension to TDVA, allowing to simulate quantum dynamics at finite temperatures. And last, in Section 1.6 we introduce a new trial wavefunction used for modeling of a nonlinear interaction between the system and the environment.

For simplicity, we will assume natural units in the text, setting $\hbar = 1$, $c = 1$, $\frac{1}{4\pi\epsilon\epsilon_0} = 1$.

1.1 Electronic-vibrational systems

The central concept in the theory of quantum dynamics of molecular aggregates is the Frenkel exciton. We consider an aggregate to be a cluster of neutral electrostatically interacting molecules. The charge density is assumed to be strongly localized on the molecules, and the overlap of the electronic wavefunctions between different molecules in the aggregate is considered to be zero. The ground and excited states of each individual molecule can be then obtained solving the time-independent Schrödinger equation with the molecular Hamiltonian (the approach can be readily found in ref.,[26] but is beyond the scope of the thesis). Note that we restrict the set of all possible excitations of a single molecule to only two states, thus treating the molecule as a two-level system[2]. The basis vectors, which we denote $|\psi_n\rangle^{(\mathrm{g})}$ for the ground state, and $|\psi_n\rangle^{(\mathrm{e})}$ for the excited state, are used for construction of the global electronic state of the molecular aggregate. First we denote the global electronic ground state as the product of ground states of all constituent molecules:

$$|0\rangle_{\mathrm{el}} = \prod_n |\psi_n\rangle^{(\mathrm{g})}. \tag{1.5}$$

We use the ladder operator formalism for describing localized excitations: the creation operator for the local electronic excitation at molecule n is defined by

$$\hat{a}_n^\dagger |\psi_n\rangle^{(\mathrm{g})} = |\psi_n\rangle^{(\mathrm{e})}. \tag{1.6}$$

Then the first and second excitation manifolds of the molecular aggregate are (for $m \neq n$):

$$|n\rangle = \hat{a}_n^\dagger |0\rangle_{\mathrm{el}}, \tag{1.7}$$

$$|mn\rangle = \hat{a}_m^\dagger \hat{a}_n^\dagger |0\rangle_{\mathrm{el}}. \tag{1.8}$$

This set of product states $|n\rangle$ is known as the *site* basis, and the constituent molecules will be referred to as sites further in the text. The ladder operators for the electronic

[2]Higher-lying molecular excited states are difficult to access within an experimental setup, since their transition energy is approximately double the energy of the first excited state.

excitations obey the following commutation relation (also known as Paulionic):

$$\left[\hat{a}_m, \hat{a}_n^\dagger\right] = \delta_{mn}\left(1 - 2\hat{a}_n^\dagger \hat{a}_m\right). \tag{1.9}$$

Solving the single-molecule Schrödinger equation (usually using some approximate method like DFT) allows one to obtain the transition energies between the ground and excited states, and also ground, excited state, and transition charge densities, that we denote respectively by $\rho^{(\mathrm{g})}$, $\rho^{(\mathrm{e})}$, $\rho^{(\mathrm{t})}$. They are needed for construction of electronic block Hamiltonians. The diagonal elements corresponding to the projectors $\hat{a}_n^\dagger \hat{a}_n$ are transition energies ε_n of single non-interacting molecules modified by the correction term for the Coulomb interaction between the spatial charge of the excited state of the molecule under consideration $\rho_n^{(\mathrm{e})}$ and the spatial charges corresponding to ground states of other molecules in the aggregate $\rho_{m\neq n}^{(\mathrm{g})}$. The off-diagonal elements correspond to projectors $\hat{a}_{m\neq n}^\dagger \hat{a}_n$ and their values J_{mn} are calculated as the Coulomb interaction between the transition charge densities $\rho_{m\neq n}^{(\mathrm{t})}$ and $\rho_n^{(\mathrm{t})}$.

In most cases for naturally occurring aggregates the intermolecular distances are assumed to be much larger than the localization length of local electronic densities. Then the transition energy ε_n correction term can be assumed to be zero, and the interaction between two sites can be calculated using the dipole approximation. Denoting the transition dipole vector of site n as $\boldsymbol{\mu}_n$, and the spatial coordinate vector of site n as $\boldsymbol{R}_n$ the interaction strength is calculated as

$$J_{m\neq n,n} = \left(\frac{\boldsymbol{\mu}_m \cdot \boldsymbol{\mu}_n}{|\boldsymbol{R}_m - \boldsymbol{R}_n|^3} - 3\frac{(\boldsymbol{R}_m - \boldsymbol{R}_n)\cdot \boldsymbol{\mu}_m \, (\boldsymbol{R}_m - \boldsymbol{R}_n)\cdot \boldsymbol{\mu}_n}{|\boldsymbol{R}_m - \boldsymbol{R}_n|^5}\right). \tag{1.10}$$

Consequently, the total resulting electronic block Hamiltonian is written as

$$\hat{H} = \sum_n \varepsilon_n \hat{a}_n^\dagger \hat{a}_n + \sum_{m\neq n} J_{mn} \hat{a}_m^\dagger \hat{a}_n, \tag{1.11}$$

however, we will use a slightly more compact notation in this thesis, setting the diagonal elements of J_{mn} as

$$J_{nn} \equiv \varepsilon_n, \tag{1.12}$$

and writing the electronic block Hamiltonian simply as

$$\hat{H} = \sum_{m,n} J_{mn} \hat{a}_m^\dagger \hat{a}_n. \tag{1.13}$$

Another important basis is the *excitonic* basis, which is simply the set of eigenvectors of the electronic block Hamiltonian, easily obtained by direct diagonaliza-

tion. The corresponding eigenvalues are excitonic energies. Excitonic basis vectors are related to site basis vectors by a unitary transformation matrix

$$|\alpha\rangle = \sum_n U^{\dagger}_{\alpha n}|n\rangle. \tag{1.14}$$

1.2 Environment

In realistic scenarios molecular aggregates are not isolated from their environment. The electronic degrees of freedom defined in the previous chapter are usually interacting with vibrations of the nuclei, which are both intramolecular modes (referring to the vibrational modes of the optically active sites), and interactions with the protein scaffold or solvent in which the aggregate is embedded. The number of vibrational degrees of freedom is usually considered to be infinite, and for a description of this type of environment its statistical properties at finite temperature have to be considered.

At the basic level the environment can be described as a bath of harmonic oscillators coupled to one or more sites of the electronic subsystem. The parameters that define the bath are temperature and the set of coupling strengths between the modes of the environment and the sites of the system. While other models are sometimes used, we consider the coupling to be diagonal, i.e. the environmental vibrations influence the site transition energies, which correspond to the diagonal elements of the electronic block Hamiltonian. We define the energy operator for each vibrational mode q as

$$\hat{H}_{\mathrm{B}} = \sum_q \omega_q \hat{b}^{\dagger}_q \hat{b}_q, \tag{1.15}$$

denoting the creation and annihilation operators for the mode q of frequency ω_q as $\hat{b}^{\dagger}_q$ and $\hat{b}_q$. In contrast to ladder operators for the electronic excited states, the operators obey the bosonic commutation relation

$$\left[\hat{b}_q, \hat{b}^{\dagger}_s\right] = \delta_{qs}\hat{b}^{\dagger}_s\hat{b}_q. \tag{1.16}$$

The diagonal coupling between the electronic subsystem and the environment is therefore realized using the bilinear operator:

$$\hat{H}_{\mathrm{SB}} = \sum_n \hat{a}^{\dagger}_n \hat{a}_n \sum_q \omega_q g_{qn} \left(\hat{b}^{\dagger}_q + \hat{b}_q\right). \tag{1.17}$$

The essential property of the bath is the set of linear coupling strengths $\{g_{qn}\}$. The values of coupling parameters can be calculated from first principles or measured experimentally in some cases, but it is much more common to involve the sta-

tistical properties of the collective bath for description of non-stationary dynamics. The environment-induced fluctuations of the transition energy are then characterized by the correlation functions of the bath:

$$C_{ij}(t) = \langle \Delta\hat{V}_i(t)\Delta\hat{V}_j(0)\rangle, \tag{1.18}$$

where $\Delta V_i(t)$ is the system-bath interaction operator for site i in Heisenberg representation, defined as

$$\Delta\hat{V}_i(t) = \exp\left(\mathrm{i}\hat{H}_\mathrm{B}t\right)\hat{a}_i^\dagger\hat{a}_i\sum_q \omega_q g_{qi}\left(\hat{b}_q^\dagger + \hat{b}_q\right)\exp\left(-\mathrm{i}\hat{H}_\mathrm{B}t\right), \tag{1.19}$$

and $\langle\cdots\rangle$ represents the expectation value. It is calculated as $\left\langle\hat{A}\right\rangle = \mathrm{Tr}\left(\hat{\rho}\hat{A}\right)$, where $\hat{\rho}$ is the global density operator of both the system and the bath.

The set of linear coupling strengths can then be obtained from the Fourier transform of the correlation function, where the temperature-independent odd part $C''_{ij}(\omega)$ is the spectral density of the environment:

$$C_{ij}(t) = \frac{1}{\pi}\int \mathrm{e}^{-i\omega t}\frac{1}{1-\mathrm{e}^{\frac{\omega}{kT}}}C''_{ij}(\omega)\,\mathrm{d}\omega, \tag{1.20}$$

$$C''_{ij}(\omega) = \pi\sum_q g_{qi}g_{qj}\omega_q^2\delta(\omega-\omega_q). \tag{1.21}$$

An assumption that is often relevant for calculating the physical observables of molecular aggregates is that the modes are *local*, meaning that each site of the system is coupled to its own independent set of modes, and the fluctuations of the local environment are uncorrelated. This allows to shorten the notation as $C_{ii}(t) = C_i(t)$.

Due to dissipative processes, the correlation functions decay with time. This causes the spectral density functions to be continuous instead of sets of discrete delta-peaks centered at certain frequencies. In order to incorporate the dissipative effects the discrete damped modes are replaced with sets of fictitious harmonic oscillators, discretizing continuous spectral densities of damped and overdamped modes with large amounts of undamped modes. Throughout this thesis we discretize the spectral density uniformly in the argument range $(0, W]$, where W is the frequency width of the phonon band. This bandwidth should be chosen to be much larger than all possible frequencies of the system (essentially the exciton bandwidth for our problem). We use $q = 1, 2...Q$ and the frequency of mode q is $\omega_q = \Delta_\omega q$. The minimum frequency interval $\Delta_\omega = W/Q$ defines a recurrence timescale equal to $2\pi Q/W$. In general the latter should be larger than any timescale of interest in the system dynamics. These relations fix the parameters Q and W. The coupling

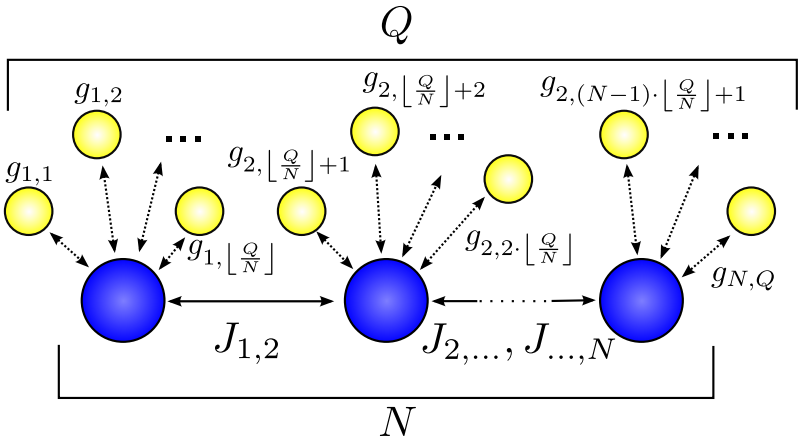

Fig. 1.1. Schematic view of the system. Blue circles denote sites, yellow circles denote modes of the phonon field, with couplings indicated by arrows.

strengths can be assigned using Eq. (1.21): $g_{qn}^2 \propto C_n''(\omega_q)/\omega_q^2$. The sign of g_{qn} remains undefined, so we keep it positive, while the values are normalized using the definition of the reorganization energy. The reorganization energy is defined as the negative energy shift in the site electronic transition energy that appears after the local environment of that site relaxes into the minimum of its potential surface in the electronically excited state, and is also known as Stokes shift. The reorganization energy is related to the spectral density simply as:

$$\Lambda_n = \frac{1}{\pi}\int_0^\infty \frac{1}{\omega} C_n''(\omega)\,\mathrm{d}\omega. \tag{1.22}$$

Practically, the spectral density functions of the environment are either measured experimentally (specifically, fluorescence line narrowing experiments) or are simply postulated by using a model for the environment. The model may be as simple as assuming an exponential decay of the correlation function, which gives the well known Brownian oscillator spectral density.

Combining the electronic and environmental subsystems we obtain the full Holstein[27] Hamiltonian[3] as:

$$\begin{aligned}\hat{H} = &\sum_{m,n} J_{mn}\hat{a}_m^\dagger \hat{a}_n + \sum_q \omega_q \hat{b}_q^\dagger \hat{b}_q \\ &- \sum_n \hat{a}_n^\dagger \hat{a}_n \sum_q g_{qn}\omega_q(\hat{b}_q^\dagger + \hat{b}_q).\end{aligned} \tag{1.23}$$

Fig. 1.1 displays a schematic view of the system under consideration.

[3]The resulting state of the "global" system is described by a vector in $[\mathcal{H}_2]^N \otimes \left[L^2(\mathbb{R})\right]^Q$ space, where $\mathcal{H}_2$ represents a two-dimensional Hilbert space spanned by two orthogonal normalized states $|0\rangle$ and $|1\rangle$. The operator basis for $\mathcal{H}_2$ is realized by the Pauli group.

1.3 Time-dependent variational approach

Instead of solving the Schrödinger equation with the Hamiltonian defined by Eq. (1.23) by direct propagation (which is not possible in our case due to the sheer amount of degrees of freedom), we employ the Dirac-Frenkel variational principle to obtain the approximate quantum dynamics.[28] We use a parametrized trial wavefunction and optimize the variational parameters so that the deviation from the solution of the Schrödinger equation would be minimal. With a generic form of the parametrized wavefunction, written in terms of a set of time-dependent generalized coordinates $|\psi(t)\rangle = |\psi\{x_n(t)\}\rangle$, we try to find the functions $\{x_n(t)\}$ that would make the parametrized wavefunction evolve as close to the exact solution as possible.

In case the wavefunction $|\psi(t)\rangle = |\psi\{x_n(t)\}\rangle$ is not an exact solution to the Schrödinger equation, we have

$$-\mathrm{i}\hbar\frac{\partial}{\partial t}|\psi(t)\rangle + \hat{H}|\psi(t)\rangle = |\delta(t)\rangle, \tag{1.24}$$

where $|\delta(t)\rangle$ is the deviation vector. The procedure to obtain the parameter dependences on time that would minimize the deviation from the exact solution is as follows.[29] First, we construct the quantum Lagrangian, which is given by

$$\mathcal{L} = \frac{\mathrm{i}}{2}\left(\langle\psi(t)|\dot{\psi}(t)\rangle - \langle\dot{\psi}(t)|\psi(t)\rangle\right) - \langle\psi(t)|\hat{H}|\psi(t)\rangle. \tag{1.25}$$

With this Lagrangian we derive the equations of motion (EOM) using the Euler-Lagrange equations for the variational parameters $\{x_n(t)\}$:

$$\frac{\mathrm{d}}{\mathrm{d}t}\left(\frac{\partial\mathcal{L}}{\partial\dot{x}_n^*}\right) - \frac{\partial\mathcal{L}}{\partial x_n^*} = 0, \forall n. \tag{1.26}$$

The resulting set of equations gives in general a system of coupled first order ODE's of the form $\dot{x}_n = f(x_1 \ldots x_N)$, which can be solved using standard numerical methods given a set of initial conditions $\{x_n(0)\}$.

This approach results in an initial value problem that can be solved numerically using common methods (for example, the adaptive step Runge-Kutta (4,5) algorithm).

1.4 Trial wavefunctions

1.4.1 Coherent states

In this subsection we give a short description of coherent states. Widely used in quantum optics for the description of quantized electromagnetic fields, coherent states have an indefinite amount of quanta (particles). The product of amplitude and phase uncertainties is always minimal (as allowed by the uncertainty principle) for a coherent state. In this regard they are the closest to a classical description of a field. These states can be generated using the one-mode displacement operator:

$$\hat{D}(\lambda) = \exp\left(\lambda \hat{b}^\dagger - \text{h.c.}\right). \tag{1.27}$$

Here λ is a complex displacement parameter. Its real part corresponds to the displacement of the wavepacket along the generalized coordinate axis, and the imaginary part corresponds to the displacement along the momentum axis. A coherent state $|\lambda\rangle$ is defined as the state obtained by acting with a displacement operator $\hat{D}(\lambda)$ on the vacuum state $|0\rangle$. One important property of coherent states is that they are eigenstates of the annihilation operator, as described by the relationship

$$\hat{b}|\lambda\rangle = \lambda|\lambda\rangle. \tag{1.28}$$

The expansion of a coherent state in the number state basis is given as

$$|\lambda\rangle = e^{-\frac{1}{2}|\lambda|^2} \sum_{n=0}^{\infty} \frac{\lambda^n}{\sqrt{n!}} |n\rangle. \tag{1.29}$$

To calculate expectation values of various physical observables we use the Baker-Campbell-Hausdorff (BCH) lemma.[30] For any pair of bounded operators $\hat{X}, \hat{Z}$, we may write a series expansion:

$$e^{\hat{X}} \hat{Z} e^{-\hat{X}} = \hat{Z} + [\hat{X}, \hat{Z}] + \frac{1}{2!}[\hat{X}, [\hat{X}, \hat{Z}]] + \cdots. \tag{1.30}$$

Since the displacement operator is unitary ($\hat{D}(\lambda)^\dagger = \hat{D}(-\lambda)$) we may use the BCH lemma to calculate the expectation values of any operators of the form $\left(\hat{b}^\dagger\right)^m \left(\hat{b}\right)^n$ (in that case the series expansion is finite) in a coherent state. Some useful identities that will be used in further derivations are:

$$\langle\lambda|\hat{b}|\lambda\rangle = \lambda, \tag{1.31}$$

$$\langle\lambda|\hat{b}^\dagger|\lambda\rangle = \lambda^\star, \tag{1.32}$$

$$\langle\lambda|\hat{b}^\dagger\hat{b}|\lambda\rangle = |\lambda|^2. \tag{1.33}$$

The coherent states form an *overcomplete* basis for the Hilbert space spanned by number states, meaning that the identity operator is expressed in the coherent state basis as

$$\int |\lambda\rangle\langle\lambda| \, \mathrm{d}^2\lambda = \pi\hat{I}. \tag{1.34}$$

For a system being in a coherent state $|\lambda\rangle$ the probability of measuring the number of quanta as n is calculated using the (1.29) expansion:

$$P_n(\lambda) = |\langle n|\lambda\rangle|^2 = e^{-|\lambda|^2}\frac{\left(|\lambda|^2\right)^n}{n!}. \tag{1.35}$$

1.4.2 Davydov Ansatze

The primary approximation involved in constructing a Davydov Ansatz is the assumption that each vibrational state is parametrized using a few parameters. Although the idea is conceptually similar to the vibronic model, instead of a truncated set of amplitudes in number state basis one uses the coherent state basis for the representation of the phonon states. For every phonon mode q we define a displacement operator acting on the mode q:

$$\hat{D}_q(\lambda) = \exp\left(\lambda\hat{b}_q^\dagger - \mathrm{h.c.}\right).$$

In the simplest cases the state of each mode is represented with either a single coherent state or a superposition of coherent states. This is the case with the original Davydov Ansatz,[29,31–34] also denoted as D_1, which describes the global wavefunction with a set of parameters $\{\alpha_n, \lambda_{qn}\}$:

$$|\Psi_{D1}(t)\rangle = \sum_n \alpha_n(t)\hat{a}_n^\dagger \prod_q \hat{D}_q(\lambda_{qn})|0\rangle. \tag{1.36}$$

The parameters describing the system are site excitation amplitudes $\{\alpha_n(t)\}$ and phonon mode displacements $\{\lambda_{qn}(t)\}$. The Davydov Ansatz D_2 is a simplified version of the D_1:

$$|\Psi_{D2}(t)\rangle = \sum_n \alpha_n(t)\hat{a}_n^\dagger \prod_q \hat{D}_q(\lambda_q)|0\rangle, \tag{1.37}$$

the difference being that $\lambda_{qn}(t) = \lambda_q(t)$. In this case the global wavefunction is separable (a direct product of the electronic subsystem state and the vibrational subsystem state).

In some cases, translationally invariant variants of the Davydov Ansatz have sig-

nificant computational advantages, e.g. Merryfield Ansatz and Global-Local (GL) Ansatz.[35,36] However, this study is focused on systems with broken translational invariance, so for the larger part of the thesis we will use either the D_1 or the D_2 Ansatze. A more complicated $\mathcal{S}_2$ Ansatz that allows the treatment of nonlinear system-bath interaction terms will be introduced in Section 1.6.

We will proceed with the derivation of equations of motion using the Holstein Hamiltonian (1.23) and the Davydov Ansatze D_1 and D_2.

1.4.3 Equations of motion for the D_1 Ansatz

Following the procedure outlined in Section 1.3, we first construct the Lagrangian according to Eq. (1.25)

$$\mathcal{L} = \frac{\mathrm{i}}{2}\left(\langle\Psi_{D1}|\dot{\Psi}_{D1}\rangle - \langle\dot{\Psi}_{D1}|\Psi_{D1}\rangle\right) - \langle\Psi_{D1}|\hat{H}|\Psi_{D1}\rangle \tag{1.38}$$

The set of variational parameters is $\{\alpha_n, \lambda_{qn}\}$, with each variable being a time-dependent function. Next we will evaluate each term in the Lagrangian individually using the explicit form of the D_1 Ansatz. We start with calculating its time derivative:

$$|\dot{\Psi}_{D1}\rangle = \frac{\mathrm{d}}{\mathrm{d}t}\left(\sum_n \alpha_n(t)\hat{a}_n^\dagger \sum_q \exp\left[-\frac{1}{2}|\lambda_{qn}|^2\right]\sum_{k=0}^{\infty}\frac{\lambda_{qn}^k}{\sqrt{k!}}|k\rangle\right) \tag{1.39}$$

$$= \sum_n \Bigg\{ \dot{\alpha}_n \hat{a}_n^\dagger \tag{1.40}$$

$$+ \alpha_n \hat{a}_n^\dagger \sum_q \left[\dot{\lambda}_{qn}\hat{b}_q^\dagger - \frac{1}{2}\left(\dot{\lambda}_{qn}\lambda_{qn}^* + \text{c.c.}\right)\right]\Bigg\}\prod_q \hat{D}_q(\lambda_{qn})|0\rangle.$$

Taking the inner product of D_1 Ansatz and its time derivative, and applying relations (1.31)-(1.32) we obtain

$$\langle\Psi_{D1} \mid \dot{\Psi}_{D1}\rangle = \sum_n \left\{\dot{\alpha}_n\alpha_n^* + |\alpha_n|^2\sum_q \dot{\lambda}_{qn}\lambda_{qn}^* - \frac{1}{2}|\alpha_n|^2\sum_q\left(\dot{\lambda}_{qn}\lambda_{qn}^* + \text{c.c.}\right)\right\}. \tag{1.41}$$

Using the calculated inner product and its complex conjugate, we arrive at the so-called kinetic term of the Lagrangian

$$\frac{\mathrm{i}}{2}\left(\langle\Psi_{D1}|\dot{\Psi}_{D1}\rangle - \langle\dot{\Psi}_{D1}|\Psi_{D1}\rangle\right)$$
$$= \frac{\mathrm{i}}{2}\sum_n\left(\dot{\alpha}_n\alpha_n^* - \dot{\alpha}_n^*\alpha_n + |\alpha_n|^2\sum_q\left\{\dot{\lambda}_{qn}\lambda_{qn}^* - \text{c.c.}\right\}\right). \tag{1.42}$$

For the "potential" term we calculate the system, bath and interaction terms separately:

$$\begin{aligned} E_{\mathrm{S}} &= \langle\Psi_{D1}|\hat{H}_{\mathrm{S}}|\Psi_{D1}\rangle \\ &= \sum_{m,n} J_{mn}\alpha_n^*\alpha_m \cdot S_{n,m}, \end{aligned} \tag{1.43}$$

$$\begin{aligned} E_{\mathrm{B}} &= \langle\Psi_{D1}|\hat{H}_{\mathrm{B}}|\Psi_{D1}\rangle \\ &= \sum_n |\alpha_n|^2\sum_q \omega_q|\lambda_{qn}|^2, \end{aligned} \tag{1.44}$$

$$\begin{aligned} E_{\mathrm{SB}} &= \langle\Psi_{D1}|\hat{H}_{\mathrm{SB}}|\Psi_{D1}\rangle \\ &= -\sum_n |\alpha_n|^2\sum_q g_{qn}\omega_q\left(\lambda_{qn}^* + \lambda_{qn}\right), \end{aligned} \tag{1.45}$$

here $S_{n,m}$ is the Debye-Waller factor (coherent state overlap integral), equal to:

$$S_{n,m} \;=\; \exp\sum_q\left[\lambda_{qn}^*\lambda_{qm} - \frac{1}{2}\left(\lambda_{qn}^*\lambda_{qn} + \lambda_{qm}^*\lambda_{qm}\right)\right]. \tag{1.46}$$

Taking the kinetic and substracting the potential terms, we obtain the Lagrangian as a function of the variable set $\{\alpha_n, \dot{\alpha}_n, \lambda_{qn}, \dot{\lambda}_{qn}\}$:

$$\begin{aligned} \mathcal{L} = &\frac{\mathrm{i}}{2}\sum_n\left(\alpha_n^*\dot{\alpha}_n - \alpha_n\dot{\alpha}_n^* + |\alpha_n|^2\sum_q\left[\lambda_{qn}^*\dot{\lambda}_{qn} - \text{c.c.}\right]\right) \\ &- \sum_{m,n} J_{mn}\alpha_n^*\alpha_m \cdot S_{n,m} - \sum_n |\alpha_n|^2\sum_q \omega_q|\lambda_{qn}|^2 \\ &+ \sum_n |\alpha_n|^2\sum_q g_{qn}\omega_q\left(\lambda_{qn}^* + \lambda_{qn}\right) \end{aligned} \tag{1.47}$$

The Euler-Lagrange equations are used with the set of variational parameters $\{\alpha_n^*, \lambda_{qn}^*\}$:

$$\frac{\mathrm{d}}{\mathrm{d}t}\left(\frac{\partial \mathcal{L}}{\partial \dot{\alpha}_n^*}\right) - \left(\frac{\partial \mathcal{L}}{\partial \alpha_n^*}\right) = 0 \,\forall n, \tag{1.48}$$

$$\frac{\mathrm{d}}{\mathrm{d}t}\left(\frac{\partial \mathcal{L}}{\partial \dot{\lambda}_{qn}^*}\right) - \left(\frac{\partial \mathcal{L}}{\partial \lambda_{qn}^*}\right) = 0 \,\forall \{n, q\}. \tag{1.49}$$

Inserting the calculated full Lagrangian (1.47) into the Euler-Lagrange equations we obtain the explicit partial derivatives:

$$\frac{\mathrm{d}}{\mathrm{d}t}\left(\frac{\partial \mathcal{L}}{\partial \dot{\alpha}_n^*}\right) = -\frac{\mathrm{i}}{2}\dot{\alpha}_n, \tag{1.50}$$

$$\begin{aligned}\frac{\partial \mathcal{L}}{\partial \alpha_n^*} = &\frac{\mathrm{i}}{2}\dot{\alpha}_n + \frac{\mathrm{i}}{2}\alpha_n \sum_q \left[\lambda_{qn}^* \dot{\lambda}_{qn} - \text{c.c.}\right] \\ &- \sum_m J_{mn}\alpha_m \cdot S_{n,m} \\ &- \alpha_n \sum_q \omega_q |\lambda_{qn}|^2 \\ &+ \alpha_n \sum_q g_{qn}\omega_q(\lambda_{qn} + \lambda_{qn}^*),\end{aligned} \tag{1.51}$$

$$\begin{aligned}\frac{\mathrm{d}}{\mathrm{d}t}\left(\frac{\partial \mathcal{L}}{\partial \dot{\lambda}_{qn}^*}\right) &= -\frac{\mathrm{i}}{2}\frac{\mathrm{d}}{\mathrm{d}t}(|\alpha_n|^2\lambda_{qn}) \\ &= \frac{\mathrm{i}}{2}(\dot{\alpha}_n^*\alpha_n\lambda_{qn} + \alpha_n^*\dot{\alpha}_n\lambda_{qn} + |\alpha_n|^2\dot{\lambda}_{qn}),\end{aligned} \tag{1.52}$$

$$\begin{aligned}\frac{\partial \mathcal{L}}{\partial \lambda_{qn}^*} = &-\frac{\mathrm{i}}{2}|\alpha_n|^2\dot{\lambda}_{qn} \\ &- \sum_m J_{mn}\alpha_n^*\alpha_m(\lambda_{qm} - \frac{1}{2}\lambda_{qn}) \cdot S_{n,m} \\ &- \sum_m J_{mn}\alpha_n^*\alpha_m(-\frac{1}{2}\lambda_{qn}) \cdot S_{n,m} \\ &- |\alpha_n|^2\omega_q\lambda_{qn} \\ &+ |\alpha_n|^2 g_{qn}\omega_q.\end{aligned} \tag{1.53}$$

Rearranging and simplifying the expressions for the partial derivatives we get a first order ODE system for variables $\{\alpha_n, \dot{\alpha}_n, \lambda_{qn}, \dot{\lambda}_{qn}\}$:

$$\dot{\alpha}_n = -\frac{\mathrm{i}}{2}\alpha_n \sum_q \left[\lambda_{qn}^* \dot{\lambda}_{qn} - \text{c.c.}\right]$$

$$
\begin{aligned}
&- \mathrm{i}\sum_m J_{mn}\alpha_m \cdot S_{n,m} - \mathrm{i}\alpha_n \sum_q \omega_q |\lambda_{qn}|^2 \\
&+ \mathrm{i}\alpha_n \sum_q g_{qn}\omega_q \left(\lambda^*_{qn} + \lambda_{qn}\right), \qquad (1.54)\\
\dot{\lambda}_{qn} &= \mathrm{i}\sum_m J_{mn}\frac{\alpha^*_n\alpha_m}{|\alpha_n|^2} S_{n,m}\left(\lambda_{qm} - \lambda_{qn}\right) \\
&- \mathrm{i}\omega_q\lambda_{qn} + \mathrm{i}g_{qn}\omega_q. \qquad (1.55)
\end{aligned}
$$

1.4.4 Equations of motion for the D_2 Ansatz

The derivation for the D_2 Ansatz is similar, using the condition $\lambda_{qn} = \lambda_{qm} \forall m, n$. In this scenario the Debye-Waller factor $S_{n,m} = 1$ and the equations have a simpler form. First the Lagrangian is simplified to

$$
\begin{aligned}
\mathcal{L} = &\frac{\mathrm{i}}{2}\sum_n \left(\alpha^*_n\dot{\alpha}_n - \alpha_n\dot{\alpha}^*_n + |\alpha_n|^2 \sum_q \left[\lambda^*_q\dot{\lambda}_q - \mathrm{c.c.}\right]\right) \\
&- \sum_{m,n} J_{mn}\alpha^*_n\alpha_m - \sum_n |\alpha_n|^2 \sum_q \omega_q|\lambda_q|^2 \\
&+ \sum_n |\alpha_n|^2 \sum_q g_{qn}\omega_q \left(\lambda^*_q + \lambda_q\right). \qquad (1.56)
\end{aligned}
$$

Using the set of variational parameters $\{\alpha^*_n, \lambda^*_q\}$ we have the following form of Euler-Lagrange equations:

$$
\begin{aligned}
\frac{\mathrm{d}}{\mathrm{d}t}\left(\frac{\partial\mathcal{L}}{\partial\dot{\alpha}^*_n}\right) - \left(\frac{\partial\mathcal{L}}{\partial\alpha^*_n}\right) &= 0 \,\forall n, \qquad (1.57)\\
\frac{\mathrm{d}}{\mathrm{d}t}\left(\frac{\partial\mathcal{L}}{\partial\dot{\lambda}^*_q}\right) - \left(\frac{\partial\mathcal{L}}{\partial\lambda^*_q}\right) &= 0 \,\forall\{n, q\}. \qquad (1.58)
\end{aligned}
$$

Explicitly calculating the partial derivatives we have

$$
\begin{aligned}
\frac{\mathrm{d}}{\mathrm{d}t}\left(\frac{\partial\mathcal{L}}{\partial\dot{\alpha}^*_n}\right) &= -\frac{\mathrm{i}}{2}\dot{\alpha}_n, \qquad (1.59)\\
\frac{\partial\mathcal{L}}{\partial\alpha^*_n} &= \frac{\mathrm{i}}{2}\dot{\alpha}_n + \frac{\mathrm{i}}{2}\alpha_n \sum_q \left[\lambda^*_q\dot{\lambda}_q - \mathrm{c.c.}\right] \\
&\quad - \sum_m J_{mn}\alpha_m \\
&\quad - \alpha_n \sum_q \omega_q|\lambda_q|^2
\end{aligned}
$$

$$+\sum_n \alpha_n \sum_q g_{qn}\omega_q(\lambda_q + \lambda_q^*), \tag{1.60}$$

$$\begin{aligned}\frac{\mathrm{d}}{\mathrm{d}t}\left(\frac{\partial \mathcal{L}}{\partial \dot{\lambda}_q^*}\right) &= -\frac{\mathrm{i}}{2}\frac{\mathrm{d}}{\mathrm{d}t}\left(\sum_n |\alpha_n|^2 \lambda_q\right) \\ &= -\frac{\mathrm{i}}{2}\sum_n (\dot{\alpha}_n^* \alpha_n \lambda_q + \alpha_n^* \dot{\alpha}_n \lambda_q + |\alpha_n|^2 \dot{\lambda}_q) \\ &= -\frac{\mathrm{i}}{2}\sum_n |\alpha_n|^2 \dot{\lambda}_q, \end{aligned} \tag{1.61}$$

$$\begin{aligned}\frac{\partial \mathcal{L}}{\partial \lambda_q^*} &= -\frac{\mathrm{i}}{2}\sum_n |\alpha_n|^2 \dot{\lambda}_q \\ &\quad - \sum_n |\alpha_n|^2 \omega_q \lambda_q \\ &\quad + \sum_n |\alpha_n|^2 g_{qn}\omega_q. \end{aligned} \tag{1.62}$$

We use the normalization condition $\sum_n |\alpha_n|^2 = 1$ to obtain the final simplified form of the equations of motion for the variational parameters $\{\alpha_n, \dot{\alpha}_n, \lambda_q, \dot{\lambda}_q\}$:

$$\begin{aligned}\dot{\alpha}_n = &-\frac{\mathrm{i}}{2}\alpha_n \sum_m |\alpha_m|^2 \sum_q g_{qm}\omega_q \left(\lambda_q^* + \dot{\lambda}_q\right) \\ &- \mathrm{i}\sum_m J_{mn}\alpha_m + \mathrm{i}\alpha_n \sum_q g_{qn}\omega_q \left(\lambda_q^* + \lambda_q\right), \end{aligned} \tag{1.63}$$

$$\dot{\lambda}_q = -\mathrm{i}\omega_q \lambda_q + \mathrm{i}\sum_n |\alpha_n|^2 g_{qn}\omega_q. \tag{1.64}$$

One advantage of the simpler D_2 Ansatz is the lack of diverging terms at $|\alpha_n|^2 \to 0$, which allows the stable simulation of dynamics with local site excitations.

1.5 Stochastic extension (sTDVA)

Historically the Davydov Ansatze were used for simulation of dynamics of systems coupled to high-frequency bosonic modes. In this case their energy gap between eigenstates $\hbar\omega \gg kT$, and so the environmental modes could be assumed to be in the ground state prior to any excitation in the system. However, to obtain the density operator at finite temperatures with lower frequency modes an extension of the time-dependent variational approach is needed. Here we use a straightforward procedure by constructing the time-dependent density operator from individually propagated wavefunctions using a Monte-Carlo type procedure. Consider the electronic system being in the ground state. The bath equilibrium density operator is then diagonal

and corresponds to the canonical ensemble. The system contains thermal energy in all vibrational modes. Hence, the temperature of the environment determines the energy and displacements of the environmental modes. The modes prior to optical excitation of the system are in thermal equilibrium and hence can be sampled from the thermal state. The equilibrium density operator of the thermal state is the canonical ensemble:

$$\hat{\rho} = \frac{1}{\mathcal{Z}} \exp\left(-\frac{\sum_q \omega_q \left(\hat{b}_q^\dagger \hat{b}_q + \frac{1}{2} \right)}{kT} \right). \tag{1.65}$$

Using the Glauber-Sudarshan P representation of the equilibrium thermal state[30] for a single mode q we may write the density operator in a coherent state basis:

$$\hat{\rho}^{\mathrm{ph},q}(0) = \int P_q(\lambda_q) |\lambda_q\rangle\langle\lambda_q| \, \mathrm{dRe}\lambda_q \mathrm{dIm}\lambda_q, \tag{1.66}$$

where $P_q(\lambda_q)$ is a generalized probability distribution for each vibrational mode. The $P_q(\lambda_q)$ function is equal to:

$$P_q(\lambda_q) = \mathcal{Z}_q^{-1} \exp\left(-|\lambda_q|^2 \exp\left[\frac{\omega_q}{kT} \right] \right), \tag{1.67}$$

where $\mathcal{Z}_q$ is the partition function of a single harmonic oscillator. Consequently, the initial conditions for the environmental phonon states prior to optical excitation are sampled from distribution (1.67). Due to the lack of coupling between phonon modes of the harmonic bath in the electronic ground state (before optical excitation), the full reduced density operator for the phonon bath can be factorized as $\hat{\rho}^{\mathrm{ph}}(0) = \prod_q \hat{\rho}^{\mathrm{ph},q}(0)$. Note that the mean energy of a phonon mode sampled using the provided $P_q(\lambda)$ function is equal to $\frac{1}{2}\omega_q \coth \frac{\omega_q}{2kT}$, so the high frequency modes of the system are at ground state prior to the excitation of the system.

Random sampling of initial values for the displacements λ_q from the $P_q(\lambda_q)$ distribution and propagation of the equations of motion leads to a set of stochastic realizations $\{R\}$. From these realizations we then explicitly construct all thermally averaged observables, e.g. the reduced density operator for the electronic subsystem with its matrix elements m, n is given by:

$$\rho_{mn}(t) = \langle \alpha_m^*(t) \alpha_n(t) \rangle_R, \tag{1.68}$$

where $\langle \cdots \rangle_R$ denotes averaging over realizations. The mixed state in this approach is constructed by stochastic ensemble averaging of pure states corresponding to individual wavefunctions. Thus, even though a single realization of the sTDVA so-

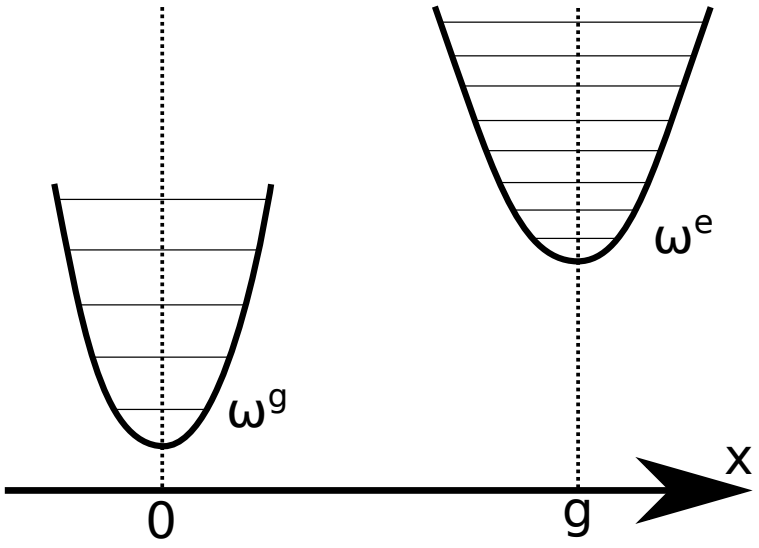

Fig. 1.2. Displaced harmonic oscillator model with a frequency shift

lution is a pure state, the averaging procedure allows us to reconstruct the mixed state density operator. This is the only way the temperature comes in when determining the dynamics of the system. The zero temperature case then corresponds to every environmental oscillator being in the ground state initially (with displacement parameter $\lambda_q = 0$).

1.6 Squeezed coherent state Ansatz

One of the advantages of the TDVA approach is the ability to go beyond bilinear models of system-bath interaction. Here we will apply a new form of variational Ansatz together with a Hamiltonian term for nonlinear corrections. One of the simplest models for nonlinear interactions is that the vibrational modes are harmonic but the phonon frequency is slightly different in the electronic ground and the excited state manifolds (displayed in Figure 1.2).

With the ground state frequency ω^{g} and excited state frequency ω^{e}, the nonlinear interaction Hamiltonian term becomes

$$\hat{H}^{\mathrm{nonlinear}} = \sum_n \hat{a}_n^\dagger \hat{a}_n \sum_q \left(\omega_q^{\mathrm{e}} - \omega_q^{\mathrm{g}}\right) \left(\hat{b}_q^\dagger + \hat{b}_q\right)^2 . \tag{1.69}$$

For calculations of system-bath dynamics in the single excitation manifold we use the Dirac-Frenkel variational approach with a squeezed coherent state Ansatz ($\mathcal{S}_2$) for the global wavefunction, defined as

$$|\mathcal{S}_2(t)\rangle = \sum_n \alpha_n(t)\hat{a}_n^\dagger \cdot \prod_q \hat{D}\left(\lambda_q(t)\right) \hat{S}\left(\xi_q(t)\right) |0\rangle, \tag{1.70}$$

with the displacement and squeezing operators

$$\hat{D}\left(\lambda_q(t)\right) = \exp\left(\lambda_q \hat{b}_q^\dagger - \lambda_q^* \hat{b}_q\right), \tag{1.71}$$

$$\hat{\mathcal{S}}\left(\xi_q(t)\right) = \exp\left(\frac{1}{2}\xi_q \hat{b}_q^{\dagger 2} - \frac{1}{2}\xi_q^* \hat{b}_q^2\right), \tag{1.72}$$

respectively. This is a generalization of the well-known Davydov D_2 Ansatz, with the wavefunction approximated by a product state of local electronic excitations and single squeezed coherent states for each phonon. While Davydov Ansatze have been shown to provide an adequate description in case of linear coupling to harmonic modes, the higher order terms in the Hamiltonian corresponding to nonlinearities and anharmonic corrections can deform Gaussian wavepackets. The squeezing operator expands the Hilbert space spanned by the wavefunction to account for the nonlinear effects. The parameter λ_q corresponds to displacement in the coordinate-momentum space and

$$\xi_q = s_q \exp\left(\mathrm{i}\theta_q\right) \tag{1.73}$$

corresponds to squeezing. The set of parameters $\{\alpha_n(t), \lambda_q(t), \xi_q(t)\}$ follow the equations of motion, which are determined from a set of Euler-Lagrange equations:

$$\frac{\mathrm{d}}{\mathrm{d}t}\left(\frac{\partial \mathcal{L}}{\partial \dot{\alpha}_n^*}\right) - \frac{\partial \mathcal{L}}{\partial \alpha_n^*} = 0, \forall n, \tag{1.74}$$

$$\frac{\mathrm{d}}{\mathrm{d}t}\left(\frac{\partial \mathcal{L}}{\partial \dot{\lambda}_q^*}\right) - \frac{\partial \mathcal{L}}{\partial \lambda_q^*} = 0, \forall q, \tag{1.75}$$

$$\frac{\mathrm{d}}{\mathrm{d}t}\left(\frac{\partial \mathcal{L}}{\partial \dot{\xi}_q^*}\right) - \frac{\partial \mathcal{L}}{\partial \xi_q^*} = 0, \forall q. \tag{1.76}$$

First, let us consider the general case without explicitly specifying the nonlinear term of the Hamiltonian. Using the same definition of the Hamiltonian as in the previous chapters (Eq. (1.23)), we define the Lagrangian as

$$\mathcal{L} = \frac{\mathrm{i}}{2}\left(\langle \mathcal{S}_2(t)|\dot{\mathcal{S}}_2(t)\rangle - \langle \dot{\mathcal{S}}_2(t)|\mathcal{S}_2(t)\rangle\right) - \langle \mathcal{S}_2(t)|\hat{H} + \hat{H}^{\mathrm{nonlinear}}|\mathcal{S}_2(t)\rangle. \tag{1.77}$$

The explicit calculation of all the terms in the Lagrangian is very long and technical, and so here I will provide only a guideline on how to arrive at these results. As in the previous sections, the derivation requires obtaining the time derivative $|\dot{\mathcal{S}}_2(t)\rangle$ and the expectation values of elements of the Hamiltonian. First we obtain the time

derivative of a squeezing operator applied to a vacuum state:

$$\begin{aligned}|\xi_q\rangle &= \hat{S}\left(\xi_q\right)|0\rangle = |s_q, \theta_q\rangle \\ &= \left(\text{sech}s_q\right)^{1/2} \sum_{n=0}^{\infty} \frac{\sqrt{(2n)!}}{n!} \left\{-\frac{1}{2}\exp\left(\text{i}\theta_q\right)\tanh s_q\right\}^n |2n\rangle\,. \end{aligned} \tag{1.78}$$

Applying the same principle of expanding in a number state basis, we have:

$$\begin{aligned}\left|\dot{\xi}_q\right\rangle &= \dot{\hat{S}}\left(s_q, \theta_q\right)|0\rangle = \\ &= \frac{1}{2}\left(\sinh s_q \cdot \left(\text{sech}s_q\right)^{3/2} \cdot \dot{s}_q\right) \\ &\cdot \sum_{n=0}^{\infty} \frac{\sqrt{(2n)!}}{n!} \left\{-\frac{1}{2}\exp\left(\text{i}\theta_q\right)\tanh s_q\right\}^n |2n\rangle \\ &+ \left\{-\frac{\text{i}}{2}\dot{\theta}_q \exp\left(\text{i}\theta_q\right)\tanh s_q - \frac{1}{2}\exp\left(\text{i}\theta_q\right)\cdot \text{sech}^2 s_q \cdot \dot{s}_q\right\} \\ &\cdot \left(\text{sech}s_q\right)^{1/2} \sum_{n=0}^{\infty} \frac{\sqrt{(2n)!}}{n!} n \left\{-\frac{1}{2}\exp\left(\text{i}\theta_q\right)\tanh s_q\right\}^{n-1} |2n\rangle\,. \end{aligned} \tag{1.79}$$

.

Simplifying the equation we obtain:

$$\begin{aligned}\left|\dot{\xi}_q\right\rangle &= \frac{1}{2}\sinh s_q \cdot \dot{s}_q \cdot \hat{S}\left(s_q, \theta_q\right)|0\rangle \\ &+ \left\{-\frac{1}{2}\text{i}\dot{\theta}_q \exp\left(\text{i}\theta_q\right)\tanh s_q - \frac{1}{2}\exp\left(\text{i}\theta_q\right)\cdot \text{sech}^2 s_q \cdot \dot{s}_q\right\} \hat{b}^{\dagger 2}\hat{S}\left(s_q, \nu_q\right)|0\rangle\,. \end{aligned} \tag{1.80}$$

The expression for the time derivative $|\dot{\mathcal{S}}_2(t)\rangle$ follows from calculation of a derivative of a product of functions:

$$\begin{aligned}\left|\dot{\mathcal{S}}_2(t)\right\rangle &= \sum_n \dot{\alpha}_n\left(t\right)\hat{a}_n^{\dagger} \prod_q \hat{D}\left(\lambda_q\right)\hat{S}\left(s_q, \theta_q\right)|0\rangle + \\ &+ \sum_n \alpha_n\left(t\right)\hat{a}_n^{\dagger} \sum_q \dot{\hat{D}}\left(\lambda_q\right)\hat{S}\left(s_q, \theta_q\right) \prod_{k\neq q} \hat{D}\left(\lambda_k\right)\hat{S}\left(s_k, \theta_k\right)|0\rangle \\ &+ \sum_n \alpha_n\left(t\right)\hat{a}_n^{\dagger} \sum_q \hat{D}\left(\lambda_q\right)\dot{\hat{S}}\left(s_q, \theta_q\right) \prod_{k\neq q} \hat{D}\left(\lambda_k\right)\hat{S}\left(s_k, \theta_k\right)|0\rangle\,. \end{aligned} \tag{1.81}$$

Referring to the Eqn. 1.40 for the calculation of the derivative of the displacement

operator applied to the vacuum state, we obtain the kinetic part of the Lagrangian:

$$\mathcal{K} = \sum_n \frac{\mathrm{i}}{2}\left\{\alpha_n^*\dot{\alpha}_n - \dot{\alpha}_n^*\alpha_n\right\} + \frac{\mathrm{i}}{2}\sum_n |\alpha_n|^2 \sum_q \left\{\left(\dot{\lambda}_q\lambda_q^* - \text{c.c.}\right) + \mathrm{i}\dot{\theta}_q \sinh^2 s_q\right\}. \tag{1.82}$$

Calculating the potential part requires obtaining the expressions for expectation values of form $\langle \mathcal{S}_2(t)| \left(\hat{b}_q^\dagger\right)^m \left(\hat{b}_q\right)^n |\mathcal{S}_2(t)\rangle$. While it is still a technical part, I would like to refer to ref.,[30] where expectation values of such ladder operator products in squeezed coherent states are calculated in a general case. The final expression for the Lagrangian is:

$$\begin{aligned}
\mathcal{L} = &\sum_n \frac{\mathrm{i}}{2}\left\{\alpha_n^*\dot{\alpha}_n - \dot{\alpha}_n^*\alpha_n\right\} + \frac{\mathrm{i}}{2}\sum_n |\alpha_n|^2 \sum_q \left\{\left(\dot{\lambda}_q\lambda_q^* - \text{c.c.}\right) + \mathrm{i}\dot{\theta}_q \sinh^2 s_q\right\} \\
&- \sum_{m,n} J_{mn}\alpha_m^*\alpha_n - \sum_n |\alpha_n|^2 \sum_q \omega_q \left(|\lambda_q|^2 + \sinh^2 s_q\right) \\
&+ \sum_n |\alpha_n|^2 \sum_q \omega_q g_{qn}\left(\lambda_q + \lambda_q^*\right) \\
&- \langle \mathcal{S}_2(t)|\hat{H}^{\text{nonlinear}}|\mathcal{S}_2(t)\rangle.
\end{aligned} \tag{1.83}$$

Applying the same procedure of deriving the equations of motion as in previous subsections we get the following equations of motion without an explicit form of the nonlinear contribution term:

$$\begin{aligned}
\dot{\alpha}_n = &-\frac{1}{2}\alpha_n \sum_q \left\{\left(\dot{\lambda}_q\lambda_q^* - \text{c.c.}\right) + \mathrm{i}\dot{\theta}_q \sinh^2 s_q\right\} \\
&- \mathrm{i}\sum_m J_{mn}\alpha_m - \mathrm{i}\alpha_n \sum_q \omega_q \left(|\lambda_q|^2 + \sinh^2 s_q\right) \\
&+ \mathrm{i}\alpha_n \sum_q \omega_q g_{qn}(\lambda_q + \lambda_q^*) \\
&+ \frac{\partial}{\partial \alpha_n^*}\langle S_2(t)|\hat{H}^{\text{nonlinear}}|S_2(t)\rangle,
\end{aligned} \tag{1.84}$$

$$\begin{aligned}
\dot{\lambda}_q = &-\mathrm{i}\omega_q\lambda_q + \mathrm{i}\sum_n |\alpha_n|^2 g_{qn}\omega_q \\
&+ \frac{\partial}{\partial \lambda_q^*}\langle S_2(t)|\hat{H}^{\text{nonlinear}}|S_2(t)\rangle,
\end{aligned} \tag{1.85}$$

$$\dot{s}_q = -\frac{\partial}{\partial \theta_q}\langle S_2(t)|\hat{H}^{\text{nonlinear}}|S_2(t)\rangle \tag{1.86}$$

$$\dot{\theta}_q = 2\omega_q - \frac{1}{\sinh 2s_q}\frac{\partial}{\partial s_q}\langle S_2(t)|\hat{H}^{\mathrm{nonlinear}}|S_2(t)\rangle \tag{1.87}$$

As can be seen here, the squeezing amplitude stays constant if no nonlinear interactions are present in the Hamiltonian. First, this signifies that the D_2 Ansatz is sufficient to describe linear system-bath interactions. Second, the ground state propagator (where the nonlinear terms are absent) is significantly simpler, with the squeezing amplitude in the ground state being $s_q(t) = \mathrm{const}$ and the squeezing phase being $\theta_q(t) = 2\omega_q t + \theta_q(0)$.

Now adding the specific form of the nonlinear term described by Eq. (1.69), we calculate the contributions to the equations of motion:

$$\frac{\partial}{\partial \alpha_n^*}\langle \mathcal{S}_2(t)|\hat{H}^{\mathrm{nonlinear}}|\mathcal{S}_2(t)\rangle = \tag{1.88}$$
$$\mathrm{i}\alpha_n \sum_q \left(\omega_q^{\mathrm{e}} - \omega_q^{\mathrm{g}}\right)\left[\left(\lambda_q^* + \lambda_q\right)^2 - \cos\theta_q \sinh 2s_q + \cosh 2s_q\right],$$

$$\frac{\partial}{\partial \lambda_q^*}\langle \mathcal{S}_2(t)|\hat{H}^{\mathrm{nonlinear}}|\mathcal{S}_2(t)\rangle = \tag{1.89}$$
$$2\mathrm{i}\sum_n |\alpha_n|^2 \left(\omega_q^{\mathrm{e}} - \omega_q^{\mathrm{g}}\right)\left(\lambda_q^* + \lambda_q\right),$$

$$\frac{\partial}{\partial \theta_q}\langle \mathcal{S}_2(t)|\hat{H}^{\mathrm{nonlinear}}|\mathcal{S}_2(t)\rangle = \tag{1.90}$$
$$4\sum_n |\alpha_n|^2 \left(\omega_q^{\mathrm{e}} - \omega_q^{\mathrm{g}}\right)\sin\theta_q,$$

$$\frac{1}{\sinh 2s_q}\frac{\partial}{\partial s_q}\langle \mathcal{S}_2(t)|\hat{H}^{\mathrm{nonlinear}}|\mathcal{S}_2(t)\rangle = \tag{1.91}$$
$$4\sum_n |\alpha_n|^2 \left(\omega_q^{\mathrm{e}} - \omega_q^{\mathrm{g}}\right)\cos\theta_q \left(\coth 2s_q + 1\right).$$

The obtained equations of motion with the nonlinear contributions will be used in Chapter 4 for modeling of nonlinear interactions.

1.7 Observables and optical response of quantum systems

For the spectroscopy simulations presented in this thesis we model the absorption and emission events using a broad-band optical pulse (ideally of an infinitely small duration and infinitely broad spectrum). The elementary optical excitation event (in the sense of perturbation theory) is then realized by acting with the system-field interaction Hamiltonian, $\hat{H}_{\mathrm{F}} = \hat{d}\cdot\boldsymbol{E}$ with

$$\hat{d} = \sum_n \boldsymbol{\mu}_n(\hat{a}_n^\dagger + \hat{a}_n), \tag{1.92}$$

on the electronic ground state leading to the initial excited state

$$|\Psi_{D2}(0)\rangle \equiv \mathcal{N}^{-1} \sum_n (\boldsymbol{\mu}_n \cdot \boldsymbol{E})\, \hat{a}_n^\dagger |0\rangle_e \prod_q |\lambda_q(0)\rangle, \tag{1.93}$$

with $\boldsymbol{E}$ being the electric field vector, $\boldsymbol{\mu_n}$ the site transition dipole vector, $\mathcal{N}$ the normalization of the wavefunction. The direction of the electric field is generated randomly for each realization to account for an arbitrary orientation. This excitation defines the initial conditions for the electronic subsystem and takes into account the orientational properties of the site dipoles.

In this thesis the primary observables of interest are the absorption and time-resolved fluorescence spectra, the occupation probabilities of individual sites or groups of sites and the delocalization length of the excitation. The absorption spectrum is obtained from the linear response theory by calculating the time-domain response functions and averaging over the realizations of both the static disorder and randomly sampled initial conditions for the vibrational states.[2] Using the wavefunction approach we have the following form for the linear absorption:[37]

$$F^{\mathrm{abs}}(\omega) = \mathrm{Re} \int_{-\infty}^{\infty} \mathrm{d}t\, e^{\mathrm{i}\omega t} \sum_R \mathcal{F}^{\mathrm{abs}}{}_R(t), \tag{1.94}$$

where $\mathcal{F}_R(t)$ is the linear optical response function for a single fluctuating trajectory (realization) R. Using the Davydov D_2 Ansatz, it can be explicitly evaluated in terms of dynamical variables α_n, λ_q (Eqns. 1.84,1.85) as the inner product of a state evolving in the ground state manifold and a state evolving in the excited state manifold:

$$\begin{aligned}
\mathcal{F}_R^{\mathrm{abs}}(t) &= \langle \Psi_{D2}(0) | e^{\mathrm{i}\hat{H}_B t} | \Psi_{D2}(t) \rangle \\
&= \sum_{m,n} (\boldsymbol{\mu_m} \cdot \boldsymbol{\mu_n})\, \alpha_m^*(0) \alpha_n(t) \\
&\cdot \exp \sum_q \Big(e^{\mathrm{i}\omega_q t} \lambda_q^*(0) \lambda_q(t) \\
&- \frac{1}{2} \left[|\lambda_q(0)|^2 + |\lambda_q(t)|^2 \right] \Big),
\end{aligned} \tag{1.95}$$

with $\hat{H}_B = \sum_q \omega_q \hat{b}_q^\dagger \hat{b}_q$. The time-resolved auxiliary fluorescence optical response function[38] is calculated similarly:

$$F^{\mathrm{trf}}(\omega, \tau) = \mathrm{Re} \int_{-\infty}^{\infty} \mathrm{d}t\, e^{\mathrm{i}\omega t} \sum_R \mathcal{F}^{\mathrm{trf}}{}_R(t, \tau), \tag{1.96}$$

where the contribution from a single realization is given by

$$\begin{aligned}\mathcal{F}_R^{\mathrm{trf}}(t,\tau) &= \langle \Psi_{D2}(\tau)|\hat{d}e^{\mathrm{i}\hat{H}_{\mathrm{B}}t}\hat{d}|\Psi_{D2}(t)\rangle \\ &= \mathcal{S}_{\mathcal{R}} \cdot \sum_{m,n} \left(\boldsymbol{\mu}_{\mathbf{m}} \cdot \boldsymbol{\mu}_{\mathbf{n}}\right) \alpha_m^*(\tau)\alpha_n(t) \\ &\cdot \exp \sum_q \Big(e^{\mathrm{i}\omega_q(t-\tau)} \lambda_q^*(\tau)\lambda_q(t) \\ &-\frac{1}{2}\left[|\lambda_q(\tau)|^2 + |\lambda_q(t)|^2\right] \Big), \end{aligned} \tag{1.97}$$

with $\mathcal{S}_{\mathcal{R}} = \sum_n (\boldsymbol{E} \cdot \boldsymbol{\mu_n})^2$ being the weight factor for the realization characterizing its excitation probability. This expression is analogous to absorption except the time arguments are shifted to allow the partial equilibration in the electronic excited state for a time period τ.

For the optical response calculations with squeezed coherent states the expressions are slightly more complicated due to the overlap of two squeezed coherent states. In the case of linear absorption measurements we have

$$\begin{aligned}\mathcal{F}_R^{\mathrm{abs}} &= \langle \mathcal{S}_2(0)|\mathrm{e}^{\mathrm{i}\hat{H}_{\mathrm{B}}t}\mathrm{e}^{-\mathrm{i}\hat{H}t}|\mathcal{S}_2(0)\rangle \\ &= \sum_{m,n} \left(\boldsymbol{\mu}_m \cdot \boldsymbol{E}\right)\left(\boldsymbol{\mu}_n \cdot \boldsymbol{E}\right) \alpha_m^*(0)\alpha_n(t) \\ &\cdot \langle \lambda(t), s(t), \theta(t)|\lambda'(t), s'(t), \theta'(t)\rangle, \end{aligned} \tag{1.98}$$

where we denote the electric field polarization vectors of the measurement apparatus as $\boldsymbol{E}$.

The $\langle \lambda(t), s(t), \theta(t)|\lambda'(t), s'(t), \theta'(t)\rangle$ term is the vibrational overlap integral for two distinct squeezed coherent states (writing the squeezing parameter in polar form), and is expressed as:

$$\begin{aligned}\langle \lambda, s, \theta|\lambda', s', \theta'\rangle = \frac{1}{\sqrt{\zeta}} \exp\Bigg[&-\frac{|\lambda|^2 + |\lambda'|^2}{2} + \frac{\lambda^*\lambda'}{\zeta} \\ &+ \frac{\lambda^{*2}}{2\zeta}\left(e^{-i\theta'}\cosh s \cdot \sinh s' - e^{-i\theta}\cosh s' \cdot \sinh s\right) \\ &+ \frac{\lambda'^2}{2\zeta}\left(e^{i\theta}\cosh s' \cdot \sinh s - e^{i\theta'}\cosh s \cdot \sinh s'\right)\Bigg], \end{aligned} \tag{1.99}$$

where

$$\zeta = \cosh s \cdot \cosh s' - e^{i\left(\theta' - \theta\right)} \sinh s \cdot \sinh s'. \tag{1.100}$$

Similarly, for the ATRF signal we have the two-time response function as

$$\begin{aligned}\mathcal{F}_R^{\mathrm{trf}}(t,\tau) &= \langle \mathcal{S}_2(\tau)|\hat{d}\mathrm{e}^{\mathrm{i}\hat{H}_{\mathrm{B}}t}\hat{d}|\mathcal{S}_2(t)\rangle\Big\rangle \\ &= \sum_{m,n}\frac{1}{3}\left(\boldsymbol{\mu}_m\cdot\boldsymbol{\mu}_n\right)\alpha_m^*(\tau)\alpha_n(t) \\ &\quad \langle\lambda(t),s(t),\theta(t)|\lambda'(t),s'(t),\theta'(t)\rangle.\end{aligned} \tag{1.101}$$

One observable of interested used throughout the thesis is the site/exciton occupation probability. It is straightforwardly calculated both in site and excitonic bases as the diagonal element of the electronic excited state density operator $\hat{\rho}_{mn}(t)$ (defined in Eq. (1.68)), taken either in site or respectively excitonic basis. So for site n its occupation probability is equal to $\rho_{nn}(t)$. Another important set of observables also follows from the calculated density operators: to investigate the localization behaviour of the excitonic states we use three quantities. The first one is the exciton participation ratio which is defined as:

$$L(t) = \langle\left(\sum_n |\alpha_n(t)|^4\right)^{-1}\rangle, \tag{1.102}$$

here angular brackets denote thermal averaging. The second one is the site coherence length:[39]

$$L^{[2]}(t) = \sum_{m\neq n}|\hat{\rho}_{mn}(t)|. \tag{1.103}$$

Similarly, we obtain the third parameter, the excitonic coherence length as

$$L_e^{[2]}(t) = \sum_{m\neq n}|\hat{\rho}_{mn}^{exc}|, \tag{1.104}$$

where $\hat{\rho}_{mn}^{exc}$ is the density operator in the eigenbasis of the electronic Hamiltonian (obtained by a unitary transformation). It represents the quantified amount of coherence between distinct excitonic states. The density operators are normalized according to the condition

$$\mathrm{Tr}\hat{\rho}^{\mathrm{el}} = \mathrm{Tr}\hat{\rho}^{\mathrm{exc}} = 1. \tag{1.105}$$

In contrast to static models, all parameters are averages of time-dependent stochastic quantities and include the dynamic disorder. The three definitions become very important to investigate the effect of finite temperature on exciton delocalization to isolate the dephasing effects of the thermal environment.

Chapter 2

Formation of excitonic polarons

2.1 Introduction

Electronic excitation in translationally invariant lattices (e. g. molecular crystals) is usually completely delocalized. However, the molecular excitation induces the redistribution of the electron density in the molecule and in its local molecular environment, which could be solvent molecules in solutions, polymer matrix in films, or protein surrounding in biological pigment-protein complexes. Such static polarization field can essentially affect the relationship of coherent superpositions between the molecular excitations and reshape the exciton states. In the case when the energy of the induced polarization is large in comparison with the characteristic energy of intermolecular interactions[6,40,41] the exciton self-trapping process, named the *excitonic polaron* formation in analogy to the electronic polaron known in crystals, is expected. The possible appearance of the excitonic polaron states has been revealed by analyzing absorption and fluorescence spectra of various molecular crystals and films.[42–44] More recently such concepts were applied to polymers[45] and photosynthetic pigment-protein complexes.[46–48] Polaron formation thus changes the system states from "free" or infinite radius states to "self-trapped" or finite radius states. On the other hand, realistic molecular aggregates and polymers often possess a high degree of conformational disorder and so the excitation is localized to some extent over several molecules. Thus the excitonic polaron formation in this case does not change the character of system states completely. However, compared to excitons, the polarons have more compact localization, different energies and a reduced bandwidth.[46,49]

Variational methods are often applied to large systems possessing translational invariance, like molecular crystals. The quantities of interest in these studies are the polaron ground state energy, the effective bandwidth and the effective mass.[50–54] The static polaron properties are obtained, yet the dynamics of polaron formation

are usually ignored. In this chapter, we focus on the dynamical irreversible picture of polaron formation and analyze how the Brownian environment affects this process. Hence, the phonons in our treatment represent the overdamped harmonic bath having a continuous spectral density. To capture the qualitative character of polaron formation dynamics starting from an optical exciton in a disordered molecular aggregate, we perform numerical simulations on the simplest two-site molecular aggregate (a heterodimer), which exhibits very rich excitation dynamics[12,20,55,56] despite the small number of sites.

In this chapter we use the D_1 Ansatz to construct the general procedure for investigating the excitation dynamics in systems coupled to the bath. The approach, described in Chapter 1.3, allows to directly evaluate the full polaronic effective Hamiltonian, which appears to be a complex-valued matrix hence including damping effects. Time dependence of the effective coupling is used to define the polaron formation timescale and as a guidance to understand distinct system evolution regimes.

2.2 Model parameters

We use a simple electronic block Hamiltonian (as in Eqn. (1.13)) given by

$$\hat{H}_{\mathrm{s}} = \begin{pmatrix} 0 & J \\ J & \Delta \end{pmatrix}. \tag{2.1}$$

The values $J = -100\,\mathrm{cm}^{-1}$ and $\Delta = 100\,\mathrm{cm}^{-1}$ represent realistic molecular aggregates of dyes or photosynthetic complexes. As described in Chapter 1.1, the excitonic Hamiltonian is obtained from $\hat{H}_{\mathrm{s}}$ by direct diagonalization. Here we assume that each phonon mode is coupled to a single site, and thus fluctuations of site energies are independent. The quantum overdamped Brownian oscillator model is used for the environment, with its spectral density function defined as[57]

$$C''(\omega) = \frac{4\Lambda\gamma^3\omega}{\left(\omega^2+\gamma^2\right)^2}. \tag{2.2}$$

It depends on two characteristic parameters: the reorganization energy Λ and the characteristic relaxation rate γ. This spectral density implies the exponential decay ($\sim \exp(-\gamma t)$) of the bath correlation function of environmental fluctuations,[6,26] which allows to describe the dephasing and relaxation processes. In order to obtain different regimes of the evolution we use four distinct cases for the spectral density function parameters: Markovian environment (fast bath relaxation) with large reorganization energy $\left(\gamma^{-1} = 10\,\mathrm{fs},\ \Lambda = 100\,\mathrm{cm}^{-1}\right)$, Markovian environment with

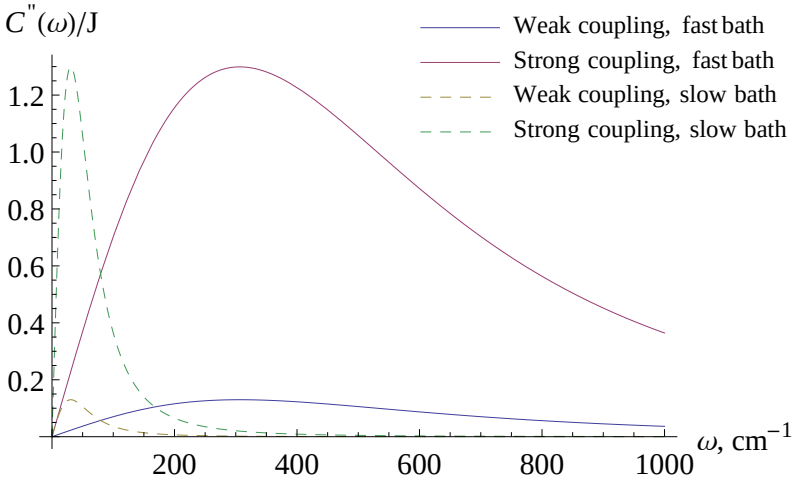

Fig. 2.1. Spectral density functions of the environment scaled by the resonant interaction strength J.

small reorganization energy $\left(\gamma^{-1} = 10\,\mathrm{fs},\ \Lambda = 10\,\mathrm{cm}^{-1}\right)$, slow bath with large reorganization energy $\left(\gamma^{-1} = 100\,\mathrm{fs},\ \Lambda = 100\,\mathrm{cm}^{-1}\right)$ and slow bath with small reorganization energy $\left(\gamma^{-1} = 100\,\mathrm{fs},\ \Lambda = 10\,\mathrm{cm}^{-1}\right)$. Similar parameters have been used in simulations of optical spectra of various molecular complexes[18,58] and theoretical investigations.[12,59,60] All used spectral density functions are shown in Fig. 2.1. As we will demonstrate further, these cases give distinct qualitative characteristics in the time evolution of the excitons.

The total phonon bandwidth W is chosen depending on the relaxation rate γ so that the coupling strength of the largest considered frequency $g(W)$ is taken to be approximately 1% of the maximum coupling strength g_{max}. Explicitly in case of the fast bath the phonon bandwidth was set to $2000\,\mathrm{cm}^{-1}$ and in the case of slow bath the cutoff frequency was set at $500\,\mathrm{cm}^{-1}$. In order to achieve numerical convergence in our simulations we used 1000 modes per site, which is sufficient for our spectral density. In general the number of the modes required to achieve convergence depends on the shape of the spectral density function, e.g. for the Debye spectral density[12] the required number must be higher because of the slower coupling strength decay at high frequencies.

For the initial conditions (at $t = 0$) we set the electronic excitation vector $\begin{pmatrix} \alpha_1 \\ \alpha_2 \end{pmatrix}$ as the eigenvector of the electronic Hamiltonian $\hat{H}_\mathrm{S}$ in site basis corresponding to the optically prepared higher energy excitonic state, with its amplitudes equal to $\begin{pmatrix} -0.526 \\ 0.851 \end{pmatrix}$. All the initial displacements of the phonons $\lambda_{qn}(t = 0)$ are set to zero as the bath is in the ground state before excitation. As a reference, for this initial condition the site populations would remain stationary if the system was not coupled

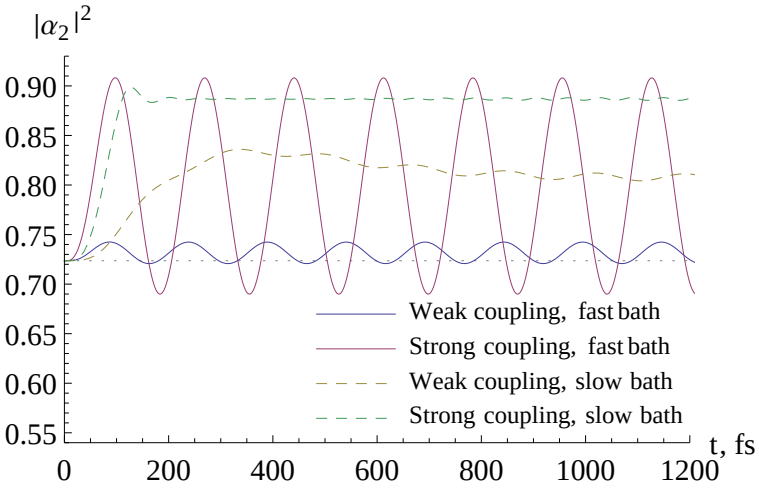

Fig. 2.2. Time dependences of site 2 electronic state populations. Dotted line denotes the initial population of the corresponding state.

to the bath, i.e. $g_{qn} = 0$. Additionally, when $g_{qn} = 0$, other initial conditions, which are not eigenvectors of the bare Hamiltonian (e.g. single site excitation), would result in quantum oscillations of the site populations (these are known as Rabi oscillations), arising from the resonant coupling J. When the coupling between the system and the bath is switched on, the optically prepared eigenvector of the bare Hamiltonian is no longer a stationary solution and relaxation dynamics of the site populations of the composite system must take place. In the following we study the dynamics for several types of the bath.

2.3 Population dynamics

The evolutions of the populations $|\alpha_2|^2$ with different bath parameters are shown in Fig. 2.2, while $|\alpha_1|^2 = 1 - |\alpha_2|^2$ follows the from normalization condition. Notice that in this representation we can discuss the exciton delocalization explicitly: if $|\alpha_1|^2 = |\alpha_2|^2 = 0.5$, the state is completely delocalized (the populations are distributed evenly among the sites), while $|\alpha_n|^2 = 1$ denotes complete localization. First, let us consider dynamics with fast (Markovian) bath. In the case of weak system-bath coupling, the populations of the excited states show small amplitude oscillations around the initial values, which correspond to a stationary state of the pure excitonic Hamiltonian. Thus, in this case the bath induced effects on the electronic system dynamics are minimal. By increasing the reorganization energy, the amplitude of oscillations increases and oscillations are shifted away from the initial population lines, thus the excitation becomes more localized. Stronger system-bath coupling thus leads to self-trapping, or excitonic polaron formation. The remaining Rabi oscillations reflect the coherence between sites, or the existence of a new polaronic basis, which is delocalized between the sites.

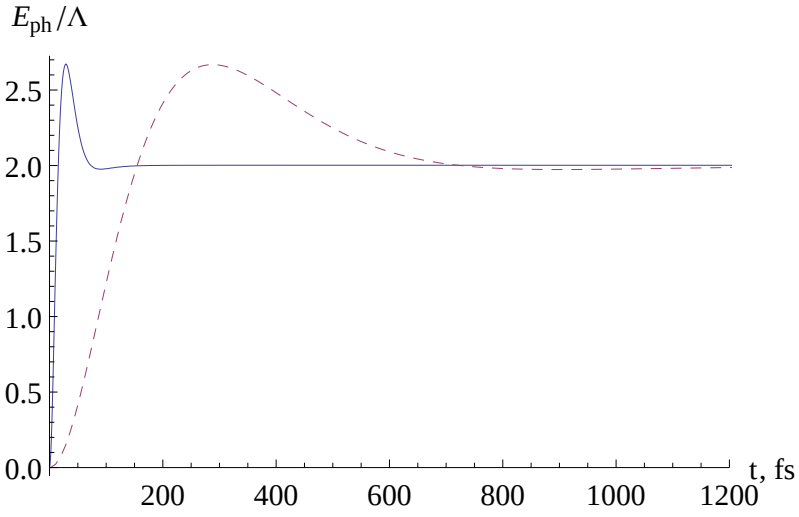

Fig. 2.3. Evolution of the total phonon field energy of the system, scaled by the reorganization energy Λ. Solid line corresponds to the fast bath ($\gamma^{-1} = 10\,\mathrm{fs}$), dashed line corresponds to the slow bath ($\gamma^{-1} = 100\,\mathrm{fs}$).

In the case of a slow bath, the evolution of the electronic populations demonstrates dynamic decoherence and localization. This self-trapping process is qualitatively different from fast reversible oscillations, observed in the case of the fast bath. The effects of increased system-bath coupling are twofold. First, a stronger coupling leads to a more localized state. Second, it quenches all oscillatory behavior.

As indicated above, the four cases described above demonstrate that the initial optically prepared excitonic eigenstate is not the stationary state of the full system including the environment. However, in the case of weak coupling to the fast bath the minimal deviations from the pure excitonic case indicate that the purely excitonic picture holds. In all other considered cases we have a qualitative change, which we denote as the excitonic polaron formation. Its formation dynamics are very dependent on the bath timescale.

Another observable in the evolution of the system is the total energy of the phonon field, which can be evaluated as

$$E_{\mathrm{ph}} = \sum_n |\alpha_n|^2 \sum_q \omega_q |\lambda_{qn}|^2. \tag{2.3}$$

As demonstrated in Fig. 2.3 the normalized phonon energy behaves similarly in all four cases under consideration. Its evolution is determined only by the relaxation time of the environment and scales linearly with the reorganization energy. Hence, from the point of view of the environment, all four systems behave identically.

2.4 Effective Hamiltonian

The equilibrium density operator of excitonic states is not described by the bare excitonic Boltzmann distribution, since the bath effectively reduces the excitonic bandwidth.[12] Using the present theory we can introduce the effective system Hamiltonian by inspecting the very equations of motion. Our system of interest can be mapped to an effective two-level system with its electronic Hamiltonian elements depending on time, i.e., the phonon field being absorbed by the effective system parameters: site energies and inter-site couplings:

$$\hat{H}_{eff} = \begin{pmatrix} \epsilon_1(t) & J_{eff}(t) \\ J_{eff}(t) & \epsilon_2(t) \end{pmatrix}.$$

We have the same dynamics of the electronic amplitudes as calculated using the equations of motion (1.54)-(1.55) when the above matrix is given by :

$$\epsilon_1(t) = -\frac{1}{2}\sum_q g_{q1}\omega_q(\lambda_{q1} + \lambda_{q1}^*), \tag{2.4}$$

$$\epsilon_2(t) = -\frac{1}{2}\sum_q g_{q2}\omega_q(\lambda_{q2} + \lambda_{q2}^*) + \Delta, \tag{2.5}$$

$$\begin{aligned} J_{eff}(t) = \frac{3}{2}JS_{1,2}\sum_q \left[|\lambda_{q1}|^2 - \lambda_{q1}^*\lambda_{q2}\right] \\ + J\frac{\alpha_2^*\alpha_1}{\alpha_2\alpha_1^*}S_{2,1}\sum_q \left[|\lambda_{q1}|^2 - \lambda_{q2}^*\lambda_{q1}\right]. \end{aligned} \tag{2.6}$$

In the present case, where the spectral density is the same for both sites, the difference $\epsilon_2(t) - \epsilon_1(t) = \text{const}$, while the effective coupling $J_{eff}(t)$, shown in Figs. 2.4 and 2.5, determines all characteristics of the dynamics of the electronic amplitudes. Inspecting closer both the real and the imaginary parts we notice that the full evolution of J_{eff} consists of a primary envelope governed by the first term in Eq. (2.6) with the second term determining the rotation around the primary term in the complex plane, dependent on the relative phases of the electronic excitation amplitudes.

The complex-valued effective Hamiltonian is a clear indication of dissipative phenomena. In the phenomenological description of relaxation, the finite lifetimes of the states can be often accounted for by adding imaginary parts to the energies $\epsilon_n \rightarrow \epsilon_n + \mathrm{i}/\tau_n$. The imaginary part of the effective coupling hence contains a similar time-dependent damping.

The real part of J_{eff} shows different evolutions for different regimes of parameters (see Fig. 2.4). In the case of the fast bath and weak coupling, its amplitude stays

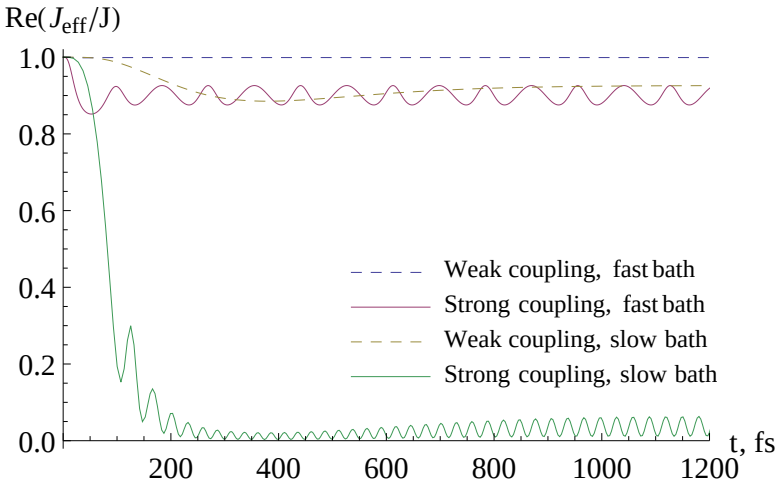

Fig. 2.4. Evolution of the J_{eff} real parts with different reorganization energies and relaxation timescales.

approximately the same at all times, while closer inspection reveals a very fast drop with subsequent stabilization and oscillations (however, the change is only within 0.1%). Increasing the system-bath coupling strength noticeably increases the deviation from the initial value and oscillations. Turning to the case of the slow bath and weak coupling, the real part of J_{eff} shows a slow decay without any noticeable oscillations. However, when the system-bath coupling is stronger, the amplitude of J_{eff} drops dramatically with discernible oscillations in this case. Decay of the effective coupling with the increase of the system-bath coupling qualitatively agrees with an empirical formula obtained for the Debye bath at finite temperature in ref.[12] The imaginary part of J_{eff} (see Fig. 2.5) adds additional phase factors to the amplitudes.

Analysis of the real part of J_{eff} allows us to explain the different regimes of electronic population evolutions shown in Fig. 2.2. In the case of the weak coupling to the fast bath, the real part of J_{eff} remains almost constant and correspondingly, the electronic populations remain unaffected. With stronger coupling J_{eff} drops by almost 10% and induces some localization. It is also the case with the weak coupling to the slow bath. When the electronic system is strongly coupled to the slow bath, the amplitude of the real part of J_{eff} drops dramatically and, consequently, the electronic amplitudes become more localized than in all other cases under consideration.

Whether the electronic populations show oscillations or slow relaxation can be explained considering the rate of change of the effective coupling compared to the timescale of excitonic coherence oscillations, which given by the reciprocal excitonic bandwidth of the coupled system ($\sqrt{4J^2 + \Delta^2} \backsimeq 220$ cm^{-1} giving a 152 fs oscillation period in our case). In the case of the fast bath the real part of J_{eff}

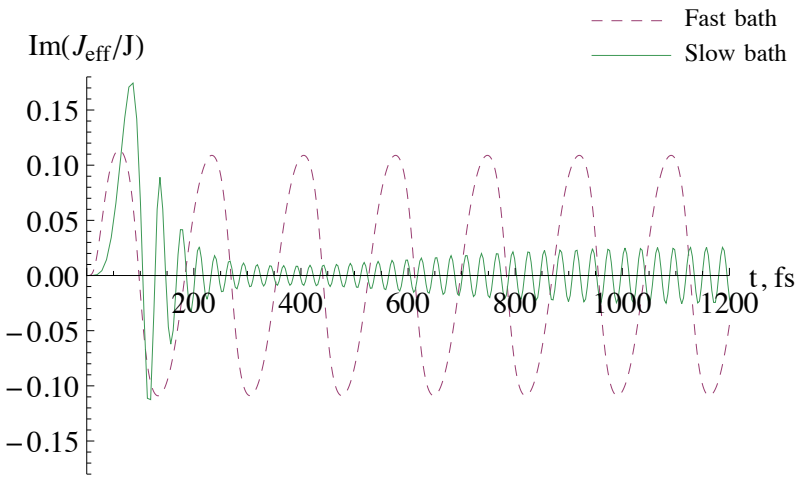

Fig. 2.5. Evolution of the J_{eff} imaginary parts in the case of strong system-bath coupling.

changes rapidly over a timescale of about 30 fs, thus, the change in the effective coupling is abrupt compared to the intrinsic frequencies of the wavefunction. This rapid change generates a "quantum leap" followed by Rabi oscillations with respect to the "new" system. When the system-bath coupling is weak, this deformation is vanishing and can be ignored. When the system-bath coupling is strong, the excitonic amplitudes are affected considerably and we can denote the new states as the coherent polaron states formed in the *non-adiabatic* regime. On the other hand, the slow evolution of J_{eff} caused by long relaxation times of the environment is on timescales longer than the excitonic coherence oscillations, which leads to an adiabatic relaxation in the system. Consequently, this is the *adiabatic* regime of the excitonic polaron formation, and the resulting polaron is highly incoherent.

The timescale of polaron formation can be obtained from the time that J_{eff} needs to stabilize. From Fig. 2.4 we see that in the nonadiabatic polaron formation regime it is $\sim 100\,\mathrm{fs}$, while in the adiabatic regime it is $\sim 300\,\mathrm{fs}$. The polaron formation timescale is thus deeply related to the timescale of bath relaxation.

Our results show that the excitonic picture is only then not perturbed when the bath relaxation is fast and the coupling to the bath is weak. In other case we observe excitonic polaron formation. The first condition can be quantified by comparing the reciprocal resonant coupling to the characteristic bath timescale. For the second condition we should compare the resonant coupling to the reorganization energy. Note that usually only this condition is considered in the literature,[6,41] while this study shows that the bath timescale is also an important factor in polaron formation dynamics. It follows from our analysis that the excitonic polaron forms when either $\Lambda \gtrsim J$ or $\gamma^{-1} > J^{-1}$. When the latter condition is satisfied, the excitonic polaron formation proceeds in the adiabatic regime irrespective of Λ and we obtain the

incoherent polaron. When $\gamma^{-1} < J^{-1}$ and $\Lambda \gtrsim J$ we have the non-adiabatic polaron formation which leads to the coherent polaron. These findings are fully consistent with our previous calculations.[12]

Excitonic polaron formation conditions described above are expressed using two bath parameters: the reorganization energy Λ and the timescale γ^{-1}. While the former is a well-defined characteristic, the timescale cannot be unambiguously defined for an arbitrary spectral density, since the fluctuation correlation function may decay non-exponentially. However, the characteristic timescale of the environment relaxation could be estimated as[61] :

$$\tau_{chr} = \frac{1}{\Lambda} \int_0^\infty \Gamma(t)\, \mathrm{d}t. \tag{2.7}$$

Here $\Gamma(t)$ is the phonon relaxation function, which can be obtained from fluorescence Stokes shift experiments.[62] It is related to the spectral density by

$$\Gamma(t) = \int_{-\infty}^{\infty} \frac{C''(\omega)}{\omega} \cos(\omega t) \frac{\mathrm{d}\omega}{2\pi}. \tag{2.8}$$

For the quantum overdamped Brownian oscillator spectral density function we obtain

$$\tau_{chr}^{QOD} = \frac{2}{\gamma}. \tag{2.9}$$

For environments described by other spectral densities one would have to compare τ_{chr} with J^{-1} when considering polaron formation.

In this work the phonon field is chosen to represent an overdamped environment. This means it can show relaxation and dephasing dynamics. This is in contrast to investigations where only a limited number of explicitly chosen phonon modes corresponding to specific intra- and/or intermolecular vibrations are considered and the total system is thus closed. Polaron formation due to high frequency intramolecular vibrational modes is extensively studied.[45,63,64] Here we show that the Brownian environment is another source of polaron formation, which should be accounted even at zero temperature. It is straightforward to add the intra- and/or intermolecular vibrational modes with their respective couplings (Huang-Rhys factors) explicitly to the continuous environmental spectral density by adding weighted delta functions at corresponding frequencies, but this is out of scope of this thesis.

Usually, the weak coupling in the Markovian bath limit is analyzed in the context of the Redfield relaxation theory,[26,65] which is formulated in the purely excitonic basis. We find that there is no excitonic polaron formation in this regime and, thus, the

Redfield picture holds perfectly. However, in the case of the slow bath, the Redfield approach breaks down even in the case of the weak coupling with the bath.[66] In light of our results, this can be explained by the decrease of the effective coupling and emergence of polaronic states. In the case of the strong system-bath coupling and weak inter-molecular couplings, the Förster theory should be invoked,[67,68] which, as was recently demonstrated, provides good agreement with exact calculations in the case of the fast bath.[18] However, in the case of the slower bath the Förster theory provides noticeably faster excitation transfer rates compared to the exact calculations. The Förster transfer rate between two molecules is proportional to the square of the inter-molecular resonant coupling. As it is demonstrated here, in the case of the slow bath, the coupling between the sites is reduced, thus the real transfer rate should become slower than the one estimated by the Förster theory.

2.5 Conclusions

We have performed simulations of excitonic polaron transition dynamics using a two-site molecular aggregate. Despite the small size the dimeric system already shows excitonic effects: excitonic energy splitting and redistribution of transition dipole moments.[6] Moreover, such systems are common in nature. Dimers are typical constituents of various molecular crystals.[69] They are also relevant, because strong disorder can induce localization of excited states even in translational invariant molecular systems.[70,71] Additionally, photosynthetic complexes often contain dimeric elements. The reaction centers, where charge separation occurs[72–75] , contain two very closely interacting molecules. Dimers are also the simplest aggregates that can be created artificially. Recently, a series of heterodimers were engineered in order to study the coherence between the excited states and its spectroscopic signatures.[76] Thus, our theory applies to arbitrary molecular aggregates, while our results are directly useful for studies of small molecular systems with complex geometry, molecular crystals and aggregates possessing impurities that break translational invariance.

Polaronic effects should be taken into account when considering the charge transfer (CT) processes in molecular systems. A recent attempt to describe the excitation dynamics in the reaction center of plant photosystem II showed deviations from experimental data at short timescales.[58] The CT states interact strongly with their environment,[58,77,78] thus, the system-bath interaction should quench couplings of the CT states with other CT states, or with excitonic states, especially if the bath is not Markovian. This should affect system dynamics in two ways. First, the initial time evolution of the system would be heavily influenced by polaron formation dynamics. Second, the quenched coupling should slow down energy or charge transfer

between the relaxed states. As such, we propose the excitonic polaron formation mechanism as a viable candidate for the explanation of this discrepancy.

Here we considered only the zero temperature case, hence, our simulated evolution reveals the lowest energy excitonic polaron state, which is mostly relevant for exciton trapping.[51] Thus the results of this chapter are most relevant when analyzing real systems at low temperatures.[79] The qualitative agreement with a study done using a formally exact calculational approach (HEOM),[12] where the high temperature case was considered, means that the main features of excitonic polaron formation are also valid at higher temperatures. However, the question whether the excitonic polaron formation makes a significant impact on the observables at higher temperatures still remains, and a more detailed analysis of the temperature effects in polaron formation dynamics will be the foundation of the next chapter.

Chapter 3

Polaronic effects at finite temperature

3.1 Introduction

Two theoretical schemes are commonly used to represent the limiting cases used for the description of the excitation evolution in molecular aggregates at finite temperature. Taking the bare exciton states as a perpetual representation of the molecular aggregate not changeable in the course of time after excitation, the time-resolved exciton evolution is usually attributed to relaxation processes defined by exciton interaction with a vibrational bath. This type of behavior is qualitatively easily explained in terms of the Redfield theoretical scheme. In the case when the intermolecular interaction is weak compared to the coupling to phonons, the excitation dynamics are described in the real space site representation and the resonance interaction is treated perturbatively in terms of the Förster theory. Such type of approximations are commonly used when trying to model the electronic excitation dynamics. In realistic molecular aggregates, such as photosynthetic systems, the couplings between monomers can be of the same order as couplings to vibrations, which makes the perturbation theory a rough approximation. When there is no small parameter, the perturbational approaches fail. The simplest approximate treatment is possible when timescale separation is possible, e. g. when electronic dynamics are fast, while phonons are slow. The nonlinear Schrödinger equation can then be derived, which signifies the transformation of excitons into polarons. This can be understood in terms of a feedback relation between excitons and phonons. When the timescale separation is unavailable, the time dependence can still be treated approximately up to the desired accuracy using the variational approaches, where the accuracy solely depends upon the choice of trial wavefunctions. In these approaches the interaction between sites and their local phonons may cause non-uniform polarization of the immediate environment, creating excitonic polarons (as discussed in the previous chapter).

Performing measurements on molecular aggregates at zero temperature is technically impossible, and very low temperatures (below 4K) are difficult to achieve in an experimental setup. The vast majority of the experimental spectroscopic data exists at either liquid nitrogen temperature (77K) or room temperature (300K). So for modeling of population dynamics and optical spectra a pure single-wavefunction approach becomes unsuitable, requiring ensemble-based methods, such as the stochastic time-dependent variational approach presented in this thesis. In this chapter we will first test the validity of the approach in different parameter regimes, and then proceed to the modeling of dynamics in a real photosynthetic aggregate, the LH2 complex.

3.2 Benchmarking the stochastic time-dependent variational approach

3.2.1 Introduction

Non-perturbative theories that make no assumptions on the relative strength of interactions have become available in recent decades.[7–10] For example, the approach based on hierarchical equations of motion (HEOM) has been applied to study model systems with various strengths of resonant interactions between molecules and with the inter- and intra-molecular vibrations.[11–15] It has also been used to describe time resolved spectroscopy experiments.[16–21] Nevertheless, exact theories are usually very expensive computationally, and sometimes limited to rather structureless vibrational baths. Therefore in practice their application is often limited. This leads to a search for alternative non-perturbative theories that could possibly be used in the intermediate coupling regime.[80–82]

The application of the TDVA is thus very promising as the method is not perturbative, and is not expected to fail for specific ranges of parameters. Moreover, this approach allows one to keep track of bath degrees of freedom explicitly. This is of great advantage for nonlinear optical response function calculations, as correlations between different time intervals of the free system propagation without the optical field are accounted for. In comparison, when using reduced master equation based approaches, each time interval of the response function is described by an independent equation and dynamics in all time intervals become uncorrelated.[83,84] Previously, the validity of the TDVA was examined for the zero temperature case.[85] The approach was extended (called sTDVA for stochastic TDVA) to include the finite temperature case via stochastic sampling of the initial conditions, as described in section 1.5 of the thesis. This opened a possibility for a direct comparison with exact methods over a wide parameter range, which is the goal of the present study.

Here, we present a systematic comparison of the excitation dynamics obtained with sTDVA for different interaction parameters and temperatures with the exact HEOM approach. First, we compare population evolutions for a molecular dimer in three parameter regimes: when the resonant coupling is small, when the interaction with the vibrations is small, and when both parameters are of similar strength. We also calculate absorption and auxiliary time resolved fluorescence spectra[38] to determine whether the sTDVA can reproduce accurate spectral lineshapes.

3.2.2 Model parameters

We used a heterodimer as the model system, with the electronic Hamiltonian as follows:

$$\hat{H}_{\mathrm{el}} = \begin{pmatrix} 0 & J \\ J & \Delta \end{pmatrix}. \tag{3.1}$$

The state energies are assumed to be shifted by an optical energy gap which is not important for our calculations. The three used sets of parameters were chosen to represent either the *weak system-bath coupling regime* (a), with reorganization energy much smaller than the inter-site resonant coupling, the *weak resonant coupling regime* (b), when the resonant coupling is small in comparison to the reorganization energy, or the *intermediate regime* (c) when both parameters are equal. The exact values that we used for modeling are a) $J = 100\,\mathrm{cm}^{-1}$, $\Lambda = 20\,\mathrm{cm}^{-1}$, b) $J = 20\,\mathrm{cm}^{-1}$, $\Lambda = 100\,\mathrm{cm}^{-1}$, c) $J = 100\,\mathrm{cm}^{-1}$, $\Lambda = 100\,\mathrm{cm}^{-1}$. The energy gap Δ was set equal to $100\,\mathrm{cm}^{-1}$. We fixed the bath correlation timescale to $\gamma^{-1} = 100\,\mathrm{fs}$. These parameters are similar to those of realistic pigment-protein complexes,[6] and a similar set of parameters was used in the previous chapter. The initial condition for the electronic subsystem state was chosen as

$$\hat{\rho}(0) = \begin{pmatrix} 0 & 0 \\ 0 & 1 \end{pmatrix}, \tag{3.2}$$

which corresponds to only the higher energy site being excited at the initial time. This initial condition was used in both population evolution and auxiliary TRF spectra calculations, while for the linear absorption calculation we set the initial condition as described in subsection 3.2.4 .

The functional form of the spectral density function depends on the model for the environmental fluctuations. Here we apply the widely used overdamped Brownian oscillator model,[37] which corresponds to the Drude-Lorentz spectral density function:

$$C_n''(\omega) = \frac{2\Lambda_n \gamma_n \omega}{\gamma_n^2 + \omega^2}. \tag{3.3}$$

It is different from the spectral density function described in the previous chapter due to requirements of the HEOM approach used for benchmarking. The parameters related to discretization of the spectral density function were as follows: the number of modes $Q = 4000$ (2000 per site) the bandwidth $W = 3000\,\mathrm{cm}^{-1}$ and the minimum frequency $\omega_0 = 0.001\,\mathrm{cm}^{-1}$. The observables were averaged over 10000 stochastic realizations, which is the number sufficient for convergence at 300K temperature in the strong system-bath coupling case. For lower temperatures the results converge with less realizations.

To describe the interaction with the optical field we add a system-field interaction term to the Hamiltonian

$$\begin{aligned}\hat{H}_{\mathrm{F}} &= -\hat{d}\cdot\boldsymbol{E}(t)\\ &= -\sum_n \left(\boldsymbol{\mu}_n\cdot\boldsymbol{o}\right)\boldsymbol{E}(t)\left(\hat{a}_n^\dagger+\hat{a}_n\right).\end{aligned} \tag{3.4}$$

Here $\hat{d}$ is the dipole moment operator, $\boldsymbol{\mu}_n$ is the transition dipole vector for site n, $\boldsymbol{o}$ is the polarization vector of the optical field and $\boldsymbol{E}(t)$ is the time-dependent electric field amplitude. We selected the site transition dipole moment vectors as having an identical magnitude. In absorption calculations we selected them to be parallel to each other: $\boldsymbol{\mu}_1 = (1,0,0)$, $\boldsymbol{\mu}_2 = (1,0,0)$, and in auxiliary TRF calculations they were set perpendicular to each other: $\boldsymbol{\mu}_1 = (1,0,0)$, $\boldsymbol{\mu}_2 = (0,1,0)$ for demonstration purposes: setting the dipoles perpendicular allows for better visual identification of energy transfer in the corresponding spectra.

3.2.3 Hierarchical equations of motion approach

In this subsection we give a short overview of the hierarchical equations of motion (HEOM) approach used for benchmarking. HEOM approach is a non-perturbative method to calculate the electronic excitation dynamics and the optical response functions.[7,86,87] The main idea of this method is to replace the reduced density operator $\hat{\rho}$ by a set of auxiliary density operators (ADOs) $\hat{\rho}_{\mathbf{n}}$ (here $\mathbf{n} = \{n_{10},\ldots,n_{1K};\ldots;n_{N0}\ldots,n_{NK}\}$ is a set of indices) and expand the bath correlation function into exponential functions[18,60] as

$$C_n(t) = \sum_{k=0}^{K} c_{nk}\mathrm{e}^{-\gamma_{nk}t} + \Delta_{nK}\delta(t). \tag{3.5}$$

The ADO with indices all equal to zero $(\mathbf{0})$ represents the reduced density operator. The HEOM then read as:[60]

$$\begin{aligned}\frac{\mathrm{d}}{\mathrm{d}t}\hat{\rho}_{\mathbf{n}} = &-\mathrm{i}\left[\hat{H}_{\mathrm{el}}, \hat{\rho}_{\mathbf{n}}\right] - \sum_{m}\sum_{k}^{K}\gamma_{mk}n_{mk}\hat{\rho}_{\mathbf{n}} \\ &- \sum_{m}\frac{\Delta_{mK}}{2}\left[|m\rangle\langle m|, [|m\rangle\langle m|, \hat{\rho}_{\mathbf{n}}]\right] \\ &+ \mathrm{i}\sum_{m}\sum_{k}^{K} n_{mk}\left(c_{mk}|m\rangle\langle m|\hat{\rho}_{\mathbf{n}^{-}_{mk}} - c^{*}_{mk}\hat{\rho}_{\mathbf{n}^{-}_{mk}}|m\rangle\langle m|\right) \\ &+ \mathrm{i}\sum_{m}\sum_{k}^{K}\left[|m\rangle\langle m|, \hat{\rho}_{\mathbf{n}^{+}_{mk}}\right]. \end{aligned} \tag{3.6}$$

Here

$$\mathbf{n}^{\pm}_{mk} = \{n_{10}, \ldots, n_{1K}; \ldots; n_{m0}, \ldots, n_{mk} \pm 1, \ldots, n_{mK}; \ldots; n_{N0}, \ldots, n_{NK}\}. \tag{3.7}$$

The coefficients Δ_{mK}, γ_{mk} and c_{mk} for the spectral density defined in Eq. 3.3 can be taken from, e. g.[18]

The tier of ADO is defined as $L = \sum_{m}^{N}\sum_{k}^{K} n_{mk}$. The hierarchy is then truncated in two dimensions - first, by limiting the number of exponential functions K in the expansion (Eq. (3.5)), and, second, by limiting the maximum tier L of ADOs included in calculations. In all our calculations both these parameters were chosen such that convergence was achieved.

3.2.4 Absorption spectra

For calculation of linear absorption spectra using the sTDVA approach we completely follow the methodology described in chapter 1.7. To set the initial conditions we have used the Ansatz $\mathrm{e}^{-\mathrm{i}\hat{H}t}\hat{\mu}|0\rangle = |\Psi_{D2}(t)\rangle$, with

$$\alpha_n(0) = (\boldsymbol{\mu}_n \cdot \boldsymbol{o}) \Big/ \sqrt{\sum_{m}(\boldsymbol{\mu}_m \cdot \boldsymbol{o})^2}. \tag{3.8}$$

Orientational averaging is performed by a Monte Carlo procedure: we generate randomly oriented electric field polarization vectors of unit magnitude $\boldsymbol{o}$, and thus obtain $(\boldsymbol{\mu}_m \cdot \boldsymbol{o})$. The averaging is then done at the same time as the ensemble averaging of realizations. The ensemble- and orientationally-averaged response function is then given by

$$R^{\mathrm{abs}}(t) = \left\langle R^{\mathrm{abs}}(t)^{(R)} \right\rangle_{R,\mathrm{or}}. \tag{3.9}$$

The calculation of the linear response function using the HEOM approach was described in ref.[11] Briefly, we start by taking $\hat{\rho}_{\mathbf{0}}(0) = |0\rangle\langle 0|$ and $\hat{\rho}_{\mathbf{n}\neq\mathbf{0}}(0) = 0$ as the initial condition. We multiply $\hat{\rho}_{\mathbf{n}}$ from the left by the polarization operator $\hat{\mu}$, which is equal to

$$\hat{\mu} = \sum_l \mu_l \left(|l\rangle\langle 0| + |0\rangle\langle l|\right). \tag{3.10}$$

We then obtain

$$\hat{\mu}\hat{\rho}_{\mathbf{n}}(0) = \sum_l \mu_l |l\rangle\langle 0|\hat{\rho}_{\mathbf{n}}(0), \tag{3.11}$$

using the fact that that $\hat{\rho}_{\mathbf{n}}(0)$ has nonzero elements only for the ground state. We introduce a shorthand notation for the product of site state projectors and the density operators as: $|a\rangle\langle b|\hat{\rho}_{\mathbf{n}}(\tau) = \hat{\rho}_{\mathbf{n}}(ab,\tau)$ and $\hat{\rho}_{\mathbf{n}}(\tau)|a\rangle\langle b| = \hat{\rho}_{\mathbf{n}}(\tau, ab)$. Using this notation the linear response function is expressed as

$$\begin{aligned} R^{\mathrm{abs}}(t) &= \sum_m \sum_l \langle (\boldsymbol{\mu}_m \cdot \boldsymbol{o})(\boldsymbol{\mu}_l \cdot \boldsymbol{o})\rangle_{\mathrm{or}} \rho^{\mathbf{0}}_{m0}(l0, 0; t) \\ &= \sum_m \sum_l \frac{1}{3}(\boldsymbol{\mu}_{\mathrm{m}} \cdot \boldsymbol{\mu}_{\mathrm{l}})\, \rho^{\mathbf{0}}_{m0}(l0, 0; t). \end{aligned} \tag{3.12}$$

The factor $\frac{1}{3}$ arises from the orientational averaging of the molecular system.[88] Note that only the reduced density operator and not the rest of ADOs contribute to the observable response function.

3.2.5 Time-resolved fluorescence spectra

The time-resolved fluorescence (TRF) experiment is characterized by four interactions between the system and the optical field, with the first two being with the incoming laser pulse creating an optical excitation and the later two being the vacuum fluctuations leading to spontaneous emission.[12,37,38,89] From the theoretical point of view, the TRF spectrum is obtained by a convolution of the optical response function of the system with the response function of the instrument. Under the assumption of instantaneous excitation, all the information about the system available from the TRF experiment is contained in the system response function $R^{\mathrm{TRF}}(t,\tau)$. Since the convolution hides some information, we will follow ref.[38] and calculate auxiliary TRF spectra defined as :

$$F(\omega,\tau) = \mathrm{Re}\int_0^\infty \mathrm{d}t\, \mathrm{e}^{\mathrm{i}\omega t} R^{\mathrm{TRF}}(t,\tau). \tag{3.13}$$

In addition, in this case we simplify the model even further by factorizing out the first two interactions corresponding to the excitation process completely by setting

an explicit initial excited state for the system. The optical response function in the density operator formalism is then given as

$$R^{\mathrm{TRF}}(t,\tau) = \Big\langle \mathrm{Tr}\left\{\hat{d}\exp\left(-\mathrm{i}\hat{H}t\right)\exp\left(-\mathrm{i}\hat{H}\tau\right)\hat{\rho}(0)\hat{\rho}^{\mathrm{ph}}(0) \cdot \exp\left(\mathrm{i}\hat{H}\tau\right)\hat{d}\exp\left(\mathrm{i}\hat{H}t\right)\right\}\Big\rangle_{\mathrm{or}}. \tag{3.14}$$

For sTDVA the response function is calculated exactly as in chapter 1.7. In this particular case the single-realization optical response function is given in terms of the variational parameters as

$$\begin{aligned} R^{\mathrm{TRF}}(t,\tau)^{(R)} &= \Big\langle \langle\Psi_{D2}(\tau)|\hat{d}\mathrm{e}^{\mathrm{i}H_B t}\hat{d}|\Psi_{D2}(t)\rangle\Big\rangle_{\mathrm{or}} \\ &= \sum_{m,n}\frac{1}{3}\left(\boldsymbol{\mu}_m\cdot\boldsymbol{\mu}_n\right)\alpha_m^*(\tau)\alpha_n(t) \\ &\quad\cdot\exp\sum_q\Big(\mathrm{e}^{\mathrm{i}\omega_q(t-\tau)}\lambda_q^*(\tau)\lambda_q(t) \\ &\quad -\frac{1}{2}\left[|\lambda_q(\tau)|^2+|\lambda_q(t)|^2\right]\Big). \end{aligned} \tag{3.15}$$

The ensemble averaging is then performed numerically in the same way as for the linear response.

Calculation of the nonlinear response functions using the HEOM approach formally requires an introduction of somewhat abstract concepts as the HEOM space,[60] which are beyond the scope of this thesis. Nevertheless, the required steps can be explained rather simply as follows, having in mind Eq. (3.14). First, we propagate the HEOM for time τ using the initial condition $\hat{\rho}_{\mathbf{0}}(0) = \hat{\rho}(0)$ and $\hat{\rho}_{\mathbf{n}\neq\mathbf{0}}(0) = 0$ to obtain $\hat{\rho}_{\mathbf{n}}(\tau)$. Here $\hat{\rho}(0)$ is the chosen initial electronic density operator of the primary excited state. Then we multiply it from the right by $\hat{\mu}$ and obtain $\hat{\rho}_{\mathbf{n}}(\tau)\hat{\mu} = \sum_l \mu_l\hat{\rho}_{\mathbf{n}}(\tau)|l\rangle\langle 0| = \sum_l \mu_l\hat{\rho}_{\mathbf{n}}(\tau,l0)$. Next we propagate the HEOM for time t using the initial condition $\hat{\rho}_{\mathbf{n}}(\tau,l0)$, and obtain $\hat{\rho}_{\mathbf{n}}(\tau,l0;t)$. Using the matrix element $\rho_{0m}^{\mathbf{n}}(\tau,l0;t) = \langle 0|\hat{\rho}_{\mathbf{n}}(\tau,l0;t)|m\rangle$ we can write the response function as

$$\begin{aligned} R(t,\tau) &= \sum_l\sum_m\langle\left(\boldsymbol{\mu}_m\cdot\boldsymbol{o}\right)\left(\boldsymbol{\mu}_l\cdot\boldsymbol{o}\right)\rangle_{\mathrm{or}}\rho_{0m}^{\mathbf{0}}(\tau,l0;t) \\ &= \sum_l\sum_m\frac{1}{3}\left(\boldsymbol{\mu}_m\cdot\boldsymbol{\mu}_l\right)\rho_{0m}^{\mathbf{0}}(\tau,l0;t). \end{aligned} \tag{3.16}$$

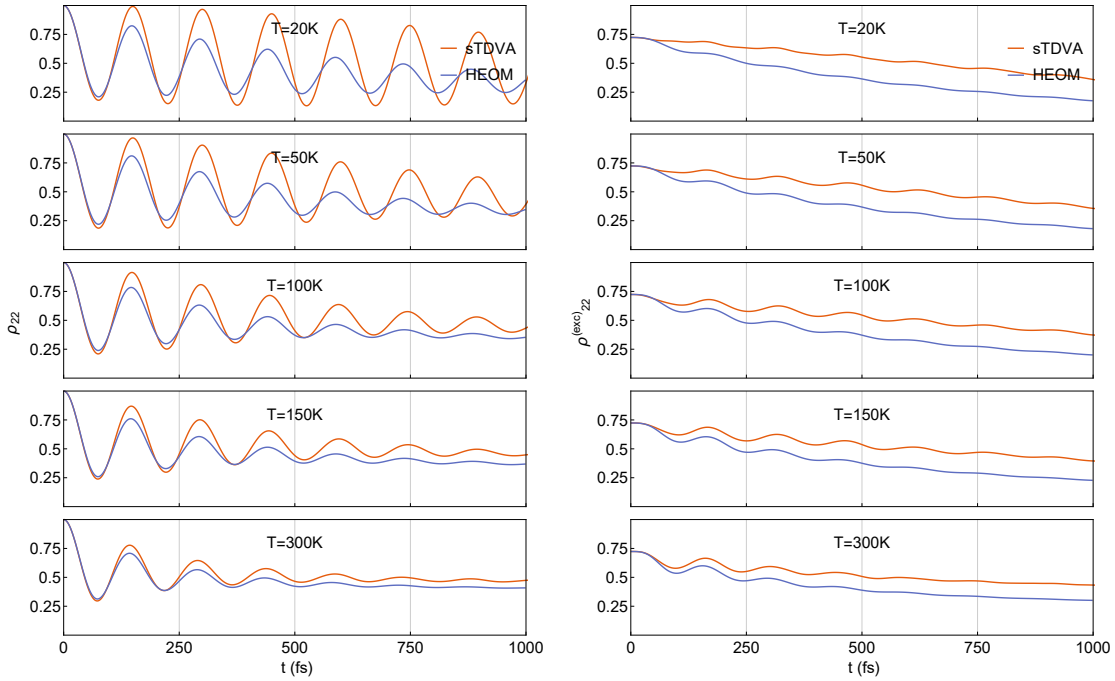

(a) Site basis **(b)** Excitonic basis

Fig. 3.1. Comparison of population dynamics of a heterodimer system in weak system-bath coupling regime, calculated with sTDVA and HEOM approaches

3.2.6 Results

First we show the population evolutions obtained with the sTDVA and HEOM approaches for five different temperatures. The evolutions in site and exciton bases are shown in Figs. 3.1, 3.2, and 3.3. Every figure shows the population of either the higher energy site or the higher energy exciton, and the populations of the lower energy site/exciton follow from the condition $\sum_n \rho_{nn} = 1$.

Let us consider the weak system-bath coupling regime. For early times ($t \lesssim 50\,\mathrm{fs}$) the populations in both bases match exactly between the sTDVA and the HEOM methods (see Fig. 3.1a), which also applies to other regimes. At later times, the HEOM approach displays a faster decay of coherences (the off-diagonal elements of the reduced density operator) and faster population transfer (between the diagonal elements of the density operator). The qualitative behavior of both approaches is similar, with the frequency of the coherent oscillations coinciding. The agreement is better at higher temperatures, with the sTDVA approach showing similar timescales for the coherence decay, but the population transfer rate is still somewhat lower than the one obtained with HEOM.

Now let us turn to the weak resonant coupling regime. Considering first the site basis (Fig. 3.2a), the agreement between the sTDVA and HEOM populations at low temperatures is worse than in the weak system-bath coupling regime. Although for early times the evolutions still coincide identically, the sTDVA approach predicts

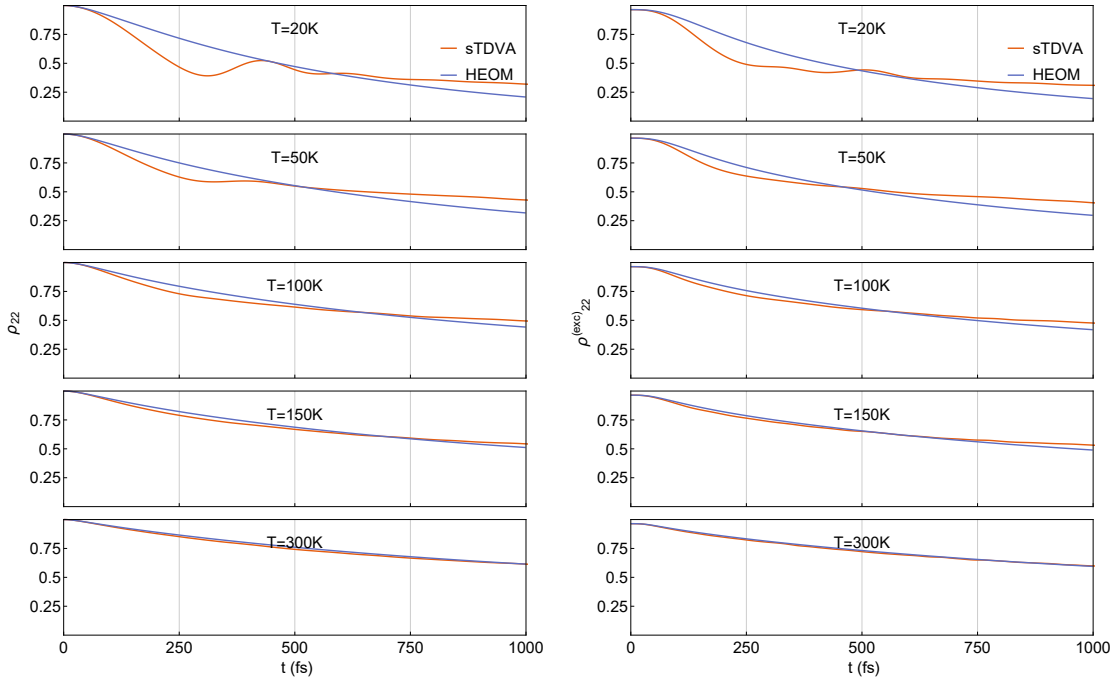

(a) Site basis **(b)** Excitonic basis

Fig. 3.2. Comparison of population dynamics of a heterodimer system in weak resonant coupling regime, calculated with sTDVA and HEOM approaches

faster energy transfer during the first 500 fs of the evolution and slower energy transfer on later times, with the kinetics being non-exponential. At higher temperatures the results obtained with both approaches coincide almost exactly. Since the resonant coupling is weak, results in the excitonic basis (Fig. 3.2b) are not much different from the site basis.

In the case of the intermediate regime (Fig. 3.3a and Fig. 3.3b) a slower coherence decay is obtained by the sTDVA at low temperatures, though the population transfer rate is similar. At higher temperatures the timescales of coherence decay start to coincide, but the energy transfer rate is slightly lower in the sTDVA case, though the difference in all cases is less pronounced than in the weak system-bath coupling regime. The asymptotic population is slightly higher in the sTDVA case at higher temperatures. Overall, the agreement between the two approaches is reasonable.

The calculated absorption spectra corresponding to the intermediate regime are presented in Fig. 3.4. The lineshapes obtained with the two approaches are qualitatively very similar, displaying perfect match at higher temperatures. The sTDVA approach generally predicts a slightly lower intensity of the lower energy peak at all temperatures. The corresponding absorption spectra for the two other regimes (not shown) display a similar agreement. The population dynamics match exactly for the first 50 fs, and this is approximately the decay timescale of the linear response

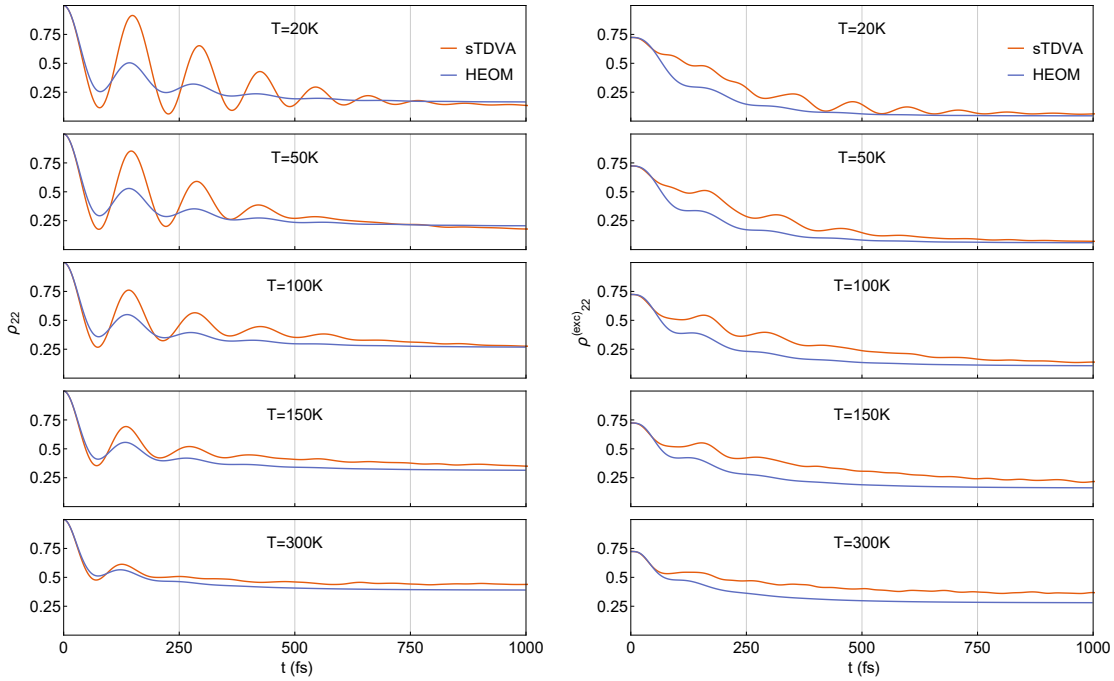

(a) Site basis **(b)** Excitonic basis

Fig. 3.3. Comparison of population dynamics of a heterodimer system in intermediatecoupling regime, calculated with sTDVA and HEOM approaches

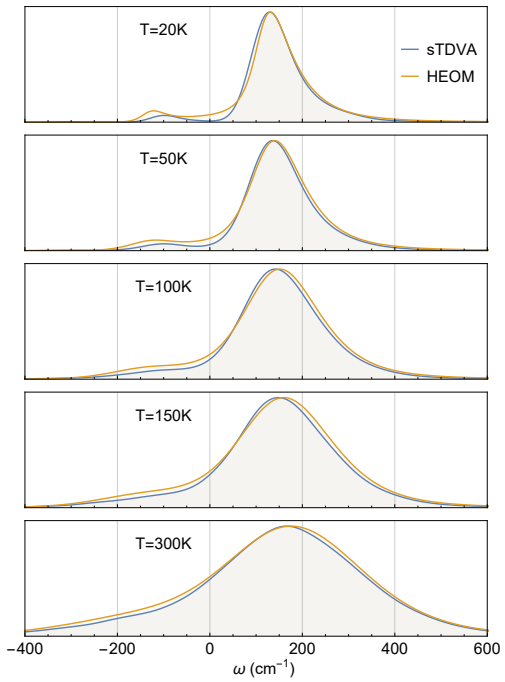

Fig. 3.4. Linear absorption spectra for intermediate coupling regime.

function, which is relevant for absorption spectra. The auxiliary time-resolved fluorescence spectra at 150 K demonstrate poor agreement between the two methods in the weak system bath coupling case (see Fig. 3.5a). Though the agreement between the spectral lineshapes is good, the effect of the slower energy transfer is very noticeable in this case as the time evolution of peak intensities follows the populations of the excitonic states. Indeed, the peak intensities given by the sTDVA at 1000 fs

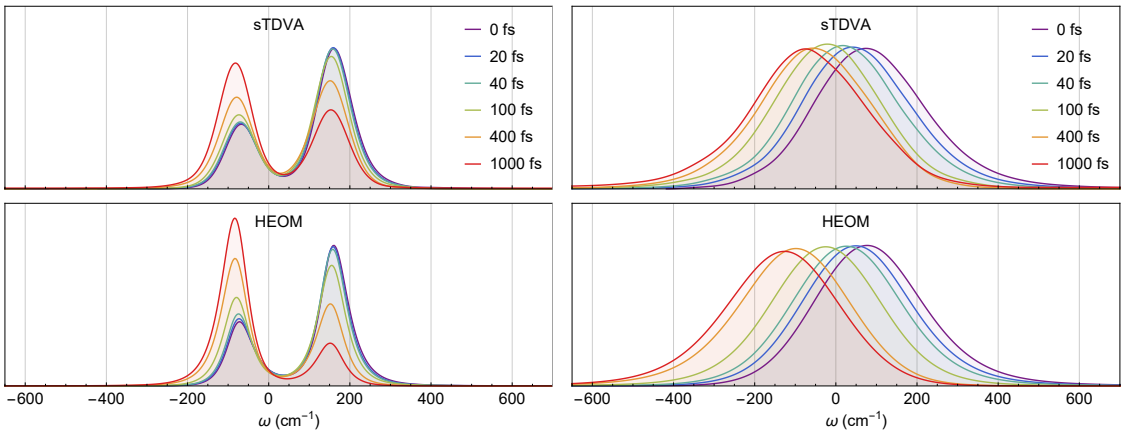

(a) Weak system-bath coupling regime

(b) Weak resonant coupling regime

Fig. 3.5. Auxiliary time-resolved fluorescence spectra at $T = 150\mathrm{K}$.

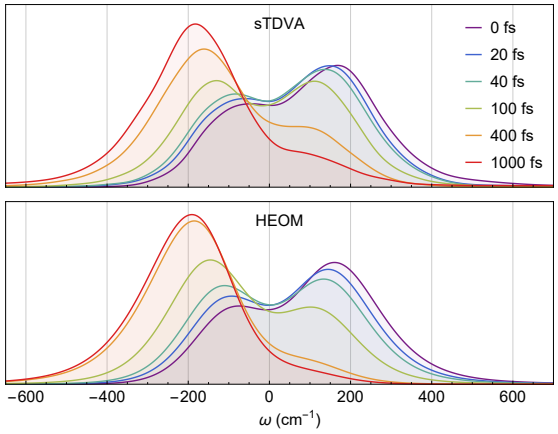

Fig. 3.6. Auxiliary time-resolved fluorescence spectrum at $T = 150\mathrm{K}$ in intermediate regime

are similar to the intensities given by the HEOM at 400 fs. On the other hand, in the weak resonant coupling regime (see Fig. 3.5b) the spectra coincide nearly identically, with the only difference being slightly slower bath reorganization. In the intermediate regime (see the Fig. 3.6) the difference between the two methods is minor, displaying slightly slower transfer replicating the population dynamics. The redshifts and spectral broadening coincide using both approaches.

3.2.7 Summary of the accuracy study

From the three different sets of parameters that were examined, we conclude that the sTDVA gives better agreement with the HEOM when the system-bath coupling is large and the resonant coupling is small. These results are in a qualitative agreement with the results corresponding to the zero temperature case.[85] The error in populations from sTDVA comes from underestimating the rate of energy transfer. Additionally, we have found that the agreement between the two methods becomes better for higher temperatures. This is somewhat surprising, as the D_2 Ansatz assumes that the phonon modes are described as coherent states, which are an exact representation of a harmonic oscillator in the ground electronic state. The wave-

functions of low energy oscillator states, that are important at low temperatures, have high overlap with the ground state wavefunction, and thus should be represented accurately. On the other hand, at lower temperatures the low frequency part of the spectral density becomes critical, and, as discussed below, the specific form of the spectral density might be responsible for the differences between the two methods.

Our results show that the sTDVA gives considerably longer lasting oscillations of site populations in the weak system-bath coupling regime. In principle, they reflect the Rabi oscillations, arising because the initial condition for propagation does not correspond to an eigenstate of the system Hamiltonian. It is noteworthy that these longer oscillations are less evident in the excitonic basis. This means that the errors of site coherences and populations add up in such a way that excitonic populations given by the sTDVA are closer to the ones given by the HEOM.

The spectral density is chosen according to the demands of the HEOM calculations (Eq. (3.3)). Nevertheless, this spectral density has several issues, which are as follows. First, the relatively slow decay for larger frequencies implies that a relatively large number of modes has to be included when using the sTDVA approach, which slows down the calculations. Moreover, the behavior of this spectral density for low frequencies is proportional to the frequency ω, which means that the total Huang-Rhys factor defined as $\sum_q g_q^2 = \int_0^\infty \mathrm{d}\omega\, C''(\omega)/\pi\omega^2$ diverges for this spectral density. Therefore, the minimum frequency ω_0 cannot be set to an arbitrary low value and the spacing between the mode frequencies cannot be made too small, to avoid numerical instabilities. In case of the continuous spectral density, the minimum frequency should be arbitrarily small. As discussed in ref.,[90] two spectral densities that differ minimally in the small frequency range may nevertheless give somewhat different results, especially at lower temperature. This might explain the worse agreement between the sTDVA and HEOM at lower temperatures.

We should also emphasize that the equations of motion for the sTDVA with the D_2 Ansatz preserve the norm of the wavefunction. Therefore, physical solutions (populations are nonnegative and sum up to 1 in all bases) at all times are guaranteed. This is a considerable advantage of this approach. Conversely, the evolutions for *all* considered parameter regimes obtained using the second order quantum master equation (usually termed as the Redfield equation) give negative populations at lower temperatures (not shown), even when the system-bath coupling is small. This is because the Redfield approach relies not only on the weak system-bath coupling, but also on the Markov approximation, which requires a short bath correlation time. The decay timescale of the bath correlations chosen in this work ($\gamma^{-1} = 100\,\mathrm{fs}$) is too slow for the Redfield equation to be accurate. In cases like these, the secular approximation is often employed, but then the relation between excitonic coherences

and populations is lost. In contrast, in the sTDVA the bath degrees of freedom are included explicitly, and this automatically accounts for memory effects.

From both calculations of the absorption and auxiliary TRF spectra, it follows that the sTDVA accurately reproduces the spectral lineshapes for all considered parameter regimes. As demonstrated in our recent publication,[15] it is most important to correctly capture the initial part of the relevant response function. Since the sTDVA accurately reproduces the initial part of the population dynamics, this means that the initial part of the response function should also be reproduced well. We also note that the response functions calculated in terms of the sTDVA include the coherence transfer effects, which is somewhat difficult to do in approaches based on the cumulant expansion approach.[91]

The calculation of nonlinear response functions is required for simulations of nonlinear spectroscopy experiments. Theoretically, it is a very complicated problem, as it requires to keep track of the correlations between distinct time intervals.[83,84] Approaches that use a reduced description by tracing out the bath degrees of freedom are difficult to apply for this problem. As the sTDVA allows to explicitly account for the bath degrees of freedom, it holds a great promise for nonlinear response function calculations. Our calculated auxiliary TRF spectra show that the spectral lineshapes are reproduced accurately with this approach, and the difference from the exact results are only due to somewhat slower energy transfer. Therefore, the sTDVA should be considered as a suitable method for simulations of other nonlinear spectroscopy experiments, such as two-dimensional electronic spectroscopy, especially in the intermediate coupling regime.

The accuracy of the TDVA with Davydov Ansatze as trial wavefunctions was previously examined for the zero temperature case.[85] To the best of our knowledge, our work is the first systematic exploration of the sTDVA with a finite temperature taken into consideration. While finite temperature was included in calculations of refs.,[92–94] that was done via a secondary bath, that was not treated on equal footing with the primary bath. The sTDVA, introduced in ref.[2] and analyzed in detail here, does not require any secondary bath and allows to treat both high and low frequency phonons on the same level, explicitly tracking the degrees of freedom. We must highlight another key difference between earlier contributions and the present work. In refs.[35,85,92–94] it was assumed that the phonons couple to each site *non-locally.* Therefore, the site energy fluctuations were totally correlated, and no *incoherent* energy transfer was possible. Conversely, the model presented here assumes local coupling between phonons and sites. This is more in line with, e. g., photosynthetic complexes, as it was demonstrated that the site energy fluctuation correlations can often be neglected in this case.[95,96]

The Davydov Ansatze are often used to describe polaron dynamics, thus we

would like to make a few comments on the relation of the present approach with that of small polaron transformation. First, we must note that the polaron transformation by itself corresponds only to the transformation of the Hamiltonian,[97] thus it reflects static properties, not dynamical ones, and as such it cannot be easily compared to the sTDVA with the Davydov Ansatze. The variational procedure with Anzatze similar to the D_2 could be used for determination of polaron ground state energy and other properties,[50] but again this reflects static properties. Nonetheless, the polaron transformation can be combined with perturbation theory to yield a polaronic quantum master equation.[80] Then one gets an equation for the reduced density operator of an open quantum system, and this differs in principle with the wavefunction (of a closed system) approach presented here.

The sTDVA, as it is constructed, can work with any trial wavefunction. In principle, the more complicated the wavefunction with more degrees of freedom, the less deviation from the exact results should be obtained. Even though here we use the Davydov D_2 Ansatz, other Ansatze, such as the more complicated Davydov D_1 Ansatz, are possible as well. The only requirement is that the chosen Ansatz must allow for a consistent procedure of sampling the initial conditions, i.e. it must be possible to find a generalized probability distribution for the thermal state in the basis constructed with the Ansatz functions. It was recently shown that for a molecular crystal model, the usage of the D_2 Ansatz with higher multiplicity greatly increased the accuracy of the solution in the zero temperature case.[94] The multi-D_1 Ansatz applied to the traditional spin-boson model was shown to improve numerical accuracy by a large factor,[98] and a generalized coherent state Ansatz provides similarly accurate results in the zero-temperature case for a model excitonic polaron system.[99]

Although the sTDVA approach requires averaging over stochastic realizations, which massively increases the computation time in comparison to the zero-temperature case, with the D_2 Ansatz, the scaling of the computational effort is quadratic in the number of the system sites and linear in the number of considered modes, bandwidth and propagation time. This makes it completely feasible to apply for large molecular complexes, as shown in ref.[2] Since the averaging is performed over completely independent realizations, the approach takes full advantage of parallel computing techniques and is very suitable for running on supercomputers.

3.3 Variational study of the LH2 aggregate

3.3.1 Introduction

One of the basic light harvesting agents in studies of photosynthesis is the LH2, the peripheral light harvesting complex of purple bacteria.[100,101] The complex

demonstrates outstandingly high circular symmetry and the atomic structure obtained by X-ray crystallography[102] is known for two bacteria species: Rhodospirillum molischianum[103] and Rhodopseudomonas acidophila[73,104] (now Rhodoblastus acidophilus[105]). The latter complex consists of 27 bacteriochlorophyll (BChl) *a* pigments bound to a protein matrix and arranged in two concentric C_9-symmetry rings: one having 9 pigments and the other 18. The complex has two prominent absorption bands at 800nm and 850nm at room temperature. The rings are commonly associated with these absorption peaks and named correspondingly to their absorption maxima (in nanometers) as B800 and B850. The 9 Bchl *a* pigments that compose the B800 ring are weakly interacting, and the B850 ring is grouped into 9 strongly interacting heterodimeric pairs of Bchl *a* pigments.[49,106–111] The lowest-energy optical transition of isolated Bchl *a* pigments shows a peak approximately at 770nm (dependent on the solvent), and the large shift in transition frequency of LH2 is caused by the excitonic splitting and the reorganization of the local environment. The Frenkel exciton model has been successful to explain absorption spectroscopy[101,112,113] as well as ultrafast dephasing in two dimensional coherent spectroscopy experiments[114–117] showing the relevance of a k-band electronic structure.[72,77,118–120] However, the temperature dependencies of the spectra require to include dichotomous corrections,[121,122] or more complex anharmonic phonon properties.[117] Simulations of the experimental emission spectra of LH2 suggested that the exciton model is not enough to explain the broadening of the lowest exciton state and the temperature dependence of the fluorescence lifetime. Exciton self-trapping in the B850 ring has been suggested to explain the effects.[49,123,124] The same concept of exciton self-trapping has been used to explain the experimental data on site-selective spectra[46] and single-complex fluorescence excitation and emission spectra in various pigment-protein complexes.[125]

However, the polaronic effects are not trivial to confirm at ambient temperature because superpositions of states are in play. It has been shown in ref.[12] that the off-diagonal elements of the density matrix not decaying to zero asymptotically corresponds to a non-optimal choice of representation (quantum mechanical basis set). According to statistical physics the thermal equilibrium density operator in the global eigenstate basis is necessarily diagonal, i. e. the off-diagonal elements of the density matrix are zero. The search for polaronic effects then corresponds to the search of the global eigenbasis (also known as the pointer basis set of the system undergoing decoherence)[126,127] and comparing it to the excitonic basis. The excitonic polaron picture has been demonstrated to be relevant in the case of an overdamped phonon bath at an arbitrary temperature in a model system.[1,12]

In the following sections we describe excitation dynamics and trapping in the strongly coupled B850 ring of the LH2 aggregate utilizing the sTDVA approach.

The exciton wave-like propagation, the self-trapping and delocalization effects in this ring are obtained and characterized via simulations of excitation relaxation dynamics together with linear absorption / fluorescence spectra.

3.3.2 Model parameters

We choose to investigate separately the absorption spectrum of the full LH2 system, and then focus on the excitation dynamics and TRF spectra of the B850 ring. The site energy and coupling matrix is used as it is described in ref.[113,117] Additionally we average energies of identical pigments: B800, α-B850, and β-B850; where α-B850 and β-B850 refer to the pigments bound to the α (outer) and β (inner) transmembrane proteins of the LH2 complex, respectively. In the model the site energies of the α-B850 pigments are about $310\,\mathrm{cm}^{-1}$ higher than those of β-B850. The site-dependent conformational disorder δ_n was generated according to a Gaussian distribution with standard deviations $\sigma_{B800} = 60\,\mathrm{cm}^{-1}, \sigma_{B850} = 220\,\mathrm{cm}^{-1}$, where σ_{B800} is the value for every pigment belonging to the B800 ring, and σ_{B850} for every pigment belonging to the B850 ring.

The form for the spectral density function was chosen as a sum of Ohmic and super-Ohmic spectral densities to correctly account for the low-frequency behaviour,[128] which is the most relevant for intra-ring energy transfer. The parameters are assumed from comparison to experimental absorption lineshape studies:[47]

$$C_n''(\omega) = \sum_{i=1}^{2} \omega^{i+1} e^{-\frac{\omega}{\omega_{c,i}}} \frac{\alpha_i}{\omega_{c,i}^i\,(i+1)!}. \tag{3.17}$$

Here $\omega_{c,1} = 50\,\mathrm{cm}^{-1}$, $\omega_{c,2} = 15\,\mathrm{cm}^{-1}$, $\alpha_1 = 1$, $\alpha_2 = 2$. $\Lambda_{B800} = 45\,\mathrm{cm}^{-1}$, $\Lambda_{B850} = 135\,\mathrm{cm}^{-1}$ denote the reorganization energies (Eqn. (1.22)) of pigments belonging to the B800 and B850 rings, respectively. We must note that the chosen form of spectral density function with the specified parameters does not account for the inter-ring energy transfer processes, since the spectral density approaches zero at frequencies that correspond to the energy gaps between the B800 and the B850 excitons. Additional high frequency modes may be necessary for the inter-ring relaxation.[129]

For simulations, the vibrational modes of each site are defined by uniformly discretizing the spectral density function with a frequency step Δ_ω in the frequency range $(0, W]$, where $W = \Delta_\omega Q_{\mathrm{site}}$ is the bandwidth. W should be chosen to be larger than all relevant vibrational frequencies of the system (essentially it should match the frequency of the highest vibrational mode which is coupled to the electronic states strongly enough to influence its dynamics), while the minimum frequency interval Δ_ω defines a recurrence timescale equal to $2\pi/\Delta_\omega$. In general

the latter should be larger than an arbitrary timescale of interest in the system dynamics. The phonon bandwidth (cutoff parameter W) was set to $425\,\mathrm{cm}^{-1}$, while $Q_{\mathrm{site}} = 200$ and consequently $\Delta_\omega = 2.125\,\mathrm{cm}^{-1}$. The coupling strengths are assigned using Eqn. (1.21): $g_{qn}^2 \propto C_n''(\omega_q)/\omega_q^2$. The sign of g_{qn} remains arbitrary, so we keep it positive, while the values are normalized using the definition of the reorganization energy (Eqn. (1.22)). Every simulation is averaged over 25000 realizations of static disorder and initial conditions for the vibrational states.

3.3.3 Population dynamics and spectra

The set of parameters for the electronic block of the Hamiltonian and the transition dipole moments is directly taken from refs.,[113,117] and here we did not perform any additional fitting of the model parameters to experimental spectra. Thus, the direct comparison between the simulation results can be performed. We first calculate the linear polarization and the corresponding absorption spectrum of the full LH2 complex. Using the Eqn. (1.94), we calculate the dynamics of the system and construct the time-domain optical response function for the ensemble. It decays rapidly on a timescale of $\sim$200 fs, so only the initial femtosecond dephasing and energy transfer processes contribute to the absorption spectrum of the system, with later times being relevant only to other spectral signals (such as fluorescence). The absorption spectrum at $T = 100$ K (Fig. 3.7) reveals the expected double-peak structure with peaks at $\sim$11600 cm^{-1} and $\sim$12500 cm^{-1} (see ref.[111,113,117,130]). The lineshapes and the peak heights calculated using the present variational approach closely match the previous simulations (these were fitted to experiment), which demonstrates that both the Redfield or the present variational simulation approaches do describe the complexity of the excitation dynamics relevant to the absorption process. Consequently, the set of parameters is sufficiently accurate to describe the absorption process.

The electronic excitation causes energy relaxation within the aggregate through both electronic and vibrational degrees of freedom. In the following we proceed to simulate the dynamics in the B850 ring and do not consider the B800. The B850 ring is relevant for the fluorescence process since only B850 is emitting at long times. Additionally, the excitation dynamics in B850 fall into a regime where excitonic interaction as well as static and dynamic disorder are of comparable magnitudes. Thus, the excitation dynamics is expected to involve complex polaronic effects.

The population dynamics of the B850 ring, shown in Fig. 3.8, demonstrate a number of expected phenomena in this kind of model, namely energy redistribution among the dimeric subunits of the ring consistent with the kinetic relaxation scheme and decaying coherent oscillations which can be observed throughout the first 100

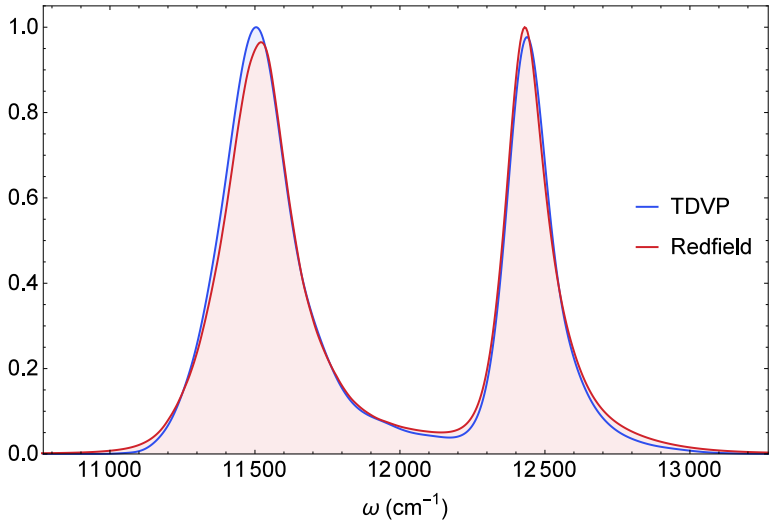

Fig. 3.7. Absorption spectrum of the full LH2 system at $T = 100$ K, calculated with sTDVA approach and with Redfield approach.[117]

fs of evolution.

At all temperatures the duration of the coherent oscillations stays roughly the same, which implies that the dephasing process is dominated by the static disorder instead of the thermal effects. To further reinforce the statement we simulate the dynamics at 100K temperature without the static conformational disorder (Fig. 3.9). As can be seen, in this case, the coherent oscillations persist up until 500 fs implying that the coherent processes last much longer in a single B850 ring vs. the disordered ensemble. Additionally notice that the final populations weakly depend on the temperature and on the static disorder. Hence, they must be determined by the energy splitting between various sites and by the intermolecular couplings.

Even though the electronic site populations become quasistationary after 100 fs (with static disorder) or 500 fs (without static disorder), the relaxation process continues due to the evolution of the phase relationships. This is demonstrated by plotting the populations in the excitonic picture (Fig. 3.10). For the symmetric circular aggregate the lowest energy excitonic state is denoted by quasimomentum $k = 0$, while next two excitonic states are degenerate with $k = \pm 1$. We recover this result when static disorder is not included. From Fig. 3.10 follows that the evolution towards a thermally equilibrated state continues to 2 ps, with the excitonic populations approaching a Boltzmann distribution. For comparison, at $T = 100$ K, $k_B T \approx 70$ cm^{-1} and the energy gap between the apparent $k = 0$ and $k = \pm 1$ states is equal to $\Delta_{k=0,k=\pm 1} = 108$ cm^{-1}. With Boltzmann distribution, $\exp(\frac{-\Delta_{k=0,k=\pm 1}}{k_B T}) \approx 0.21$ which is consistent with the observed asymptotic distributions of the excitonic populations and the excitonic picture (with the second highest excited state populations having approximately the value 0.2). The inclusion of static disorder lifts the degeneracy between $k = +1$ and $k = -1$ states, also slightly slowing down the relaxation

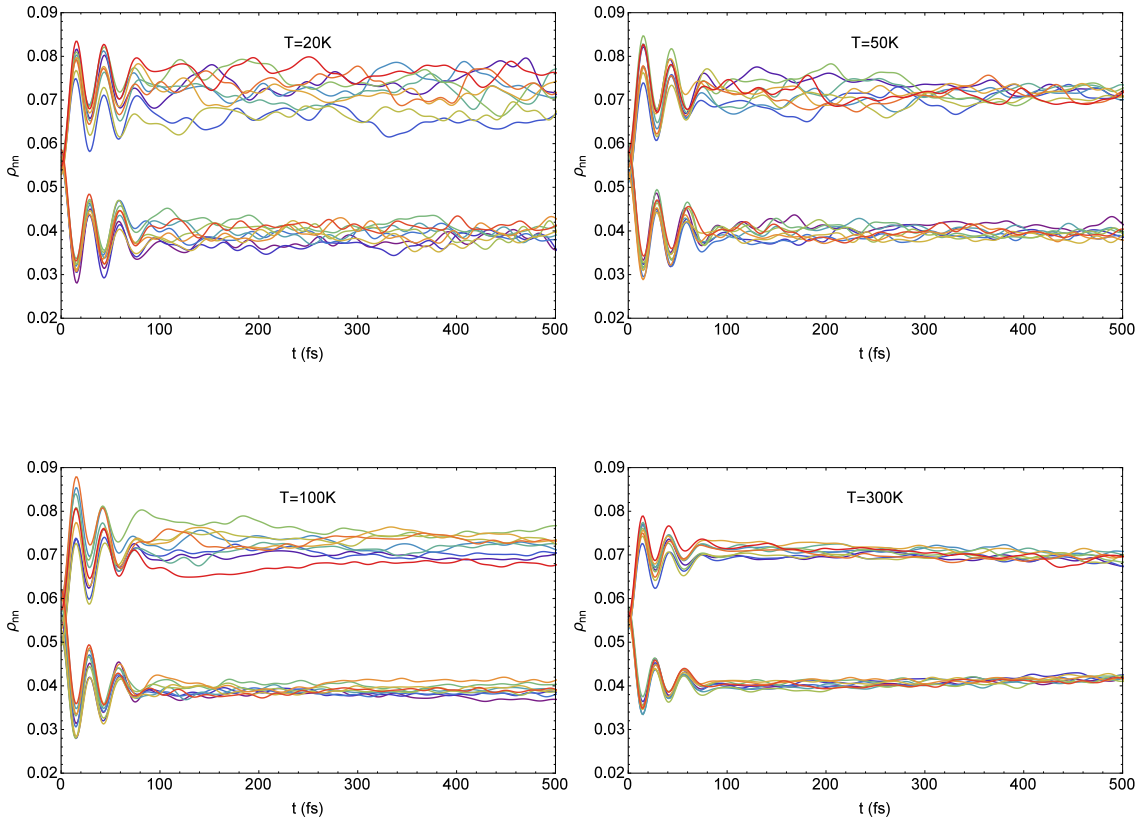

Fig. 3.8. Time dependences of site populations of B850 ring at various temperature, averaged over static disorder and thermal fluctuations. Different lines represent excitation populations at various sites, $|\alpha_n(t)|^2$ (18 lines totally).

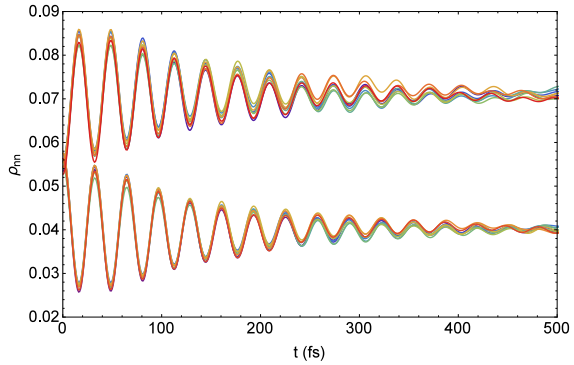

Fig. 3.9. Time dependences of site populations of B850 ring at 100 K temperature, averaged over thermal fluctuations without static disorder. Different lines represent excitation populations at various sites, $|\alpha_n(t)|^2$ (18 lines totally).

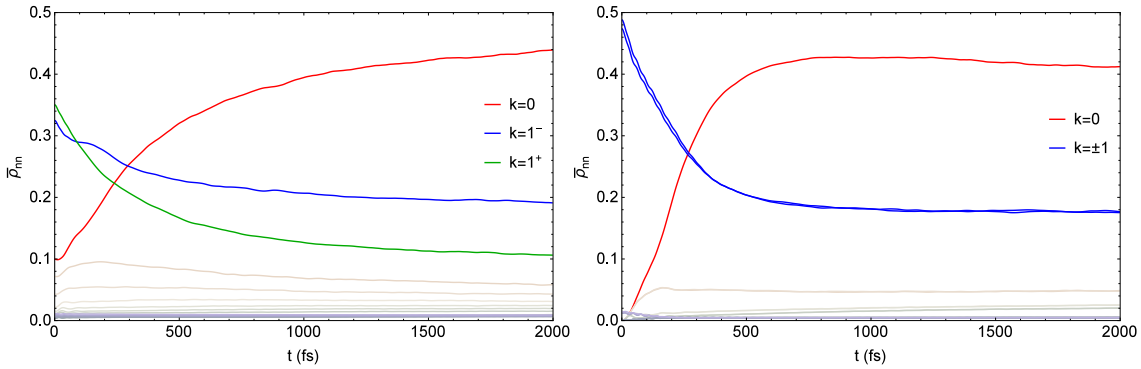

(a) With static disorder

(b) Without static disorder

Fig. 3.10. Time dependences of excitonic populations as a function of time at $T = 100$ K. We specifically mark the three lowest energy states (labeled by their quasimomentum k in order of increasing energy), the rest of the lines correspond to higher energy states.

process. Higher energy degenerate states $k = \pm 2, 3 \ldots$ are similarly split. With the degeneracy lifted we denote the lower and higher energy states correspondingly as $k = 1^-, 2^-, \ldots$ for the lower energy states and $k = 1^+, 2^+, \ldots$ for the higher energy states. Note that without static disorder we observe a slow redistribution of populations in the interval from 1 to 2 ps when the population of the lowest energy excitonic state slightly decreases. This effect implies slow reorganization of excitonic energies which hints on the transition to polaronic states.

Since the polaronic effects seem to appear at a $\sim$1 ps timescale, auxiliary time-resolved fluorescence (TRF) spectra[38] allow us to probe the spectral relaxation dynamics of the system including the complex interplay between the electronic and the vibrational degrees of freedom in these timescales. The results at four values of temperature are presented in Fig. 3.11. We normalize each of the lines to the maximum of the spectrum at $t = 0$.

Some of the features already evident from the site/exciton populations can be seen in the spectra. First, the spectral line at low (20, 50 K) temperatures show fine structure of excitonic bands. At the high temperature of 300 K the homogeneous broadening becomes larger and the excitonic bands become hidden. Second, the decay time of the absolute intensity of the spectrum coincides with the decay of coherent effects (Fig. 3.8), and is attributed first and foremost to the electronic coherence decay process. The second factor playing a role from 500 fs to 1 ps is the relaxation to the $k = 0$ state carrying a relatively low dipole strength. This can be clearly seen in the TRF spectra at lower temperatures, where the peak height decays rapidly to a value of about 0.6 during the initial 50 fs, and then the relaxation to the $k = 0$ state located at $\sim$11400 cm^{-1} redshifts the peak on a slower time scale.

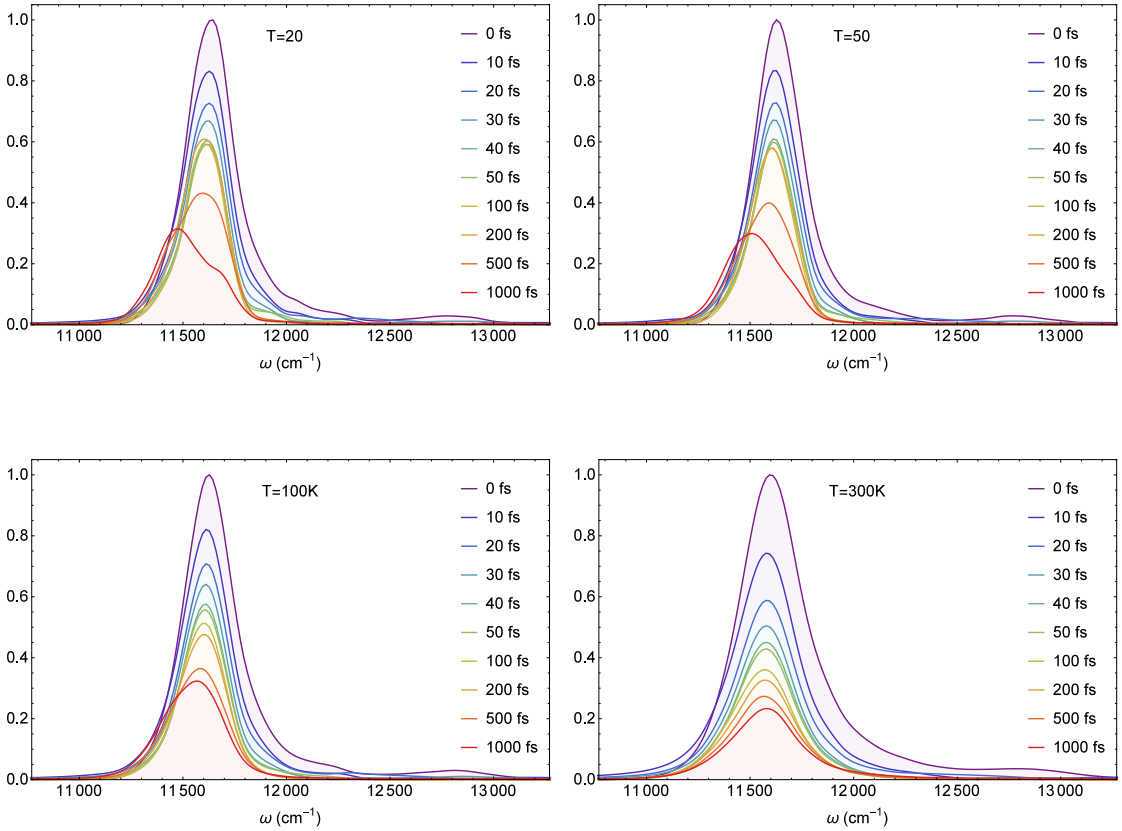

Fig. 3.11. Time resolved fluorescence spectra of the B850 ring.

At higher temperatures the thermally induced decoherence manifests on a faster time scale, leading to approximately exponential relaxation kinetics (see Fig. 3.11). Consequently time-resolved fluorescence follows the populations of excitonic states quite accurately and polaronic effects remain difficult to identify unambiguously.

As it turns out with the present set of parameters the polaronic effects remain hidden in the absorption or time-resolved fluorescence spectra. However, to test whether they need to be considered at all we perform an analysis of the wavefunction itself. We thus investigate the exciton participation parameter (Eqn. 1.102) and the coherence length parameter (Eqn. 1.103). The exciton participation ratio is calculated separately for each realization and then averaged, thus representing the wavefunction delocalization behaviour for each member in the statistical ensemble. The coherence length is obtained from the electronic density operator, so it includes the decoherence due to diagonal disorder in a different way.

As can be seen in Figs. 3.12 and 3.13a, at $t = 0$ the state is highly delocalized due to an excitation by a broadband pulse, with average exciton participation ratio of 11.5 and site coherence length of 10.5. Both delocalization parameters, participation ratio $L(t)$ and site coherence length $L^{[2]}(t)$, undergo a small decay in the

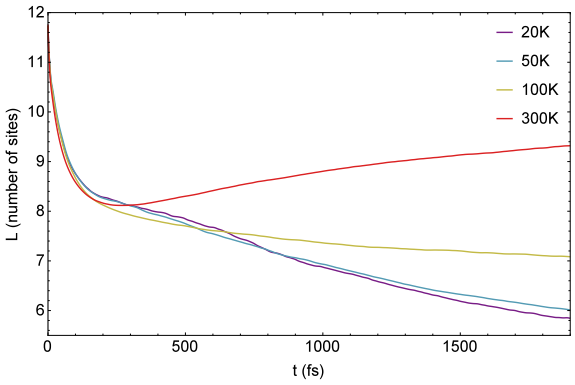

Fig. 3.12. Time evolution of the participation ratio, $L(t)$.

initial stages of the evolution ($\sim$100 fs) consistent with the decay of coherences. Then the participation ratio, $L(t)$, decays further at low temperatures, demonstrating characteristics of exciton self-trapping. However, at 300 K temperature the exciton participation starts to slightly increase in value from 500 fs. Overall at the time of 2 ps the participation grows with temperature. This result suggests that high temperatures counteract the self-trapping, inhibiting the localization process.

The coherence length, $L^{[2]}(t)$, shows a different temperature dependence. It decays rapidly up to 500 fs at all temperatures. It further decays down to $\sim$2 at time 2 ps at the high temperature of 300 K. However at low temperature (20 K) the coherence length grows up to the value of $\sim$7 from 500 fs to 2 ps. Thus, the overall picture is the following: at short times both parameters decay together with electronic coherences leading to the primary mixed state formation; later exciton participation grows with temperature, while the coherence length drops with temperature.

The coherence length not decaying completely and remaining at some fixed value confirms the non-optimality of the site basis. The site basis certainly is not the eigenbasis due to non-zero couplings between sites. Therefore we switch to the excitonic basis and show the coherence length in the excitonic basis set (Eqn. 1.104) in Fig. 3.13b. Again the length decays within a few hundred fs in accord with coherence decay and stays constant from 1 ps. Note that asymptotic values of $L_e^{[2]}(t)$ are generally much smaller, with the values being lower than 0.5. This implies that the excitonic states are close to the global eigenstates for the system. However, non-zero asymptotic values demonstrate the existence of polaronic effects.

The delocalization parameters demonstrate a complicated temperature dependence, which is revealed by the asymptotic values of L, $L^{[2]}$ and $L_e^{[2]}$. This is an additional proof for the formation of a polaronic picture at temperatures from 20 to 100 K. At 300 K $L_e^{[2]}$ asymptotically decays to zero signifying that only at room temperature the excitonic picture is valid.

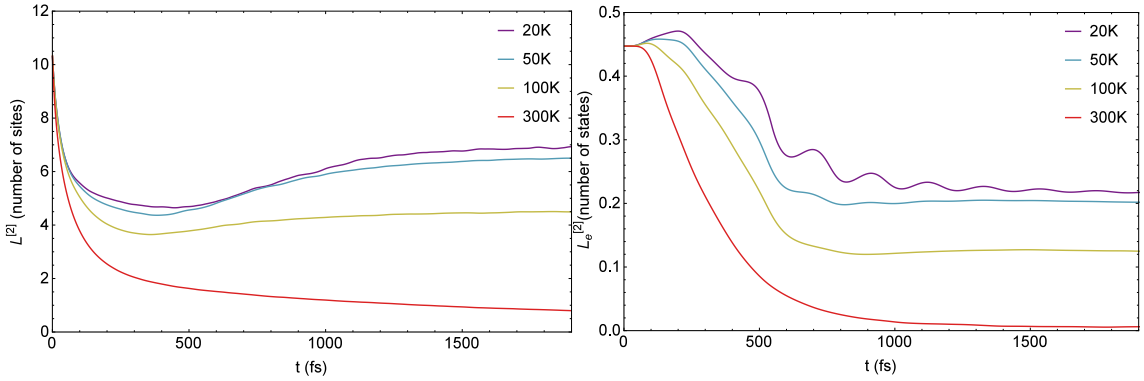

(a) Site basis $L^{[2]}(t)$.

(b) Exciton basis $L_e^{[2]}(t)$.

Fig. 3.13. Time evolution of the coherence length in site and exciton representations.

3.3.4 Discussion

The impact of the thermally fluctuating environment on the properties of the electronic excitations in the molecular aggregates is poorly understood. In the presented stochastic time-dependent variational wavefunction approach a large number of the environmental vibrational modes is treated explicitly and individual trajectories of the excitations with an initial stochastic state of the environment at a given temperature can be traced. Thus the environmental effect on the excitation dynamics can be explored in great detail. The distinctive feature of the presented approach in comparison to other similar ones[131,132] is that finite temperature is explicitly included: the energy of initial displacements of the vibrational modes follows a canonical distribution in accord with statistical physics. Each site is coupled to a separate pool of oscillators, with initial thermal states sampled independently. The presented method is non-perturbative, which lets us probe realistic systems where the resonant coupling and the reorganization energy are of the same order, without having to consider one of them as a small perturbation. Also due to the explicit treatment of phonon modes an arbitrary form of the spectral density function can be assumed, including both continuous spectral density functions and specific prominent molecular vibrational modes. Timescales of various relaxation processes, attributed to electronic coherence decay, which is caused by static disorder, and to the influence of the thermal bath can be extracted using the present model. A direct comparison to ultrafast time-resolved spectroscopy experiments can be drawn using the modeled spectra.

LH2 is an ideal object to study the complexity of dissipative excitation dynamics. The approach and the parameters of the electronic subsystem and the vibrational bath are validated by studying absorption (and fluorescence) spectra as well as pop-

ulation dynamics. The energy transfer times within rings of LH2 complexes were experimentally established. The relaxation within the B800 ring was estimated to take about 0.3 - 0.4 ps. at all temperatures.[107] Fast intraband equilibration of 100 - 200 fs was estimated for the excited states of B850 at 77 K for the LH2 complex of Rhodospirillum (Rs.) molischianum.[120] Indeed, we obtain rather similar excitation relaxation and transfer times at 100 K (Fig. 3.10) considering only the B850 ring. The relaxation dynamics in LH2 of Rhodobacter (Rb.) sphaeroides at room temperature obtained from the polarization controlled two-dimensional electronic spectroscopy shows a 200 fs component for the relaxation of the B850 high-excited states (identified at 770 nm),[114] which is slightly higher than what we observe in our modeled time-resolved fluorescence spectra. This can be partially explained by relaxation pathways involving intramolecular high-frequency molecular vibrations which were not included in our simulations.

An additional property which we can address using our approach is the controversial high-excitonic component of the B850 ring.[47,109,111,133] The question of existence and spectral prominence of the high-excitonic component becomes significant since the excitonic effects at ambient temperatures are apparently highly prominent. The broadband pulse excitation creates populations in the higher energy excitonic states, which manifest themselves as a broad shoulder extending from $\sim$12500 cm^{-1} to $\sim$13000 cm^{-1}, and its fast decay during the initial 30 fs of the evolution can be observed (Fig. 3.11). Its low amplitude makes it difficult to discern in experimental measurements. The high-excitonic component of the B850 band was estimated to be at approximately 780 nm (12820 cm^{-1}) for Rb. sphaeroides at 77 K[109] or near 755 nm (13245 cm^{-1}) at 100 K[111] similarly for Rb. sphaeroides and Rhodoblastus (Rps). acidophila. As expected, it is superimposed with the line of the B800 ring in the total spectrum.

The interplay between excitonic effects and nuclear relaxation can cause the evolution of polaronic dynamics and the variational approach includes these effects non-perturbatively. Here we show that the polaronic properties do not affect properties of optical absorption. Its associated spectrum is determined by the decay time of the linear response function ($\sim$100-200 fs). The ultrafast time-resolved fluorescence of LH2 also hardly reveals any polaronic properties because the spectral composition reflects the structure and the symmetry of excitonic energy levels (Figs. 3.10 and 3.11).

Therefore we look at intrinsic wavefunction properties. The calculated participation parameter exceeds the corresponding parameter measured in experiments. An exciton delocalization factor of 5 pigments was estimated from the analysis of the LH2 single-complex emission at 1.2 K.[125] This value is in agreement with the delocalization we obtain at low temperatures. However, the simulations of the exper-

imental femtosecond transient absorption and time-dependent pump-probe spectra of bulk LH2 samples performed by different groups suggested the delocalization over 4 - 6 sites around 1 ps. (or steady-state limit) at room temperature and 77 K.[106,134,135] The authors stayed within the excitonic picture with the Redfield relaxation approximation, thus the delocalization was essentially determined by the interplay of the resonance coupling and the energy disorder in the system. Our previous modeling of nonlinear spectra of an LH2 ensemble using the Redfield approach[117] showed that excitons are delocalized over 3-4 pigments in B850 ring both at 77 K and at room temperature. These values are significantly smaller than the ones we obtain at corresponding temperatures and delay times for a single realization averaged value in present simulations (Fig. 3.12). However the present approach is qualitatively different from the ones used in a previous work[117] and in refs.,[106,134,135] and allows us to take into account thermal fluctuations already at the wavefunction level.

In essence, the wavefunction of every individual realization (corresponding to single complexes in a medium) is largely delocalized as shown by the $L(t)$ parameter. Highly populated sites contribute heavily to the self-trapping effect, leading to the decay of the exciton participation ratio. We find that asymptotic long time values of delocalization parameters are most relevant to inspect the polaronic effects. At low temperatures exciton participation $L(t)$ becomes small denoting self-trapping. At the same time the excitonic coherence length $L_e^{[2]}$ becomes large signifying large departure from the excitonic picture. At high temperature the thermal fluctuations impede self-trapping, increasing the delocalization of the wavefunctions. However, this does not imply some kind of different polaron formation, because at high temperature the wavefunction represents a thermally excited superposition of many excitons. The decay of $L_e^{[2]}$ at 300 K on the contrary signifies the validity of the excitonic picture: the resulting wavefunction delocalization in real space is merely due to thermal activation of several excitons. We thus find that the proper description of delocalization and polaron formation requires the inspection of both participation and coherence parameters simultaneously.

However, whether large participation ratios necessarily correspond to the presence of *coherence* between the pigments is a nontrivial question. Notice that even with large exciton participation ratios at high temperatures in individual rings we do not have large exciton coherence lengths, $L^{[2]}$. These become even more reduced by increasing temperature. This seemingly conflicting result implies a fluctuation-induced decoherence process between distant sites inside a single B850 ring: the fluctuations will randomize phase relationships between distant sites in a single wavefunction. We thus observe the decoherence effects within a single B850 ring at large temperature and this explains the temperature-induced reduction of the co-

herence length.

Both parameters demonstrate signatures of excitonic polaron formation. If the picture were purely excitonic, the wavefunction coherence properties must be temperature independent. Now both parameters, $L(t)$ and $L^{[2]}(t)$ demonstrate a strong temperature dependence implying a transition from temperature-independent excitonic system symmetries to the temperature-dependent polaronic picture.

The timescale of polaron formation is yet another important parameter characterizing the spectral signature of the polarons. Coherence decay between the wavefunctions in the thermal ensemble (the fast decrease of delocalization during the first 500 fs) mostly coincides with the decay time of the optical response function and of the electronic coherences shown in Fig. 3.8. These coherences shape the absorption spectrum. This makes the polaronic effects impossible to observe in absorption spectra of the system. The time-resolved fluorescence, according to our simulations, approximately follows excitonic populations. This may be the result of the fact that our long-time coherence length in the excitonic basis is considerably smaller than 1, which may be related to our restrictions of the model parameters. Specifically, we did not include the vibration-induced variations of intermolecular couplings. This is the major cause of exciton self-trapping observed by the temperature dependence of the fluorescence lifetime[47,49] in real photosynthetic aggregates.

The delocalization also depends on the specific spectral content of bath fluctuations. If the bath fluctuations are very slow, as demonstrated in ref.[1] and in the previous chapter, the wavefunction becomes adiabatically trapped by energy deformation. More specifically, the slow phonon modes act as quasi-static disorder and hence necessarily localize the excitonic wave function in the Anderson sense, i. e. the disorder parametrically or adiabatically localizes quantum particles. Thus, the localization does not necessarily involve the response of vibrational coordinates to the excitation or the feedback of the interaction. Simple thermal fluctuations will induce localization. Consequently higher temperature will cause more localization. If the high frequency molecular vibrations are in place, the polaronic effects mostly manifest due to the feedback action. In this case the higher temperature will cause detrapping. In the present simulations we observe thermal detrapping. The effect is due to the thermal reduction of interaction feedback, thus our vibrational modes are in a high frequency regime.

The vibrational frequencies strongly overlap with excitonic energy splittings and the thermal energy k_BT. Overlapping energies allow a strong mixing of electronic and vibrational degrees of freedom, while thermal activation leads to the vibronic dynamics. Finally, this phenomenon may assist fast relaxation between energy bands in LH2 and fast exciton transport in other photosynthetic systems.

There is another temperature-related issue that should not be ignored while de-

scribing realistic LH2 aggregates. Numerous experiments and modeling show that various system and environment related parameters of the LH2 complex depend on temperature and this dependence is not simply linear.[47,111,117,121,136] The present model is therefore not fully comprehensive to accommodate all features of the LH2 aggregate.[128,137,138] The parameters used in the present modeling are those previously determined for 100 K temperature.[117] Consequently, the direct comparison of the results presented here with those obtained elsewhere for the LH2 complex is tenable only for 100 K. We intentionally keep the same parameters at all temperatures in order to reveal the manifestation of the temperature effects in the properties of the wavefunction. However, this opens up a new topic in the study of polaronic effects in molecular aggregates: the inclusion of nonlinearities. The next chapter is dedicated to construct a model for nonlinear system-bath interactions within the sTDVA framework.

Summing up, we have applied the sTDVA approach to model the energy transfer within the B850 ring of the LH2 photosynthetic complex. In contrast to other applications of the variational wavefunction approach, which consider the zero-temperature case,[131,132] we simulate the dynamics at finite temperatures by randomly sampling initial amplitudes of vibrational modes. The modeled results demonstrate that polaronic effects are small in optical absorption and fluorescence spectra in this specific aggregate. However, the dependence of wavefunction delocalization parameters $L(t)$, $L^{[2]}(t)$ and $L_e^{[2]}(t)$ and especially their asymptotic values signify a transition to a temperature-dependent polaronic picture.

Chapter 4

Nonlinear effects in energy transfer and spectroscopy

4.1 Introduction

One of the advantages of the sTDVA approach is that it is not restricted to a bilinear form of the system-bath coupling, allowing more sophisticated forms of vibrational potentials. The two well-established consequences of the linear coupling to vibrations, the mirror-image of absorption and fluorescence as well as zero linewidth of the so-called zero-phonon line are usually violated in experiments. The effects of higher order couplings on the dynamics of electronic states have to be included, while they are poorly studied. In this chapter we use the TDVA approach with a new type of trial wavefunction to investigate the effects of frequency shifts in vibrational potentials between different electronic state manifolds (a quadratic coupling effect) on quantum dynamics and optical spectra of coupled electronic-vibrational systems. We find that squeezing of vibrational wavepackets is necessary for the proper description of molecular states and to recover nonlinear effects. The derivations of the equations of motion and the theoretical background between the added terms in the Hamiltonian are all presented in Chapter 1.6, and here we will focus on constructing a model, describing the numerical simulations and interpretating the results.

4.2 Squeezing dynamics and lineshapes of a single absorber

First we look at the simplest possible scenario, which is a single molecule (transition energy is shifted to zero) coupled to a single vibrational mode with slightly different vibrational frequencies for ground and excited states. We set the frequency of the mode to $\omega = 200\mathrm{cm}^{-1}$ and the linear coupling strength between the site and the mode corresponding to a Huang-Rhys factor $S = 0.5$, which corresponds to a

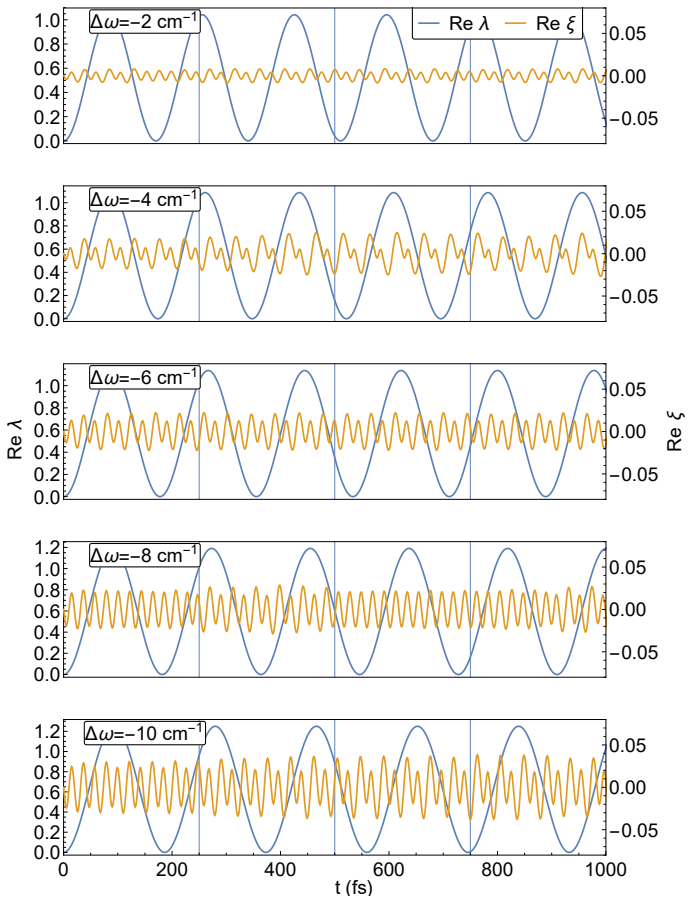

Fig. 4.1. Time evolutions of vibrational wavepacket displacement and squeezing with different values of $\Delta\omega$ (frequency difference between the ground and excited state mode). The blue line denotes the real part of displacement parameter (position of the wavepacket on the generalized coordinate axis), the orange line corresponds to the real part of squeezing parameter (stretching of the wavepacket along the generalized coordinate axis).

reorganization energy of $\Lambda = 100\mathrm{cm}^{-1}$. The calculations are performed for a set of frequency shifts between the ground and excited state manifolds as marked by $\Delta\omega$ in Fig. 4.1.

Figure 4.1 shows the time evolutions of the real part of the displacement parameter λ and the real part of the squeezing parameter ξ, corresponding to the generalized coordinate of the wavepacket and its squeezing along the coordinate axis. The imaginary parts of the same parameters (not shown) correspond to generalized momentum and squeezing along the momentum axis accordingly. The oscillations of the wavepacket position in the excited state are consistent with the frequency shift of the excited state potential, producing a lower frequency with increasing nonlinearity parameter (longer period of oscillations). The absolute value of the squeezing parameter also increases with the nonlinearity parameter, consistent with the hypothesis that nonlinear interactions cause deformations of the Gaussian wavepackets. The frequency of the oscillations of the squeezing parameter is consistent with Eq. (1.87) (with the base frequency equal to double the frequency of the harmonic oscillator and modulated by the nonlinear term). This particular form of the nonlinear term does not introduce any bias in the squeezing dynamics, and the average value of squeezing along any axis over time is equal to zero.

The effect of nonlinear terms on the optical response is highly dependent on the

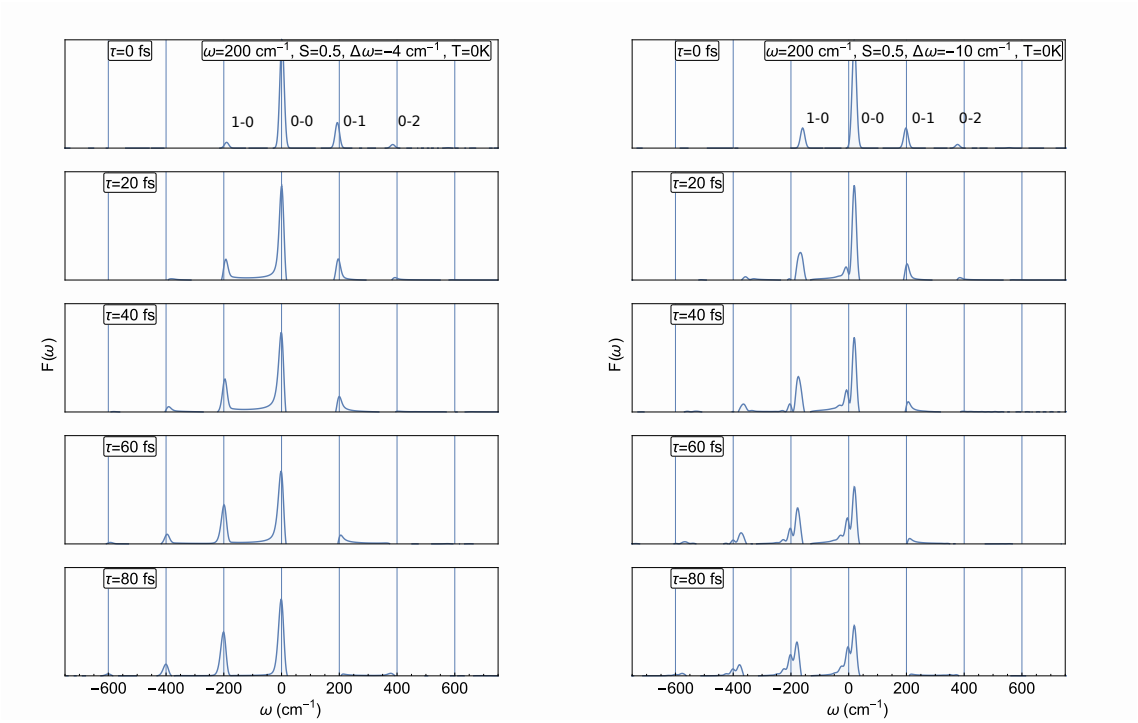

(a) Low nonlinearity **(b)** High nonlinearity

Fig. 4.2. Auxiliary time-resolved fluorescence signals of a single absorber coupled to a single mode with nonlinearity at zero temperature.

strength of the nonlinear interaction. In Figure 4.2a we show the ATRF spectrum. The ATRF at $\tau = 0$ fs shows a peak corresponding to a $(1-0)$ transition at $\tau = 0\,\mathrm{fs}$ which does not manifest when there is no nonlinearity. Its intensity increases with the nonlinearity parameter. It rises because of the different wavepacket evolution in the excited state compared to the ground state. In the absence of the nonlinearity, the lowest energy peak at $\tau = 0$ fs corresponds to a $(0-0)$ transition, with the $(1-0)$ peak amplitude being zero. The presence of this peak is usually attributed to temperature effects and absorption from the hot ground state in linear models, although it is a feature of non-parabolic potentials.[139] There is an additional subtle broadening of the lineshapes due to nonlinear terms.

Increasing the nonlinearity parameter (Figure 4.2b) increases the intensity of the $(1-0)$ peak at $\tau = 0\,\mathrm{fs}$ and overall we obtain a rich structure where every peak in the vibrational progression splits over time, generating a sub-progression in the low energy direction. The fine structure gets increasingly prominent with the time evolution of the system.

The spectral splitting due to the nonlinearity is highly dependent on the position of the wavepacket, resulting in a set of Frank-Condon peaks that do not adhere to the well-known Poisson distribution at zero temperature. With higher temperature the set of relative transition frequencies becomes very dense, leading to continuous

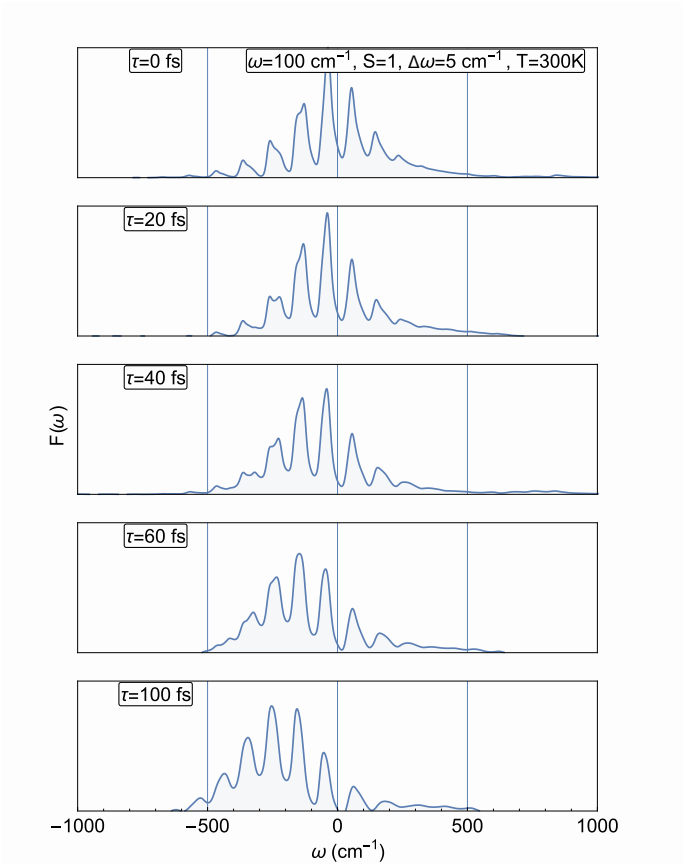

Fig. 4.3. Auxiliary time-resolved fluorescence signals of a single absorber coupled to a single mode with nonlinearity at room temperature.

spectral features even in a simple one site/one mode scenario. This is shown in Figure 4.3.

For this calculation we used a lower-frequency mode to emphasize the thermal features. As can be seen, the combination of high temperature and nonlinearity introduces additional broadening and fine features in the spectrum due to the density of the possible transition frequencies. This type of line broadening is often seen in fluorescence line narrowing experiments.[79]

4.3 Continuous spectral density

For the calculations of relaxation in the presence of a nonlinearity and of associated spectral signals we couple the site to $Q = 200$ modes with frequencies equally spaced in the range $\omega \in (0.01,\, 300)\mathrm{cm}^{-1}$. We use the super-Ohmic form for the spectral density function, defined as

$$C_n''(\omega) = \omega^3 \exp\left(-\frac{\omega}{\omega_c}\right), \tag{4.1}$$

where ω_c is the cutoff frequency. The reason for choosing this specific form is that the super-Ohmic spectral density function features a prominent zero-phonon line in the optical spectra, which is missing in models where $C_n''(\omega) \sim \omega^1$ at low

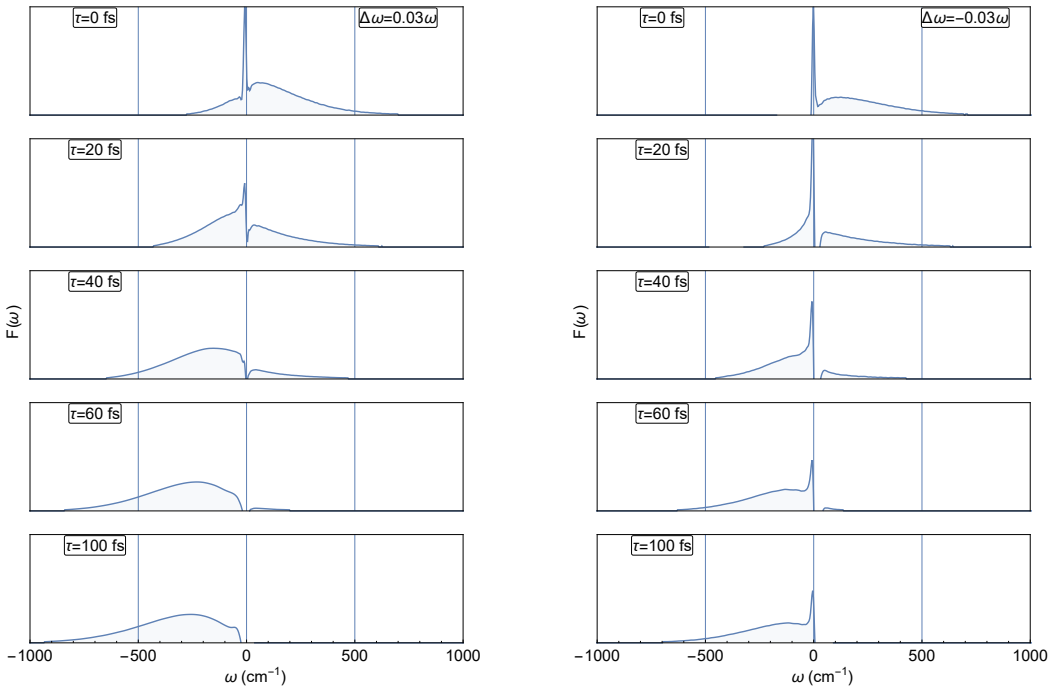

(a) Positive nonlinearity **(b)** Negative nonlinearity

Fig. 4.4. Auxiliary time-resolved fluorescence signals of a single absorber coupled to a super-Ohmic phonon bath with nonlinearity at zero temperature. The frequency of each mode is shifted by a constant multiple of its frequency.

frequencies. The coupling constants are determined from Eqn. (4.1), and the bath timescale is set to $\omega_c = 53\mathrm{cm}^{-1} \equiv 100\mathrm{fs}$. For each phonon mode we set the nonlinearity parameter as $\left(\omega_q^{\mathrm{e}} - \omega_q^{\mathrm{g}}\right) = \Delta\omega = u\omega_q$, where u is a constant. The temperature is set to $T = 0\,\mathrm{K}$. Positive u corresponds to phonon frequencies being higher in the electronic excited state manifold.

In Figure 4.4 we show the calculated ATRF spectra. The first apparent effect is the expected breaking of mirror symmetry between $\tau = 0$ and $\tau \to \infty$ spectral signals (i.e. between absorption and relaxed fluorescence). Second, in case of a positive nonlinearity the zero-phonon line features a slight redshift and decays during the time evolution of the spectrum. As the phonon bath is overdamped, we do not observe any oscillatory dynamics. Only the gradual redistribution of the phonon-induced sideband from r.h.s. to l.h.s. of the ZPL is prominent. Notice that at a certain configuration of parameters we observe the complete disappearance of the sharp ZPL because of the varying shifts of phononless transitions of different oscillators (very small negative amplitudes appear due to numerical propagation errors, however, their amplitudes can be diminished by improving the accuracy of the numerical propagation). The ZPLs and phonon sidebands are usually well resolved in fluorescence line narrowing (FLN) experiments[79] . The level of nonlinearity

in our parameters is certainly exaggerated. However, we essentially learn that the FLN experiments detect the phonon side-bands of the emission process. The same side-bands of the absorption process may show a completely different picture.

4.4 Population dynamics and associated spectral signals of a multi-site system

A much more complex scenario involves a set of sites where each site is coupled to a set of local modes or a phonon bath. The interplay between the electronic energy transfer and the local bath polarization can drive the system to various qualitatively different regimes of time evolution, as shown in multiple studies of ring systems[2,34,131] , spin-boson models,[98,140] etc. Here we wish to investigate the effect of a nonlinearity on the electronic energy transfer and the associated spectra in a model ring system. Although calculations of the LH2 aggregate are a tempting topic (as shown in the previous chapter), it is too complicated if one wants to specifically isolate the effects of nonlinearities. So for the following calculations we use a simplified ring model.

We use a ring of $N = 11$ sites labeled as -5, -4, ... 5, each coupled to a single local mode of frequency $\omega = 100], \mathrm{cm}^{-1}$, chosen to be close to the excitonic splitting. The Huang-Rhys factor for each site is $S = 0.5$. All site transition energies are set to 0, and the nearest-neighbor coupling is set to $H^{el}_{n\neq m} = 20\,\mathrm{cm}^{-1}$. We choose an initial state of $|\alpha_0|^2 = 1$ for excitation dynamics calculations, and an optical excitation for calculations as an initial condition for the spectral calculations. The site transition dipoles of the ring system are set as $d_n = \left(\cos\frac{2\pi}{N}n, \sin\frac{2\pi}{N}n, 0\right)$.

The evolutions of the site excitation populations and the phonon displacements along the coordinate are shown in Figure 4.5. The electronic evolutions displayed in the pictures are very weakly affected by the mode frequency shifts. The phonon displacements display a similar oscillatory behaviour consistent with the frequency shifts caused by the nonlinearity. However, the squeezing parameters (not shown) develop a slight bias, with the wavepackets getting stretched along the coordinate axis in coordinate-momentum space in case of negative frequency shifts, and stretched along the momentum axis in case of positive frequency shifts. The TRF spectra (Figure 4.6) also show weak secondary sidebands for each peak in the vibrational progression. Spectral shifts of the vibrational sidebands depending on the sign of the nonlinear coupling parameter are obvious. However, the intensities of sidebands are weakly affected.

We also simulate the dynamics of a ring system with the same parameters for the electronic transition energies and the resonant couplings, but this time we couple each site to a bath of $Q = 100$ phonon modes with coupling strengths set ac-

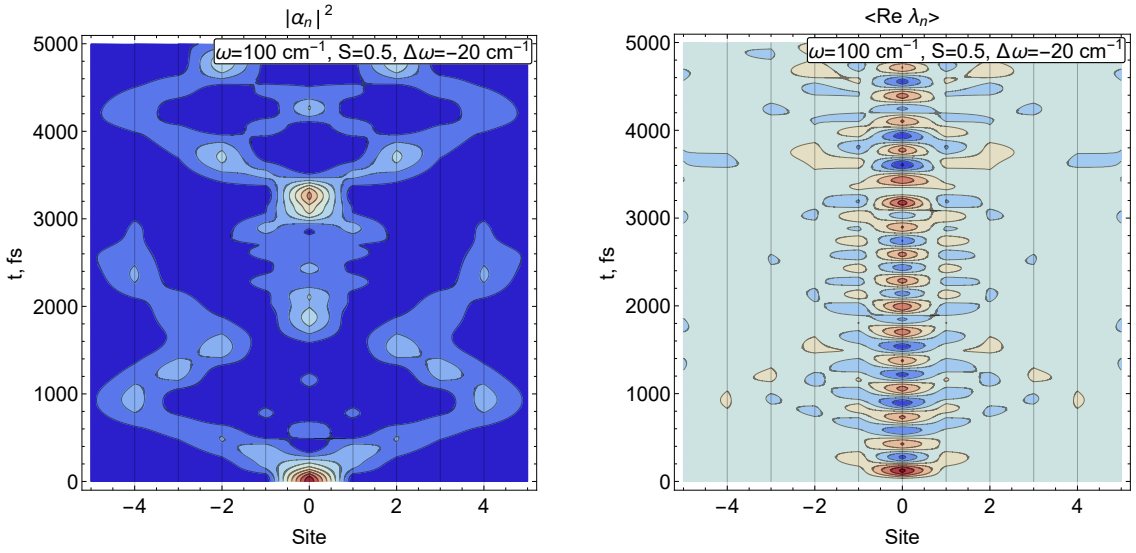

(a) Negative nonlinearity

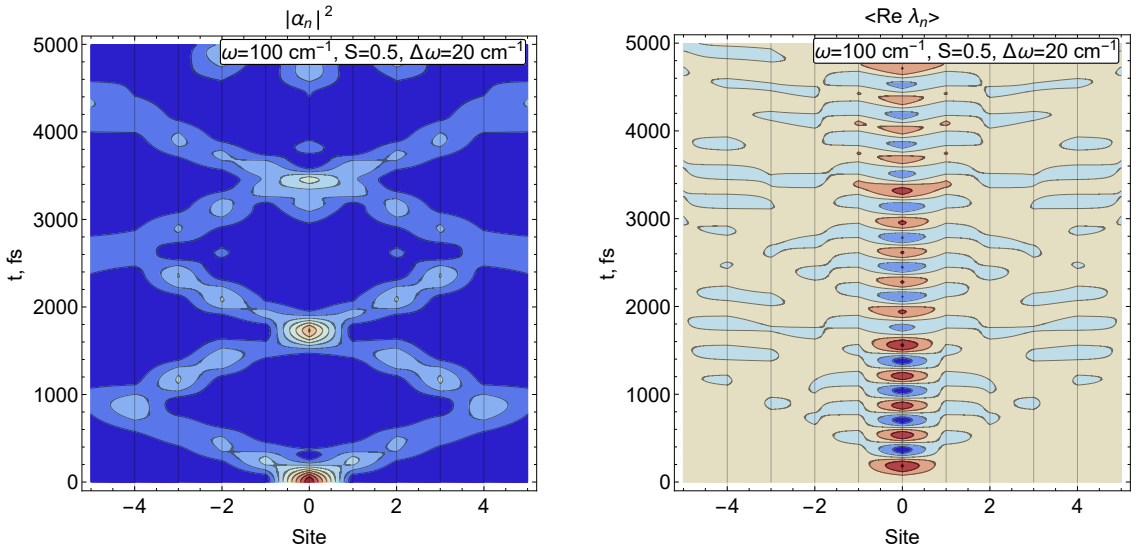

(b) Positive nonlinearity

Fig. 4.5. Population dynamics and phonon mode displacement dynamics of a ring system of $N = 11$ sites, with each site coupled to a single phonon mode with positive or negative nonlinearity.

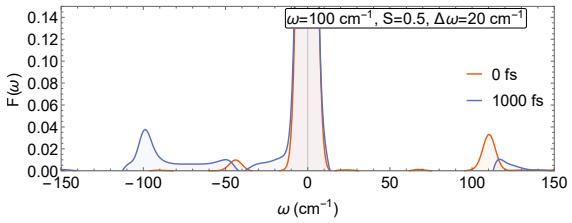

(a) TRF spectrum with positive nonlinearity

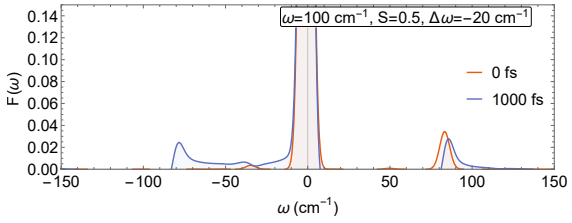

(b) TRF spectrum with negative nonlinearity

Fig. 4.6. Auxiliary time-resolved fluorescence signals of a of a ring system of $N = 11$ sites, with each site coupled to a single phonon mode with positive or negative nonlinearity.

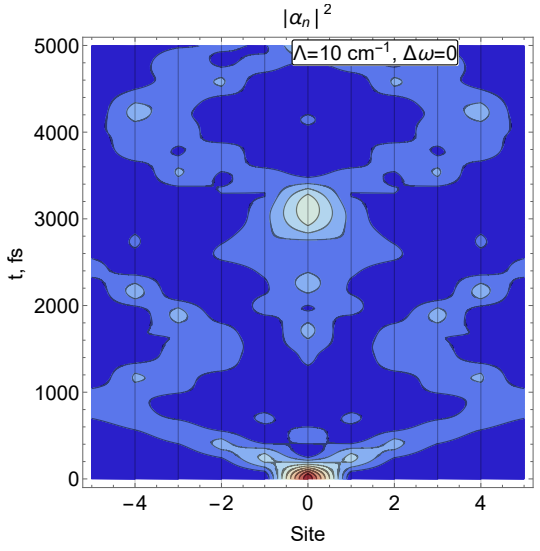

(a) Population dynamics without nonlinearity

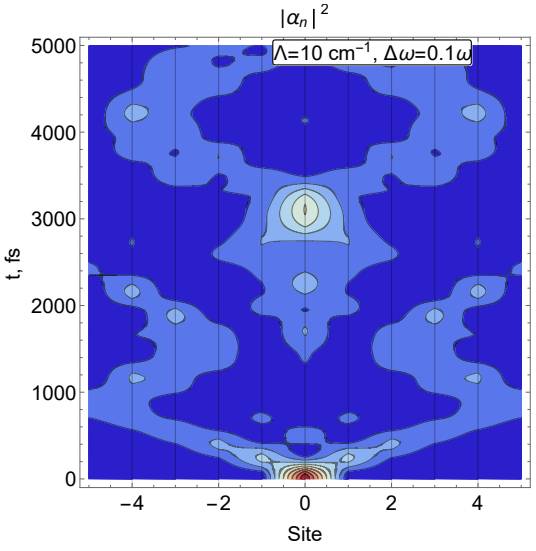

(b) Population dynamics with nonlinearity

Fig. 4.7. Population dynamics of a ring system of $N = 11$ sites, with each site coupled to a super-Ohmic bath of $Q = 100$ phonon modes with and without nonlinearity.

cording to a super-Ohmic spectral density. We choose a very slow bath timescale $\omega_c = 53\,\mathrm{cm}^{-1} = 100\,\mathrm{fs}$ so that the maximum of the spectral density function would be close to the resonant coupling strength, enabling resonant effects in energy transfer. As shown in Figure 4.7, in case of an overdamped bath the effect of a small frequency shift applied to each mode has little effect on population dynamics. Hence the energy transport in excitonic aggregates is robust against vibrational nonlinearities, at least in symmetric aggregates. The exchange narrowing mechanism[40] (the resonant interaction between constituent sites of the system) is known to reduce the effective linear system-bath coupling, and this also applies to nonlinear interactions.

4.5 Numerical properties of the approach

The lineshape theory for complex potentials is well-developed for single absorbers coupled to a single mode, see ref.[139] for a review of established methods for polynomial, Morse, and general potentials. In principle, the extension of these approaches to larger systems is usually possible, but computationally prohibitive. For methods such as exact diagonalization or the multiconfigurational time-dependent Hartree approach, the exponential growth of the Hilbert space restricts the dynamical calculations to very small systems with a few nonlinear modes. The time-dependent variational approach requires a solution of a large system of coupled ODE's, however the computational effort scales linearly with propagation time, linearly with the number of included phonon modes and quadratically with the number of included system sites. For calculations at finite temperature the calculation scheme is highly parallelizable and scales well to any number of available computing cores.

Unlike perturbative methods, sTDVA does not make any assumptions about the relative strength of the interactions. However, benchmarking has shown that the accuracy of this method is worse in the Redfield regime, where the system-bath coupling is much weaker than the resonant coupling.[3] The accuracy of the sTDVA approach in presence of strong nonlinear interactions is presently being evaluated, and making a direct comparison with a multi-site and multi-mode system is difficult because state of the art exact methods such as HEOM assume a linear system-bath coupling. In this set of simulations we have used low values of nonlinearity parameters in line with what is expected in real molecular aggregates.

The solution of the ODE system is done using an adaptive time step Runge-Kutta solver. Depending on the nonlinearity term used, the equations of motion may have a term that exhibits a divergence at low values of the squeezing parameter when the phase of the squeezing becomes undefined. We regularize the diverging terms using an additional multiplier $(1 - \exp(-\alpha_c \xi))$, with α_c being the numerical cutoff of the order 10^{-10}.

4.6 Final remarks

The fine structure of spectral lineshapes introduced by higher-order couplings is invisible in room-temperature experiments due to an abundance of broadening mechanisms, obscuring the weak non-linear features. It can be argued that weak nonlinear effects are mostly hidden at liquid nitrogen temperature ($T = 77\,\mathrm{K}$) as well since the thermal broadening of the ZPL becomes very large. The thermal energy $k_B T$ at 77 K is equal to $53\,\mathrm{cm}^{-1}$, which is well above the energies corresponding to the nonlinear part of the Hamiltonian for realistic values of frequency shifts. How-

ever, experiments at $(T = 4\,\mathrm{K})$ may reveal the vibrational substructures caused by nonlinearities and anharmonicities of vibrational potential surfaces.

Aside from the fine vibrational structures at low temperatures, we also observe spectral broadening and generation of continuous spectra when including a nonlinearity at finite temperatures. Although there is a multitude of mechanisms that could lead to the same result, for example damping or ensemble-wise disorder among the phonon frequencies, usually the effects are included on the phenomenological level, using secondary baths or hyperparameters for the simulation.[11,141] In this chapter we showed that a continuous spectrum may be obtained with only one mode from first principles, without the inclusion of any explicit relaxation mechanism and as a direct effect of nonlinearities.

The ring system model displayed a very weak effect of the nonlinearity on the coherent energy transfer within the ring even with vibrational frequencies close to the excitonic splitting. This is not surprising, as the nonlinear effects are still an order of magnitude weaker than the linear system-bath coupling using a realistic set of parameters. So while it is still somewhat relevant for describing the energy transfer and relaxation in molecular aggregates, the nonlinear effects are expected to play a bigger role in intramolecular conversion and relaxation, e.g. in carotenoids,[142] as opposed to intermolecular energy transport.

The sTDVA approach allows direct simulation of excitation dynamics for large aggregates coupled to large numbers of nonlinear modes, but the electronic dynamics are already nonlinear in non-perturbative regimes, where the system-bath and resonant couplings are of the same order, even using only the linear terms in the Hamiltonian (strictly speaking the electron-phonon coupling is bilinear). This is due to bath polarization effects and the transition to a polaronic basis, as discussed in refs.[1,2] and throughout this thesis. The combined dynamics can be driven towards qualitatively different regimes, depending on relative couplings, phonon frequencies and bath timescales. As a result, separating the effects using only linear spectroscopy is impossible, and even time-resolved methods require a substantial analysis considering all the parameters of the studied system both at low and high temperatures. For example, it was proposed that nonlinear effects may influence the surface shape of the peak in 2D spectroscopic signals,[143] which is consistent with continuous spectrum generation (a high-temperature feature). Temporal dynamics of vibrational fine structures and the effect of different potential surfaces on 2D spectroscopic data so far remain a promising field of study.

Summary of the results

According to the goals formulated in the beginning of the thesis, two milestones were achieved in the presented research. The first one was the development of the stochastic time-dependent variational approach for the simulation of quantum dynamics and optical response signals in molecular aggregates. The second was studying the dynamics of excitonic polaron formation using the developed approach. The specific purpose of developing sTDVA was to analyze the quantum dynamics in a complex regime, where no interaction can be considered small and the bath polarization (excitonic polaron formation) is expected to play a big role in energy transfer and molecular optical response. Another very important distinction from other applications of the variational approach encountered in recent literature[93] is that we introduced local couplings: the absence of correlations between fluctuations and reorganizations of spatially separated sites.

At the time the research was mostly motivated by the idea that excitonic states of molecular aggregates are not the pointer states of the electron-phonon supersystem. This means that after a long time (compared to all timescales of electronic energy transfer and bath relaxation) the reduced density operator of the electronic system is not diagonal, and coherences between purely excitonic states persist indefinitely. The search for a way to find out the "true" quantum states of such systems began long before the author's own research, dating back to W. Zurek's einselection theory.[126] However, in application to the theory of molecular aggregates more recent developments come to mind, for example a model of fluorescence in LH2 aggregates[46] and the HEOM approach analysis of time dynamics of a model two-site system.[12] The goal of the research was to construct a theoretical description that by design incorporates the possibility of electronic states being "dressed" by phonons, and examine the whole dynamics of "how the transition occurs". The methods for obtaining only the "final" polaronic state without focusing on the evolution were already present at the time.

Using the zero-temperature case, initially we were able to show the dynamical picture of polaron formation. Using a few chosen parameter combinations we have found two major qualitative regimes of polaronic state evolution, which depend on the ratio between the timescale of bath reorganization and the timescale of elec-

tronic energy transfer. Simply explained, if the bath timescale is much faster, then the environment rapidly reorganizes after the molecular aggregate is excited to an electronic eigenstate, and this produces Rabi oscillations between the local site excitations that are driven by a rapid energy shift caused by local polarization. If the bath timescale is comparatively slow then the dynamics are driven by slow adiabatic transition of the excitonic states into polaronic states, and in this case no Rabi oscillations occur.

The effective Hamiltonian approach was used for analysis and interpretation of the results, mapping the coupled exciton-phonon system into a reduced purely electronic system with time-dependent couplings between electronic states. This allowed the interpretation of the polaronic state transition as a time-dependent screening (reduction of the effective resonant coupling between electronic states) and gave the possibility to draw parallels with established results in the theory of solid state systems. We have also obtained intrinsic relaxation with the effective electronic Hamiltonian due to off-diagonal elements obtaining complex-numbered values.

Most of the processes associated with physics of molecular aggregates, such as light harvesting, electronic energy transfer, charge separation etc., usually happen at ambient temperatures in the outside world, or at least at liquid nitrogen temperature in spectroscopy experiments. So naturally the zero-temperature case was not the end goal, though useful for model applications. The theory had to be expanded to include the possibility of the bath being at a higher temperature than absolute zero. Using a stochastic sampling scheme for the initial conditions of the bath and thermally averaging over high numbers of initial conditions we were able to reconstruct the density operator approach, this time with the complete dressed electronic states. The new stochastic scheme was first benchmarked against an established method to test its limitations and find regimes where the novel calculation scheme would display insufficient accuracy. This benchmarking became an important part of the presented research, affirming the validity of all other results presented throughout the thesis.

The next step was applying the developed calculation scheme to a real photosynthetic molecular aggregate. We have investigated the excited state dynamics and the transition to a polaronic state at finite temperatures in the LH2 complex. Taking the parameters featured in calculations done with a different approach, we have shown that the optical absorption spectrum (which only features the very early post-excitation dynamics) are consistent with the traditional Redfield scheme. The auxiliary time-resolved fluorescence modeling, where the Redfield approach is expected to fail for this specific aggregate due to the large system-bath coupling, was also presented. The interplay of polaron transition dynamics, electronic energy transfer, disorder-induced broadening, coherence decay and other contributions to

this spectral signal was analyzed using the obtained electronic state dynamics and auxiliary calculations to isolate all the mentioned contributions.

We have also introduced measures to quantify how "polaronic" a state is for this analysis. The combination of the averaged exciton delocalization of a single wavefunction and coherence lengths in different representations allowed to provide a temperature-dependent picture of the dynamics of polaron formation in the LH2 complex. The limit cases were successfully captured, such as the state being least polaronic at ambient temperatures, and the timescales of the transition were extracted. This also helped address the confusion between the multiple reported values of the delocalization length from experiments. We have shown that the delocalization length reported from single-molecule experiments and the coherence length inferred from ensemble measurements are not the same quantity, and our modeling results were able to consistently incorporate both numbers in the context of experimental data. The delocalization length grows with temperature, and higher numbers are associated with a decreased self-trapping effect. The coherence length decays with temperature, and higher values of coherence length in excitonic basis signify that the density operator is not diagonal, and excitonic states are not the pointer states of the global electron-phonon system.

The last part of the research presented in this thesis was focused on yet another expansion of the approach, this time to incorporate the possible nonlinear couplings between the system and the bath. Experimentally some of the nonlinearity effects were observed already, such as mirror symmetry breaking between absorption and fluorescence signals, and zero-phonon line broadening.[137] To account for nonlinear effects we have introduced a new variational Ansatz based on squeezed coherent states, well known in quantum optics. To isolate the effects without getting confused by large amounts of free parameters we once again performed simulations on model systems. One of the essential results of this modeling was that the spectral signals displayed a range of characteristic signals. The first one was a vibrational fine structure, where every peak in the vibrational progression would split into a sequence of smaller vibrational peaks. This is an intuitive result that one would expect from exact calculations (in case of a single absorber at zero temperature they can be performed). However, we were also able to show that at finite temperature the vibrational fine structure gets progressively dense to the point when even a single vibrational mode can generate seemingly continuous regions in an optical absorption spectrum. These continuous regions are often seen in experiments and they are usually described phenomenologically. In contrast, we obtain the result with a purely ab initio calculation.

The result of mirror symmetry breaking was also achieved with a single absorber nonlinearly coupled to a continuous bath. We have shown that different signs of the

nonlinear coupling terms lead to scaling of late-time sideband shoulder lengths in different directions on the energy axis. The time evolutions were shown using the tool applied throughout the research presented in the thesis, namely the simulated auxiliary time-resolved fluorescence spectra.

Finally, we have performed calculations on a system that, to our knowledge, no other modern theoretical approach can currently handle: a multi-site system nonlinearly coupled either to local high-frequency vibrational modes or to a local phonon bath. Using this model system we were able to show that the vibrational nonlinearities produce the characteristic mirror symmetry breaking in the ATRF spectra, but the influence of the nonlinear couplings on electronic energy transfer is negligible. The exchange narrowing mechanism was proposed to explain the robustness of state dynamics. We believe that the results are important when interpreting experimental data, because discerning between electronic and vibrational effects in nonlinear optical spectra is a long-standing question and an important research direction at the moment.

Bibliography

[1] V. Chorosajev, A. Gelzinis, L. Valkunas, D. Abramavicius, Dynamics of exciton-polaron transition in molecular assemblies: The variational approach, J. Chem. Phys. **140**, 244108 (2014).

[2] V. Chorosajev, O. Rancova, D. Abramavicius, Polaronic effects at finite temperatures in the B850 ring of the LH2 complex, Phys. Chem. Chem. Phys. **18**, 7966–7977 (2016).

[3] V. Chorosajev, A. Gelzinis, L. Valkunas, D. Abramavicius, Benchmarking the stochastic time-dependent variational approach for excitation dynamics in molecular aggregates, Chem. Phys. **481**, 108–116 (2016).

[4] J. Pan, A. Gelzinis, V. Chorosajev, M. Vengris, S. S. Senlik, J.-R. Shen, L. Valkunas, D. Abramavicius, J. P. Ogilvie, Ultrafast energy transfer within the photosystem ii core complex, Phys. Chem. Chem. Phys. **19**, 15356–15367 (2017).

[5] V. Chorosajev, T. Marciulionis, D. Abramavicius, Temporal dynamics of excitonic states with nonlinear electron-vibrational coupling, The Journal of Chemical Physics **147**(7), 074114 (2017).

[6] H. van Amerongen, L. Valkunas, R. van Grondelle, *Photosynthetic Excitons* (World Scientific, 2006).

[7] Y. Tanimura, R. Kubo, Time evolution of a quantum system in contact with a nearly Gaussian-markovian noise bath, J. Phys. Soc. Jpn. **58**, 101 (1989).

[8] D. E. Makarov, N. Makri, Path integrals for dissipative systems by tensor multiplication. condensed phase quantum dynamics for arbitrarily long time, Chem. Phys. Lett. **221**(5), 482–491 (1994).

[9] N. Makri, D. E. Makarov, Tensor propagator for iterative quantum time evolution of reduced density matrices. ii. numerical methodology, J. Chem. Phys. **102**(11), 4611–4618 (1995).

[10] J. Prior, A. W. Chin, S. F. Huelga, M. B. Plenio, Efficient simulation of strong system-environment interactions, Phys. Rev. Lett. **105**, 050404 (2010).

[11] L. Chen, R. Zheng, Q. Shi, Y. J. Yan, Optical line shapes of molecular aggregates: Hierarchical equations of motion method, J. Chem. Phys. **131**(9), 094502 (2009).

[12] A. Gelzinis, D. Abramavicius, L. Valkunas, Non-Markovian effects in time-resolved fluorescence spectrum of molecular aggregates: Tracing polaron formation, Phys. Rev. B **84**, 245430 (2011).

[13] Y. Tanimura, Reduced hierarchy equations of motion approach with drude plus brownian spectral distribution: Probing electron transfer processes by means of two-dimensional correlation spectroscopy, J. Chem. Phys. **137**(22), 22A550 (2012).

[14] A. G. Dijkstra, Y. Tanimura, Linear and third- and fifth-order nonlinear spectroscopies of a charge transfer system coupled to an underdamped vibration, J. Chem. Phys. **142**(21), 212423 (2015).

[15] A. Gelzinis, D. Abramavicius, L. Valkunas, Absorption lineshapes of molecular aggregates revisited, J. Chem. Phys. **142**(15), 154107 (2015).

[16] A. Ishizaki, G. R. Fleming, Theoretical examination of quantum coherence in a photosynthetic system at physiological temperature, Proc. Nat. Acad. Sci. USA **106**(41), 17255–17260 (2009).

[17] G. S. Schlau-Cohen, A. Ishizaki, T. R. Calhoun, N. S. Ginsberg, M. Ballottari, R. Bassi, G. R. Fleming, Elucidation of the timescales and origins of quantum electronic coherence in LHCii, Nat. Chem. **4**, 389–395 (2012).

[18] V. Balevičius Jr., A. Gelzinis, D. Abramavicius, L. Valkunas, Excitation Energy Transfer and Quenching in a Heterodimer: Applications to the Carotenoid–Phthalocyanine Dyads, J. Phys. Chem. B **117**(38), 11031–11041 (2013).

[19] F. D. Fuller, J. Pan, A. Gelzinis, V. Butkus, S. S. Senlik, D. E. Wilcox, C. F. Yocum, L. Valkunas, D. Abramavicius, J. P. Ogilvie, Vibronic coherence in oxygenic photosynthesis, Nat. Chem. **6**, 706–711 (2014).

[20] L. Chen, R. Zheng, Q. Shi, Y. Yan, Two-dimensional electronic spectra from the hierarchical equations of motion method: Application to model dimers, J. Chem. Phys **132**(2), 024505 (2010).

[21] C. Kreisbeck, T. Kramer, Long-lived electronic coherence in dissipative exciton dynamics of light-harvesting complexes, J. Phys. Chem. Lett. **3**(19), 2828–2833 (2012).

[22] H. Fehske, J. Loos, G. Wellein, Lattice polaron formation: Effects of nonscreened electron-phonon interaction, Phys. Rev. B **61**, 8016–8025.

[23] L.-C. Ku, S. A. Trugman, Quantum dynamics of polaron formation, Phys. Rev. B **75**, 014307 (2007).

[24] M. Hohenadler, H. G. Evertz, W. von der Linden, Quantum monte carlo approach to the holstein polaron problem, Phys. Status Solidi B **242**(7), 1406–1413 (2005).

[25] S. R. White, A. E. Feiguin, Real-time evolution using the density matrix renormalization group, Phys. Rev. Lett. **93**, 076401 (2004).

[26] V. May, O. Kühn, *Charge and Energy Transfer Dynamics in Molecular Systems* (Wiley-VCH Verlag GmbH & Co. KGaA, 2011).

[27] T. Holstein, Studies of polaron motion, Ann. Phys. **8**, 325–342 (1959).

[28] I. Frenkel, J. Frenkel, *Wave Mechanics: Elementary Theory* (Oxford University Press, 1936).

[29] M. J. Skrinjar, D. V. Kapor, S. D. Stojanovic, Classical and quantum approach to davydov's soliton theory, Phys. Rev. A **38**, 6402–6408 (1988).

[30] D. Walls, G. Milburn, *Quantum Optics* (Springer Berlin Heidelberg, 2008).

[31] A. Davydov, *A Theory of Molecular Excitons* (Mc.Graw-Hill, New York, 1962).

[32] A. S. Davydov, N. I. Kislucha, Solitary excitons in one-dimensional molecular chains, Phys. Status Solidi (b) **59**, 465 (1973).

[33] A. Scott, Davydov's soliton, Phys. Rep. **217**(1), 1–67 (1992).

[34] J. Sun, B. Luo, Y. Zhao, Dynamics of a one-dimensional Holstein polaron with the davydov ansatze, Phys. Rev. B **82**, 014305 (2010).

[35] J. Sun, L. Duan, Y. Zhao, Delocalized davydov d1 ansatz for the Holstein polaron, J. Chem. Phys. **138**(17), 174116 (2013).

[36] Q. Liu, Y. Zhao, W. Wang, T. Kato, Global-local ansatz and dynamical coherent potential approximation study of off-diagonal exciton-phonon coupling, Phys. Rev. B **79**, 165105 (2009).

[37] S. S. Mukamel, *Principles of nonlinear optical spectroscopy* (New York : Oxford University Press, 1995).

[38] V. Balevičius Jr., L. Valkunas, D. Abramavicius, Modeling of ultrafast time-resolved fluorescence applied to a weakly coupled chromophore pair, J. Chem. Phys **143**(2), 074101 (2015).

[39] T. Meier, Y. Zhao, V. Chernyak, S. Mukamel, Polarons, localization, and excitonic coherence in superradiance of biological antenna complexes, J. Chem. Phys **107**(10), 3876–3893 (1997).

[40] L. Valkunas, D. Abramavicius, T. Mančal, *Molecular Excitation Dynamics and Relaxation* (Wiley-VCH Verlag GmbH & Co. KGaA, 2013).

[41] E. Silinš, V. Čápek, *Organic molecular crystals: interaction, localization, and transport phenomena* (American Institute of Physics, 1994).

[42] P. M. Chaikin, A. F. Garito, A. J. Heeger, Excitonic polarons in molecular crystals, Phys. Rev. B **5**, 4966–4969 (1972).

[43] A. Song, R. Williams, *Self-trapped excitons*, Springer series in solid-state sciences (Springer, 1993).

[44] A. Matsui, Excitonic processes in aromatic molecular crystals of strong exciton-phonon coupling, Pure Appl. Chem. **67**, 429–436 (1995).

[45] F. C. Spano, The spectral signatures of frenkel polarons in h- and j-aggregates, Acc. Chem. Res. **43**, 429–439 (2010).

[46] A. Freiberg, M. Ratsep, K. Timpmann, G. Trinkunas, Excitonic polarons in quasi-one-dimensional LH1 and LH2 bacteriochlorophyll a antenna aggregates from photosynthetic bacteria: A wavelength-dependent selective spectroscopy study, Chem. Phys. **357**, 102–112 (2009).

[47] M. Pajusalu, M. Ratsep, G. Trinkunas, A. Freiberg, Davydov splitting of excitons in cyclic bacteriochlorophyll a nanoaggregates of bacterial light-harvesting complexes between 4.5 and 263 K, ChemPhysChem **12**(3), 634–644 (2011).

[48] M. K. Sener, S. Park, D. Lu, A. Damjanović, T. Ritz, P. Fromme, K. Schulten, Excitation migration in trimeric cyanobacterial photosystem i, J. Chem. Phys. **120**(23), 11183–11195 (2004).

[49] A. Freiberg, M. Ratsep, K. Timpmann, G. Trinkunas, N. W. Woodbury, Self-trapped excitons in LH2 antenna complexes between 5K and ambient temperature, J. Phys. Chem. B **107**, 11510–11519 (2003).

[50] A. H. Romero, D. W. Brown, K. Lindenberg, Converging toward a practical solution of the Holstein molecular crystal model, J. Chem. Phys. **109**(16), 6540–6549 (1998).

[51] A. H. Romero, D. W. Brown, K. Lindenberg, Polaron effective mass, band distortion, and self-trapping in the Holstein molecular-crystal model, Phys. Rev. B **59**(21), 13728–13740 (1999).

[52] B. Luo, J. Ye, Y. Zhao, Variational study of polaron dynamics with the davydov ansatze, Phys. Status Solidi (c) **8**(1), 70–73 (2011).

[53] Y. Zhao, D. W. Brown, K. Lindenberg, Variational energy band theory for polarons: Mapping polaron structure with the merrifield method, J. Chem. Phys. **106**(13), 5622–5630 (1997).

[54] Y.-C. Cheng, R. J. Silbey, A unified theory for charge-carrier transport in organic crystals, J. Chem. Phys. **128**(11), 114713 (2008).

[55] V. M. Kenkre, D. K. Campbell, Self-trapping on a dimer: Time-dependent solutions of a discrete nonlinear schrödinger equation, Phys. Rev. B **34**, 4959–4961 (1986).

[56] V. M. Kenkre, H.-L. Wu, Time evolution of the nonadiabatic nonlinear quantum dimer, Phys. Rev. B **39**, 6907–6913 (1989).

[57] V. Butkus, L. Valkunas, D. Abramavicius, Molecular vibrations-induced quantum beats in two-dimensional electronic spectroscopy, J. Chem. Phys. **137**, 044513 (2012).

[58] A. Gelzinis, L. Valkunas, F. D. Fuller, J. P. Ogilvie, S. Mukamel, D. Abramavicius, Tight-Binding Model of the Photosystem II Reaction Center: Application to Two-Dimensional Electronic Spectroscopy, New J. Phys. **15**(7), 075013 (2013).

[59] D. Abramavicius, B. Palmieri, D. V. Voronine, F. Šanda, S. Mukamel, Coherent multidimensional optical spectroscopy of excitons in molecular aggregates; quasiparticle versus supermolecule perspectives, Chem. Rev. **109**, 2350–2408 (2009).

[60] J. J. Ding, J. Xu, J. Hu, R. X. Xu, Y. Yan, Optimized hierarchical equations of motion theory for drude dissipation and efficient implementation to nonlinear spectroscopies, J. Chem. Phys. **135**(16), 164107 (2011).

[61] A. Ishizaki, T. R. Calhoun, G. S. Schlau-Cohen, G. R. Fleming, Quantum coherence and its interplay with protein environments in photosynthetic electronic energy transfer, Phys. Chem. Chem. Phys. **12**, 7319–7337 (2010).

[62] G. R. Fleming, M. Cho, Chromophore-solvent dynamics, Annu. Rev. Phys. Chem. **47**(1), 109–134 (1996).

[63] L. van Dijk, F. C. Spano, P. A. Bobbert, Theory of exciton dynamics in molecular aggregates in presence of polaronic effects, Chem. Phys. Lett **529**(0), 69–73 (2012).

[64] F. C. Spano, L. Silvestri, Multiple mode exciton-vibrational coupling in h-aggregates: Synergistic enhancement of the quantum yield, J. Chem. Phys **132**(9), 094704 (2010).

[65] A. G. Redfield, On the theory of relaxation processes, IBM J. Res. Develop. **1**(1), 19–31 (1957).

[66] A. Ishizaki, G. R. Fleming, On the adequacy of the Redfield equation and related approaches to the study of quantum dynamics in electronic energy transfer, J. Chem. Phys. **130**(23), 234110 (2009).

[67] T. Förster, Zwischenmolekulare energiewanderung und fluoreszenz, Ann. Phys. **437**(1-2), 55–75 (1948).

[68] M. Yang, G. R. Fleming, Influence of phonons on exciton transfer dynamics: comparison of the Redfield, förster, and modified Redfield equations, Chem. Phys. **275**(1-3), 355–372 (2002).

[69] M. Furukawa, K. Mizuno, A. Matsui, N. Tamai, I. Yamazaki, Branching of exciton relaxation to the free and self-trapped exciton states, Chem. Phys. **138**(23), 423–432 (1989).

[70] H. Fidder, J. Knoester, D. A. Wiersma, Optical properties of disordered molecular aggregates: A numerical study, J. Chem. Phys. **95**(11), 7880–7890 (1991).

[71] S. M. Vlaming, V. A. Malyshev, J. Knoester, Localization properties of one-dimensional frenkel excitons: Gaussian versus lorentzian diagonal disorder, Phys. Rev. B **79**, 205121 (2009).

[72] G. S. Schlau-Cohen, E. D. Re, R. J. Cogdell, G. R. Fleming, Determination of excited-state energies and dynamics in the b band of the bacterial reaction center with 2D electronic spectroscopy, J. Phys. Chem. Lett. **3**(17), 2487–2492 (2012).

[73] S. Prince, M. Papiz, A. Freer, G. McDermott, A. Hawthornthwaite-Lawless, R. Cogdell, N. Isaacs, Apoprotein structure in the LH2 complex from rhodopseudomonas acidophila strain 10050: modular assembly and protein pigment interactions, J. Mol. Biol. **268**, 412–423 (1997).

[74] U. Ermler, G. Fritzsch, S. K. Buchanan, H. Michel, Structure of the photosynthetic reaction centre from rhodobacter sphaeroides at 2.65a resolution: cofactors and protein-cofactor interactions, Structure **2**, 925–936 (1994).

[75] Y. Umena, K. Kawakami, J.-R. Shen, N. Kamiya, Crystal structure of oxygen-evolving photosystem ii at a resolution of 1.9, Nature **473**, 55–60 (2011).

[76] D. Hayes, G. B. Griffin, G. S. Engel, Engineering coherence among excited states in synthetic heterodimer systems, Science **340**(6139), 1431–1434 (2013).

[77] T. Renger, Theory of optical spectra involving charge transfer states: Dynamic localization predicts a temperature dependent optical band shift, Phys. Rev. Lett. **93**, 188101 (2004).

[78] T. Mančal, L. Valkunas, G. R. Fleming, Theory of exciton-charge transfer state coupled systems, Chem. Phys. Lett. **432**(1-3), 301–305 (2006).

[79] R. Jankowiak, M. Reppert, V. Zazubovich, J. Pieper, T. Reinot, Site selective and single complex laser-based spectroscopies: A window on excited state electronic structure, excitation energy transfer, and electron-phonon coupling of selected photosynthetic complexes, Chem. Rev. **111**(8), 4546–4598 (2011).

[80] S. Jang, Theory of multichromophoric coherent resonance energy transfer: A polaronic quantum master equation approach, J. Chem. Phys. **135**(3), 034105 (2011).

[81] V. Abramavicius, D. Abramavicius, Excitation transfer pathways in excitonic aggregates revealed by the stochastic schrodinger equation, J. Chem. Phys. **140**(6), 065103 (2014).

[82] Y.-H. Hwang-Fu, W. Chen, Y.-C. Cheng, A coherent modified Redfield theory for excitation energy transfer in molecular aggregates, Chem. Phys. **447**(0), 46–53 (2015).

[83] T. Mančal, F. Šanda, Quantum master equations for non-linear optical response of molecular systems, Chem. Phys. Lett. **530**, 140–144 (2012).

[84] J. Olšina, T. Mančal, Parametric projection operator technique for second order non-linear response, Chem. Phys. **404**, 103–115 (2012).

[85] B. Luo, J. Ye, C. Guan, Y. Zhao, Validity of time-dependent trial states for the Holstein polaron, Phys. Chem. Chem. Phys. **12**, 15073–15084 (2010).

[86] Y. Tanimura, Stochastic liouville, langevin, Fokker–Planck, and master equation approaches to quantum dissipative systems, J. Phys. Soc. Jpn. **75**(8), 082001 (2006).

[87] A. Ishizaki, G. R. Fleming, Unified treatment of quantum coherent and incoherent hopping dynamics in electronic energy transfer: Reduced hierarchy equation approach, J. Chem. Phys. **130**(1), 234111 (2009).

[88] S. S. Andrews, Using rotational averaging to calculate the bulk response of isotropic and anisotropic samples from molecular parameters, J. Chem. Educ. **81**(6), 877 (2004).

[89] M. F. Gelin, A. V. Pisliakov, W. Domcke, Time- and frequency-gated spontaneous emission as a tool for studying vibrational dynamics in the excited state, Phys. Rev. A **65**, 062507 (2002).

[90] S. Jang, R. Silbey, Theory of single molecule line shapes of multichromophoric macromolecules, J. Chem. Phys. **118**, 9312–9323 (2003).

[91] T.-C. Dinh, T. Renger, Towards an exact theory of linear absorbance and circular dichroism of pigment-protein complexes: Importance of non-secular contributions, J. Chem. Phys. **142**(3), 034104 (2015).

[92] T. D. Huynh, K.-W. Sun, M. Gelin, Y. Zhao, Polaron dynamics in two-dimensional photon-echo spectroscopy of molecular rings, J. Chem. Phys. **139**(10), 104103 (2013).

[93] K.-W. Sun, M. F. Gelin, V. Y. Chernyak, Y. Zhao, Davydov ansatz as an efficient tool for the simulation of nonlinear optical response of molecular aggregates, J. Chem. Phys. **142**(21), 212448 (2015).

[94] N. Zhou, L. Chen, Z. Huang, K. Sun, Y. Tanimura, Y. Zhao, Fast, accurate simulation of polaron dynamics and multidimensional spectroscopy by multiple davydov trial states, J. Phys. Chem. A **120**(9), 1562–1576 (2016).

[95] C. Olbrich, J. Strümpfer, K. Schulten, U. Kleinekathoefer, Theory and simulation of the environmental effects on FMo electronic transitions, J. Phys. Chem. Lett. **2**, 1771–1776 (2011).

[96] T. Renger, A. Klinger, F. Steinecker, M. S. am Busch, J. Numata, F. Müh, Normal mode analysis of the spectral density of the fenna-matthews-olson light-harvesting protein: How the protein dissipates the excess energy of excitons, J. Phys. Chem. B **116**(50), 14565–14580 (2012).

[97] R. Silbey, R. A. Harris, Variational calculation of the dynamics of a two level system interacting with a bath, J. Chem. Phys. **80**(6), 2615–2617 (1984).

[98] L. Wang, L. Chen, N. Zhou, Y. Zhao, Variational dynamics of the sub-ohmic spin-boson model on the basis of multiple davydov d1 states, J. Chem. Phys. **144**(2), 024101 (2016).

[99] R. Borrelli, M. F. Gelin, The generalized coherent state ansatz: Application to quantum electron-vibrational dynamics, Chemical Physics – (2016).

[100] R. J. Cogdell, A. Gall, J. Köhler, The architecture and function of the light-harvesting apparatus of purple bacteria: from single molecules to in vivo membranes, Q. Rev. Biophys. **39**, 227–324 (2006).

[101] X. Hu, T. Ritz, A. Damjanovic, F. Autenrieth, K. Schulten, Photosynthetic apparatus of purple bacteria, Q. Rev. Biophys. **35**(01), 1–62 (2002).

[102] G. McDermott, S. Prince, A. Freer, A. Hawthornthwaite-Lawless, M. Papiz, R. Cogdell, N. Isaacs, Crystal structure of an integral membrane light-harvesting complex from photosynthetic bacteria, Nature **374**, 517–521 (1995).

[103] J. Koepke, X. Hu, C. Muenke, K. Schulten, H. Michel, The crystal structure of the light-harvesting complex ii (b800–850) from rhodospirillum molischianum, Structure **4**, 581–597 (1996).

[104] M. Papiz, S. Prince, T. Howard, R. Cogdell, N. Isaacs, The structure and thermal motion of the b800-850 LH2 complex from rps.acidophila at 2.0A resolution and 100K: new structural features and functionally relevant motions, J. Mol. Biol. **326**, 1523–1538 (2003).

[105] J. F. Imhoff, Transfer of rhodopseudomonas acidophila to the new genus rhodoblastus as rhodoblastus acidophilus gen. nov., comb. nov., Int. J. Syst. Evol. Microbiol. **51**, 1863 (2001).

[106] T. Pullerits, M. Chachisvilis, V. Sundström, Exciton delocalization length in the b850 antenna of rhodobacter sphaeroides, J. Phys. Chem. **100**, 10787–10792 (1996).

[107] V. Sundström, T. Pullerits, R. van Grondelle, Photosynthetic light-harvesting: Reconciling dynamics and structure of purple bacterial LH2 reveals function of photosynthetic unit, J. Phys. Chem. B **103**, 2327–2346 (1999).

[108] G. D. Scholes, G. R. Fleming, On the mechanism of light harvesting in photosynthetic purple bacteria: B800 to b850 energy transfer, J. Phys. Chem. B **104**, 1854–1868 (2000).

[109] M. Ketelaars, A. M. van Oijen, M. Matsushita, J. Köhler, J. Schmidt, T. J. Aartsma, Spectroscopy on the b850 Band of individual light-harvesting 2 Complexes of rhodopseudomonas acidophila i. experiments and Monte Carlo simulations, Biophys. J. **80**, 1591–1603 (2001).

[110] Y. C. Cheng, R. J. Silbey, Coherence in the b800 ring of purple bacteria LH2, Phys. Rev. Lett. **96**, 028103 (2006).

[111] G. Trinkunas, O. Zerlauskiene, V. Urboniene, J. Chmeliov, A. Gall, B. Robert, L. Valkunas, Exciton band structure in bacterial peripheral light-harvesting complexes, J. Phys. Chem. B **116**, 5192–5198 (2012).

[112] R. J. Cogdell, J. Köhler, Use of single-molecule spectroscopy to tackle fundamental problems in biochemistry: using studies on purple bacterial antenna complexes as an example, Biochem. J. **422**, 193–205 (2009).

[113] O. Rancova, J. Sulskus, D. Abramavicius, Insight into the structure of photosynthetic LH2 Aggregate from 2 Spectroscopy simulations, J. Phys. Chem. B **116**, 7803–7814 (2012).

[114] A. F. Fidler, V. P. Singh, P. D. Long, P. D. Dahlberg, G. S. Engel, Probing energy transfer events in the light harvesting complex 2 (LH2) of rhodobacter sphaeroides with two-dimensional spectroscopy, J. Chem. Phys. **139**, 155101 (2013).

[115] A. F. Fidler, V. P. Singh, P. D. Long, P. D. Dahlberg, G. S. Engel, Time scales of coherent dynamics in the light-harvesting complex 2 (LH2) of rhodobacter sphaeroides, J. Phys. Chem. Lett. **4**(9), 1404–1409 (2013).

[116] A. F. Fidler, V. P. Singh, P. D. Long, P. D. Dahlberg, G. S. Engel, Dynamic localization of electronic excitation in photosynthetic complexes revealed with chiral two-dimensional spectroscopy, Nat. Commun. **5** (2014).

[117] O. Rancova, D. Abramavicius, Static and dynamic disorder in bacterial light-harvesting complex LH2: A 2Des simulation study, J. Phys. Chem. B **118**, 7533–7540 (2014).

[118] A. M. van Oijen, M. Ketelaars, J. Köhler, T. J. Aartsma, J. Schmidt, Unraveling the electronic structure of individual photosynthetic pigment-protein complexes, Science **285**, 400–402 (1999).

[119] K. Huang, A. Rhys, Theory of light absorption and non-radiative transitions in f-centres, Proc. R. Soc. A **204**(1078), 406–423 (1950).

[120] V. Novoderezhkin, M. Wendling, R. van Grondelle, Intra- and interband transfers in the b800-B850 Antenna of rhodospirillum molischianum: Redfield theory modeling of polarized pump-probe kinetics, J. Phys. Chem. B **107**, 11534–11548 (2003).

[121] J. Meldaikis, O. Zerlauskiene, D. Abramavicius, L. Valkunas, Manifestation of protein conformations in the b850 Absorption band of light-harvesting complex LH2, Chem. Phys. **423**, 9–14 (2013).

[122] O. Zerlauskiene, G. Trinkunas, A. Gall, B. Robert, V. Urboniene, L. Valkunas, Static and dynamic protein impact on electronic properties of light-harvesting complex LH2, J. Phys. Chem. B **112**(49), 15883–15892 (2008).

[123] T. Polívka, T. Pullerits, J. L. Herek, V. Sundström, Exciton relaxation and polaron formation in LH2 at low temperature, J. Phys. Chem. B **104**, 1088–1096 (2000).

[124] K. Timpmann, Z. Katiliene, N. W. Woodbury, A. Freiberg, Exciton self trapping in one-dimensional photosynthetic antennas, J. Phys. Chem. B **105**, 12223–12225 (2001).

[125] R. Kunz, K. Timpmann, J. Southall, R. J. Cogdell, A. Freiberg, J. Köhler, Exciton self trapping in photosynthetic pigment-protein complexes studied by single-molecule spectroscopy, J. Phys. Chem. B **116**, 11017–11023 (2012).

[126] W. H. Zurek, Pointer basis of quantum apparatus: Into what mixture does the wave packet collapse?, Phys. Rev. D **24**, 1516–1525 (1981).

[127] E. Joos, H. D. Zeh, The emergence of classical properties through interaction with the environment, Z. Phys. B **59**(2), 223–243 (1985).

[128] O. Rancova, R. Jankowiak, D. Abramavicius, Probing environment fluctuations by two-dimensional electronic spectroscopy of molecular systems at temperatures below 5 K, J. Chem. Phys. **142**, 212428 (2015).

[129] D. Abramavicius, L. Valkunas, Role of coherent vibrations in energy transfer and conversion in photosynthetic pigment-protein complexes, Photosynth. Res. 1–15 (2015).

[130] S. Georgakopoulou, R. N. Frese, E. Johnson, C. Koolhaas, R. J. Cogdell, R. van Grondelle, G. van der Zwan, Absorption and CD spectroscopy and modeling of various LH2 Complexes from purple bacteria, Biophys. J. **82**, 2184 (2002).

[131] J. Ye, K. Sun, Y. Zhao, Y. Yu, C. K. Lee, J. Cao, Excitonic energy transfer in light-harvesting complexes in purple bacteria, J. Chem. Phys. **136**, 245104 (2012).

[132] K. Sun, J. Ye, Y. Zhao, Path induced coherent energy transfer in light-harvesting complexes in purple bacteria, J. Chem. Phys. **141**, 124103 (2014).

[133] M. H. C. Koolhaas, R. N. Frese, G. J. S. Fowler, T. S. Bibby, S. Georgakopoulou, G. van der Zwan, C. N. Hunter, R. van Grondelle, Identification of the upper exciton component of the b850 Bacteriochlorophylls of the LH2 Antenna complex, using a b800-Free mutant of rhodobacter sphaeroides, Biochemistry (Mosc.) **37**, 4693 (1998).

[134] R. van Grondelle, V. Novoderezhkin, Dynamics of excitation energy transfer in the lh1 and LH2 light-harvesting complexes of photosynthetic bacteria, Biochemistry (Mosc.) **40**, 15057–15068 (2001).

[135] M. Dahlbom, T. Pullerits, S. Mukamel, V. Sundström, Exciton delocalization in the b850 light-harvesting complex: Comparison of different measures, J. Phys. Chem. B **105**, 5515–5524 (2001).

[136] H.-M. Wu, M. Ratsep, R. Jankowiak, R. J. Cogdell, G. J. Small, Comparison of the LH2 Antenna complexes of rhodopseudomonas acidophila (strain 10050) and rhodobacter sphaeroides by high-pressure absorption, high-pressure hole burning, and temperature-dependent absorption spectroscopies, J. Phys. Chem. B **101**, 7641–7653 (1997).

[137] D. Hsu, J. L. Skinner, On the thermal broadening of zero-phonon impurity lines in absorption and fluorescence spectra, J. Chem. Phys. **81**, 1604 (1984).

[138] J. L. Skinner, D. Hsu, Pure dephasing of a two-level system, J. Phys. Chem. **90**, 4931–4938 (1986).

[139] A. Anda, L. De Vico, T. Hansen, D. Abramavicius, Absorption and fluorescence lineshape theory for polynomial potentials, J. Chem. Theory Comput. **12**(12), 5979–5989 (2016).

[140] M. Vojta, N.-H. Tong, R. Bulla, Quantum phase transitions in the sub-ohmic spin-boson model: Failure of the quantum-classical mapping, Phys. Rev. Lett. **94**, 070604 (2005).

[141] M. Schröder, U. Kleinekathöfer, M. Schreiber, Calculation of absorption spectra for light-harvesting systems using non-Markovian approaches as well as modified Redfield theory, J. Chem. Phys. **124**, 084903 (2006).

[142] V. Balevičius Jr, A. Gelzinis, D. Abramavicius, L. Valkunas, Excitation energy transfer and quenching in a heterodimer: Applications to the carotenoid-phthalocyanine dyads, J. Phys. Chem. B (0) (2013).

[143] F. Sanda, V. Perlík, C. N. Lincoln, J. Hauer, Center line slope analysis in two-dimensional electronic spectroscopy, J. Phys. Chem. A **119**(44), 10893–10909 (2015).

Acknowledgments

I would like express my gratitude to all the people who were with me during the years of my PhD studies. This thesis would have certainly been impossible without you.

First of all, I would like to thank my supervisor, prof. Darius Abramavičius for guidance in my research, giving me a broader context on every result, and for his great patience. Second, I would like to thank prof. Leonas Valkūnas for highly valuable discussions and for sharing his experience. My gratitude also goes to dr. Maxim Gelin for inviting me for a visit to Munchen and to prof. dr. Reinhard F. Werner for steering me away from experiments and towards mathematics a long time ago.

My thanks and best wishes go to all my colleagues in the Department of Theoretical Physics: V. Abramavičius, A. Gelžinis, V. Balevičius Jr., J. Chmeliov, V. Butkus, O. Rancova, M. Jakučionis, T. Marčiulionis, S. Toliautas, V. Dūdėnas, J. Meldaikis. It was a great pleasure working with you!

I would also like to personally thank all of my friends (in no particular order) for making sure I have a life outside of academia: Vytautas, Konstantin T., Konstantin K., Elena, Eduard, Julija, Donatas, Aleksandr, Jan, Izabelė, Saulius, Gytis, Mindaugas, Tatjana, Anna.

Next, I would like to thank my family for supporting me in every way.

And lastly, I would like to express my special thanks to Ieva.